Fall 2013

Bio-inspired design, fabrication and testing of bipolar plates for PEM fuel cells

Nannan Guo

Department: Mechanical and Aerospace Engineering

BIO-INSPIRED DESIGN, FABRICATION AND TESTING OF BIPOLAR PLATES FOR PEM FUEL CELLS

by

NANNAN GUO

A DISSERTATION

Presented to the Faculty of the Graduate School of the

MISSOURI UNIVERSITY OF SCIENCE AND TECHNOLOGY

In Partial Fulfillment of the Requirements for the Degree

DOCTOR OF PHILOSOPHY

in

MECHANICAL ENGINEERING

2013

Approved by

Ming C. Leu, Advisor
Umit O. Koylu
Frank Liou
K. Chandrashekhara
Joseph W. Newkirk

PUBLICATION DISSERTATION OPTION

This dissertation has been prepared in the form of five papers for publication. Pages 7-38 have been published in International Journal of Hydrogen Energy. Pages 39-75 have been published in International Journal of Hydrogen Energy. Pages 76-102 have been submitted to Journal of Fuel Cell Science and Technology. Pages 103-136 have been submitted to Journal of Power Sources. Pages 137-168 have been submitted to International Journal of Hydrogen Energy. All of them have been prepared in the format for publication in the corresponding journals. The balance of this dissertation follows the standard dissertation format.

ABSTRACT

The flow field of a bipolar plate distributes reactants for polymer electrolyte membrane (PEM) fuel cells and removes the produced water from the fuel cells. It greatly influences the performance of fuel cells, especially the concentration losses. Two approaches were developed to improve flow field designs in this dissertation. One is inspired by the biological circulatory structures and called bio-inspired designs, which have great potential to transport reactant efficiently and hence improve fuel cell performance. Another way is using a network-based optimization model to optimize the conventional flow field configurations, i.e., pin-type, parallel and serpentine designs, to improve flow distributions within the channels. A three-dimensional, two-phase numerical model was developed to investigate the mass, velocity and pressure distributions within the different flow fields and also the final fuel cell performance. Selective Laser Sintering, which provides a cost- and time-efficient way to build parts with complicated geometries, was used to fabricate graphite composite bipolar plates with these developed designs. Different graphite materials, including natural graphite, synthetic graphite, carbon black, and carbon fiber, were investigated in order to achieve higher electrical conductivity and flexural strength of the fabricated bipolar plates. Experimental testing of the PEM fuel cells with these fabricated bipolar plates was carried out to verify the numerical model and compare the performance for different flow field designs. Both the numerical and experimental results demonstrated that the bio-inspired designs and the optimized designs could substantially improve the fuel cell performance compared to the traditional designs.

ACKNOWLEDGMENTS

I would like to express my sincere gratitude to my advisor, Dr. Ming C. Leu, for providing guidance and constant encouragement during my graduate study at Missouri University of Science and Technology. He provided an excellent working atmosphere and supported me in every aspect. It has been a privilege and a pleasure to have worked with him.

I would like to thank Dr. Umit O. Koylu for his valuable advices and help in my research work. I would like to extend my appreciation to Dr. Frank Liou, Dr. K. Chandrashekhara, and Dr. Joseph W. Newkirk, for serving as my committee members and for their examination of the dissertation.

The dissertation was supported by the National Science Foundation grant #CMMI-1131659 and the Air Force Research Laboratory contract #FA8650-04-C-5704, which are gratefully acknowledged. I would like to thank the Department of Mechanical and Aerospace Engineering at Missouri University of Science and Technology for assisting my graduate study and research.

Finally, I wish to thank my wife, Jie Li, my son, Ryan, my parents and parents in law, for their love, understanding and support.

TABLE OF CONTENTS

LIST OF ILLUSTRATIONS

Page

PAPER II

PAPER III

LIST OF TABLES

Page

1. INTRODUCTION

1.1. PEM FUEL CELLS

A fuel cell is an electrochemical cell which converts chemical energy from a fuel and an oxidant into electrical energy. Different from conventional electrochemical batteries, fuel cells can produce electricity continuously as long as the necessary fuel is supplied, and do not need to be recharged by an external source. In this way, a fuel cell works like a combustion engine, but it is more efficient than a combustion engine in terms of energy conversion. For example, a typical fossil fuel power plant operates at about 35% efficiency, while a fuel cell can operate at 40-60% efficiency. There are several types of fuel cells including polymer electrolyte membrane (PEM) fuel cell, solid oxide fuel cell (SOFC), molten carbonate fuel cell (MCFC), direct methanol fuel cell, and so on. Compared to other types of fuel cells, the PEM fuel cell has great advantages such as low-temperature operation, high-power density, fast start-up, system robustness, and low emissions. This dissertation focuses on PEM fuel cells. The research has a high potential to generate enormous economic impact because of the promising future market of fuel cell vehicles. Several automotive industry leaders have speculated that fuel cell vehicles could account for 20-25% of about 60 million new cars sold worldwide annually in the next 20 to 25 years, and the total revenue of fuel cells is estimated between 4.5 and 45 billion dollars [1,2].

In a PEM fuel cell unit (see Figure 1.1), hydrogen molecules are split into electrons and hydrogen protons on the catalyst layer. The hydrogen protons pass across the polymeric membrane and combines with oxygen (usually from air) to form water at the cathode, while the electrons go around an external circuit to produce electricity. The theoretical optimum voltage of a single PEM fuel cell unit is around 1.2 V, but in reality the voltage of a fuel cell drops off due to three kinds of losses (see Figure 1.2): activation losses related to the energy barrier that must be overcome to initiate chemical reaction between the reactants; ohmic losses related to voltage lost in order to overcome the resistance of electrolyte, electrodes and other connections; and mass transport losses which occur when the electrochemical reactions are hindered by the effect of mass

transport which inhibits further electrochemical reaction [3]. Therefore, when a fuel cell operates at a high current density, mass transport of reactants is critical.

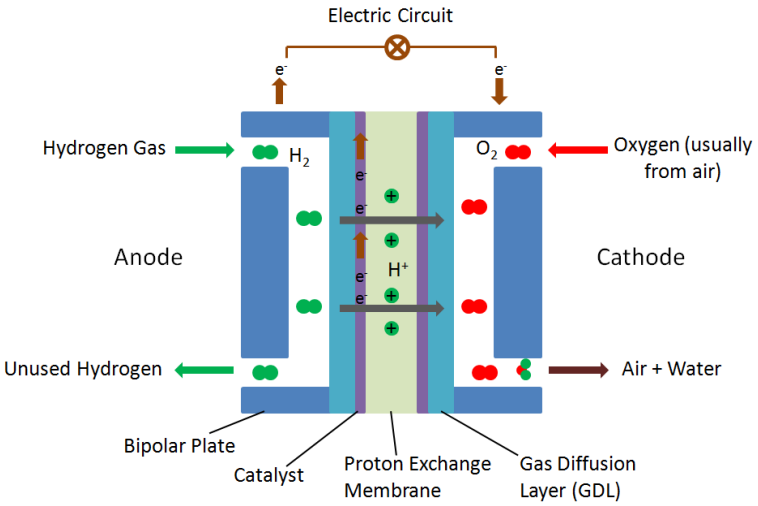

Figure 1.1. PEM fuel cell unit

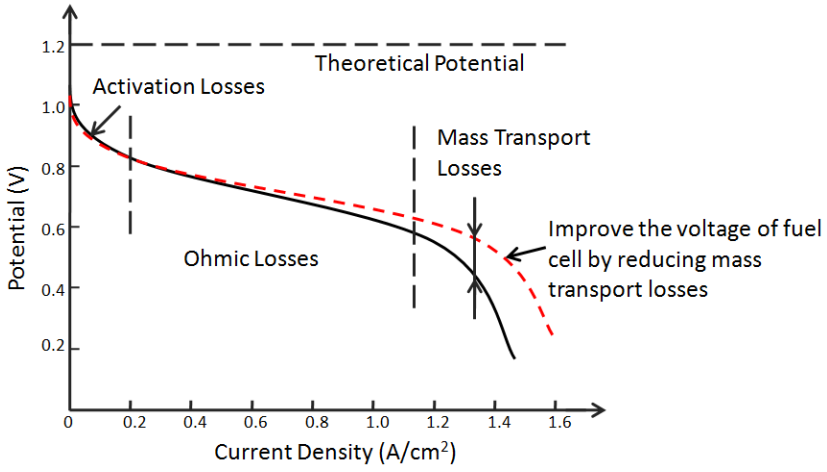

Figure 1.2. Typical PEM fuel cell polarization curve and the proposed improvement by reducing mass transport losses (dashed, red curve)

1.2. BIPOLAR PLATES

A bipolar plate is a vital component in a PEM fuel cell. It supplies fuel and oxygen to reaction sites, removes reaction products (i.e., liquid water) out of the fuel cell, collects the generated current, and provides mechanical support for the fuel cell. Bipolar plates are critical because they constitute more than 60% of the weight and 30% of the total cost in a fuel cell stack [4]. By using bio-inspired flow field designs for bipolar plates, the proposed research has great potential to increase the performance of PEM fuel cells by 30-50% in power density. In this way, the cost of a fuel cell stack can be lowered greatly because less fuel cell units will be needed for the required power output of the stack.

Bipolar plates are usually made of graphite, metal, or graphite composite. Graphite has good electrical conductivity and chemical resistance, but it is very difficult to machine graphite due to its brittleness. Metal has high electrical conductivity, but its poor chemical resistance does not allow it to work for a long time within the chemical environment of PEM fuel cell. With the advantages of easy manufacture and excellent chemical resistance, graphite composites are becoming more and more promising for producing bipolar plates.

The performance of a PEM fuel cell stack depends highly on the bipolar plate. In a PEM fuel cell unit, the flow field on the bipolar plate transports reactants. The flow field design has a significant effect on the transport efficiency for reactants. Previous studies [5, 6] have shown that the power density of a fuel cell can be increased significantly with a proper flow field design for the bipolar plate alone. This dissertation is aimed at enhancing the efficiency of transport of reactants and reducing the mass transport losses, thereby leading to significant increase of output voltage at high current densities (see the dashed, red curve in Figure 1.2) and generation of more power.

Water removal is also an important aspect of reducing mass transport losses. Since the PEM fuel cell works at ~80℃, which is below the boiling point of water, the produced liquid water at the cathode tends to accumulate at the small pores of the gas diffusion layer and the flow channels, blocking the pathway of reactant gases. Consequently, the fuel cell may stop working due to lack of reactant supply. This problem, called water flooding, becomes a much more serious problem when a fuel cell is

operating at a high current density. Past studies [7, 8] have shown that appropriate design of flow channels is the best strategy for solving the water flooding problem, which will be addressed along other critical issues in this thesis.

1.3. DESIGN OF FLOW FIELDS INSPIRED BY NATURE

Many efficient natural networks such as veins of plant leaves and blood vessels of animal lungs (see Figure 1.3) supply materials from a central source to a distributed sink/target. Consider the tree leave, which contains a large number of channels feeding progressively to the cells containing chlorophyll where photosynthesis takes place. During the photosynthesis process water is taken through the root of the plant and distributed to the leaf surface by veins, and spread to the cells that contain chlorophyll. At the same time, the produced carbohydrates are collected and transported by veins to the other places of the plant.

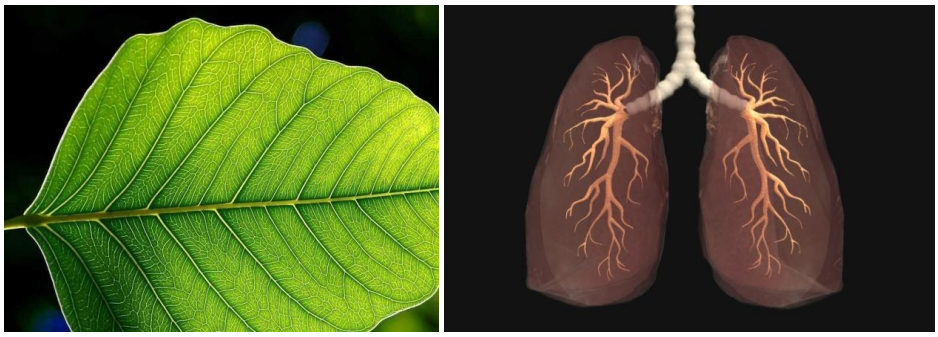

Figure 1.3. Leaf vein system [9] and human lung blood vessel system [10], both of which have structures to supply nutrient from one source to the entire leaf surface or lung in an efficient way

The flow field of bipolar plates transports fuel and oxidant to the reaction area where hydrogen molecules are broken into protons and electrons. Therefore, one approach to design the flow fields of bipolar plates is to use mass transport networks having similar structures as the veins of tree leaves and the blood vessels of animal lungs.

Figure 1.4 shows a mapping from natural structures to the flow fields of bipolar plates in terms of functions, structures, transported matters, and deriving forces. All these aspects can be mapped from natural biological systems to bipolar plates, thus it is reasonable to assume that these natural structures can be applied to the flow field design for bipolar plates.

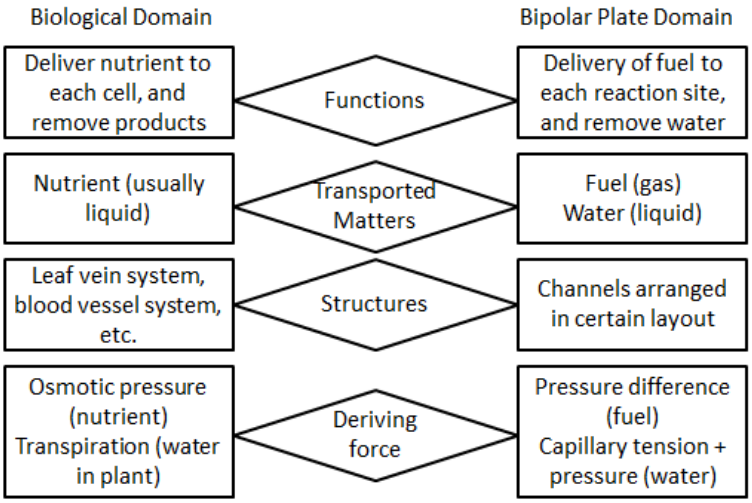

Figure 1.4. Mapping from nature's structures of mass transportation to the flow fields of bipolar plates.

1.4. FABRICATION OF BIPOLAR PLATES

Recently much attention has been paid on graphite/polymer composite bipolar plates [11-18], which have excellent chemical resistance. Two promising fabrication methods for mass production of these bipolar plates are injection molding (IM) [11] and compression molding (CM) [12]. Although these methods are suitable for mass production, they are not time-efficient or cost-effective for studying the bipolar-plate flow field design, which includes numerous channel cross-section shapes and dimensions and layouts. For the IM and CM processes, the mold corresponding to each different design will have to be fabricated, which is very expensive ($5,000-$25,000) and time-consuming (4-6 weeks). In contrast, the cost is much lower (<$50) and the time is shorter

(2-4 days) if the bipolar plates are fabricated using the Selective Laser Sintering (SLS) process.

Selective Laser Sintering has been used to fabricate graphite composite bipolar plates for PEM fuel cells [19-22]. In the SLS process, a mixture of graphite materials and binder is scanned by laser and the molten binder bonds graphite particles together to form 3D parts layer by layer. After a green part is built, it undergoes post-processing, carbonization and infiltration to increase the bipolar plate's electrical conductivity and mechanical strength, as well as its gas impermeablility. In this dissertation study, the SLS process was used to fabricate graphite composite bipolar plates with various bio-inspired designs of flow fields and the fabricated bipolar plates were used in conjunction with finite element simulation to verify the validity of the mathematical models used for the bio-inspired design and the superiority of the created flow fields compared with the those from conventional designs.

1.5. SUMMARY OF THE WORK

This dissertation comprises of five journal papers which have been or will be published. Each of the papers focuses on one topic, including SLS fabrication process of graphite composite bipolar plates, experimental study of the SLS fabricated bipolar plates, optimization model of flow fields, optimization of conventional flow field designs, and bio-inspired flow field designs. Two methods, optimization of conventional designs and utilization of bio-inspired designs, were developed to improve the current flow field designs for PEM fuel cells. Both numerical simulations and experimental studies were carried out to investigate the performance of the developed flow field designs. The mass, velocity and pressure distributions were also investigated using the numerical simulation. A Selective Laser Sintering based process was developed to fabricate graphite composite bipolar plates with these developed flow field designs. Different graphite materials were investigated to improve the electrical conductivity and flexural strength of the fabricated bipolar plates.

PAPER

I. Effect of Different Graphite Materials on the Electrical Conductivity and Flexural Strength of Bipolar Plates Fabricated using Selective Laser Sintering

Nannan Guo and Ming C. Leu

Department of Mechanical and Aerospace Engineering

Missouri University of Science and Technology, Rolla, MO 65409, USA

Corresponding author: Nannan Guo

Email: ngzn6@mail.mst.edu

Abstract

Selective Laser Sintering provides a way to fabricate graphite composite bipolar plates for use in fuel cells. This significantly reduces time and cost at the research and development stage of bipolar plates, as compared with the conventional fabrication methods such as compression molding and injection molding. Different graphite materials, including natural graphite, synthetic graphite, carbon black, and carbon fiber, were investigated using the selective laser sintering process to fabricate bipolar plates. The effect of each material on the electrical conductivity and flexural strength of the bipolar plates was studied experimentally. With a proper combination of these materials, bipolar plates with electrical conductivity ranging from 120-380 S/cm and flexural strength ranging from 30-50 MPa have been obtained, which satisfy the requirements set by the Department of Energy and also are comparable with those developed by compression molding and injection molding. A modified percolation model was proposed

to predict the electrical conductivity of the fabricated bipolar plates with different compositions. The analytical results calculated from the proposed model agree well with the experimental results. Finally, a single PEM (Proton Exchange Membrane) fuel cell unit was assembled using the fabricated bipolar plates, and its in-situ performance was studied.

Keywords: Graphite composite; Bipolar plates; Electrical conductivity; Selective Laser sintering; Percolation model.

1. Introduction

The bipolar plate, which accounts for 40-50% of the cost and 60-80% of the weight of a fuel cell stack [1, 2], is an important part of a Proton Exchange Membrane (PEM) fuel cell. The bipolar plate's main functions include carrying current away from each fuel cell, distributing gas fuels within the cell and providing support for the Membrane Electrode Assembly (MEA). The Department of Energy proposed a technical target of bipolar plates for the year 2010 [3], in which the main requirements are electrical conductivity >100 S/cm and flexural strength >25 MPa.

Compared with metals, graphite is an excellent material for bipolar plates due to its excellent chemical resistance and low density. However, its brittle nature makes it difficult to manufacture. Recently, more and more researchers have been focusing on graphite/polymer composite bipolar plates [4-10], which are easier to fabricate and have better mechanical properties. Two conventional fabrication methods for graphite

composite bipolar plates are injection molding (IM) [7] and compression molding (CM) [8], which are very suitable for mass production but less efficient for the research and development stage because of their significantly high cost and long mold preparation time. Because bipolar plates are design intensive and include numerous options of flow channel patterns and channel dimensions [11], thousands of designs must be investigated at the R&D stage. During the IM or CM process, a corresponding mold must be fabricated for each different design, which is very costly and time consuming [12] (see Table 1).

Selective Laser Sintering (SLS), an Additive Manufacturing technique, has been studied to fabricate graphite composite bipolar plates for PEM fuel cells [13-15]. Figure 1 shows the schematic of the selective laser sintering process. In the SLS process, the mixture of graphite and binder particles is scanned by a laser, and the molten binder bonds graphite particles together to form three-dimensional parts layer by layer. The major advantages of the SLS process are its ability to build complex flow channels and the limited time and cost resources consumed in making bipolar plates from each design (Table 1). Therefore, the SLS process can reduce the lead time and the cost for the R&D stage of bipolar plates, compared with IM and CM processes.

One issue that arises when fabricating bipolar plates using the SLS process is the relatively low electrical conductivity [14]. Several methods of increasing electrical conductivity have been studied, such as infiltration with conducting epoxy resin [14, 15], liquid phenolic infiltration/re-curing [14, 15] and increasing the carbonization temperature [16, 17]. Additionally, researchers recently have investigated the effect of

various graphite materials on the properties of bipolar plates fabricated by CM and IM [18, 19]. However, no previous study has been conducted to investigate the effect of graphite materials on the bipolar plates made by the SLS process. SLS is much different from CM and IM, so graphite materials could have different influences on the properties of bipolar plates fabricated using the former method versus the latter methods.

In this paper, different graphite materials, including Natural Graphite (NG), Synthetic Graphite (SG), Carbon Fiber (CF) and Carbon Black (CB), were studied in order to increase electrical conductivity and mechanical strength for the purpose of fulfilling the Department of Energy's requirements. The effect of each material on the properties of bipolar plates was studied, and the bipolar plates fabricated using SLS were compared with those fabricated using CM and IM [7, 18-21]. Furthermore, a modified percolation model was proposed to predict the electrical conductivity and to explain the conduction mechanism of the fabricated graphite composite bipolar plates. Finally, the in-situ performance of a single PEM fuel cell unit with the fabricated bipolar plates was studied.

2. Materials and Processes

2.1 Materials

Natural graphite (3610), synthetic graphite (4437), carbon black (5303) and carbon fiber (AGM99) were obtained from Asbury Graphite Mills, Inc. (New Jersey, USA). The properties of these materials are provided in Table 2. Natural graphite has high intrinsic

electrical conductivity because of its highly crystalline structure. Synthetic graphite is a product made by high-temperature treatment of amorphous carbon materials, usually calcined petroleum coke and coal tar pitch. It has a more uniform size and an almost spherical shape. Carbon black, manufactured by the combustion or thermal decomposition of hydrocarbon fuel under a reducing condition, has the finest primary particle size of all the common industrial carbons. Because the particles of carbon black are very small, the specific surface area is very large. Carbon fiber was used as the reinforcing phase to enhance the mechanical strength of bipolar plates. Phenolic powder (GP-5546, Georgia Pacific) with an average size of 15 μm was used as a binder. After carbonization, porous brown parts were infiltrated with liquid epoxy resin (EPON^{TM} Resin 828), as a matrix. The density of the liquid epoxy resin was 1.16g/cm^3. EPIKURE^{TM} 3230 was used as a curing agent to promote the curing reaction of epoxy resin.

2.2 Fabrication Process

The fabrication process is shown in Fig. 2. Graphite powder and phenolic binder were ball milled together for 12 hours to achieve a uniform mixture. A SLS machine (Sinterstation 2000) was used to build green parts from the uniform mixture. The CAD model of a bipolar plate is first converted into slices. A laser beam scans the powder bed according to the cross-section of each slice (see Fig. 1). The binder, which has a low melting point, is melted by laser and bonds the graphite particles. After one layer is scanned, the powder bed is lowered by one layer thickness and a new layer of the powder

material is fed on the top. The process is repeated until the bipolar plate fabrication is completed. The parameters used in the SLS process were: fill laser power (12 W), outline laser power (4 W), laser scan speed (1524 mm/s), layer thickness (0.1016 mm), and laser scan spacing (0.0762 mm). The temperatures of the part bed and feed bins were maintained at 60 ^{o}C and 40 ^{o}C, respectively. For carbonization, green parts were heated to 1000 ^{o}C in a furnace filled with Argon gas to dissociate the binder and convert it to carbon residue to get brown parts. The heating schedule was from room temperature to 200 ^{o}C with a heating ramp rate of 60 ^{o}C/h, followed by a slower rate of 30 ^{o}C/h to 600 ^{o}C, and then a 50 ^{o}C/h ramp rate to 1000 ^{o}C, holding for 1 h. Brown parts, which are porous and weak, must be infiltrated with a liquid resin to become gas impermeable and to increase mechanical strength. For infiltration, porous brown parts were immersed into the mixture of a liquid epoxy resin and a curing agent, taken out after 20 min for their surfaces to be cleaned, and then placed in an oven at 80 ^{o}C for 30 min to cure the infiltrated resin.

2.3 Experiments

Synthetic graphite, carbon black and carbon fiber were mixed with natural graphite in different volume ratios and then mixed with 35vol% binder (which is kept constant in all experiments), forming SG/NG/binder, CB/NG/binder, and CF/NG/binder mixtures. The binder content was determined experimentally to ensure that the green parts had enough mechanical strength to go through post processing without substantially lowering electrical conductivity. These mixtures of graphite materials and binder were used to

fabricate test samples and bipolar plates using the SLS process, and the fabricated parts were infiltrated with liquid epoxy resin. The properties of the final infiltrated parts were measured.

2.4 Characterization

Electrical conductivity was measured using the four-point probe technique, following the ASTM C611 specifications and using the Keithley 2400 SourceMeter. The average of the data obtained from five 20×3×3 mm^3 specimens was calculated, and the standard deviation calculated was less than 12%. Flexural strength was measured with the three-point bending method, using the Instron Model 4468. Five samples with the dimensions of 3×10×60 mm^3 were tested. The data was averaged, and the standard deviation was calculated. The microstructure of the samples was obtained using the Hitachi S-4700 FE-SEM.

3. Results and Discussion

3.1 Microstructures

During the fabrication process, the bipolar plate's microstructure changed as it went from the green part to the brown part and then to the infiltrated part (final part), as shown in Fig. 3. Fig. 3(a) shows the microstructure of a green part, in which the binder bonded the graphite particles (SG and NG) together. After carbonization, the phenolic binder

dissociated, and the ligaments converted to porous amorphous graphite [22]. Many pores were left in the brown part (Fig. 3(b)). Finally, these pores were filled with resin through infiltration, leaving only a few minute voids inside the part (Fig. 3(c)).

3.2 Effect of the Infiltration Process

The aim of resin infiltration is to increase the part's mechanical strength and make the bipolar plate gas impermeable. The experimental results show that the bipolar plate's flexural strength increased from 2.03 MPa to 33.4 MPa after resin infiltration (see Table 3). One concern of the infiltration process is that the insulating resin might reduce the electrical conductivity of the brown part. However, the experimental data show no distinct difference between the electrical conductivity before and after infiltration, as shown in Table 3. The material used here was 25vol% SG, 40vol% NG and 35vol% binder. Apparently, good contact between graphite particles has been established in both the green parts and the brown parts (Fig. 3(a), (b)), and the good contact is not broken by resin infiltration. Therefore, it appears feasible to increase mechanical strength and make bipolar plates gas impermeable without experiencing a significantly negative effect on the electrical conductivity.

3.3 Effect of Synthetic Graphite

Figure 4 shows the microstructure of a brown part made from the mixture of SG and NG, in which the larger, flaky particles are NG and the smaller, spherical ones are SG. Electrical conductivity and flexural strength of bipolar plates with different volume

fractions of SG is shown in Fig. 5. When only NG (65vol%) and binder (35vol%) were used, electrical conductivity was 380 S/cm. As the percentage of SG increased, the part's conductivity decreased because the conductivity of SG particles is lower than that of NG particles. When SG particles were introduced into NG powder, these particles hindered the conduction of current among NG particles. The data show that in order to achieve the target conductivity value of DOE (100 S/cm), the SG content should not be more than 15vol%.

As shown in Fig. 5, SG has a slightly negative effect on the flexural strength, which decreased from about 37 MPa to 33 MPa when SG increased from 5vol% to 65vol%. This effect was seen because adding smaller SG particles filled up the big pores among larger NG flakes (as shown in Fig. 4). This reduced the porosity; consequently, a smaller amount of resin was absorbed after infiltration. The strength decreased because the strength of the bipolar plates relies primarily on the cured resin. Despite the reduced strength, all the strength data were still higher than the target value of strength set by DOE (25 MPa).

3.4 Effect of Carbon Fiber

Carbon fiber is used widely in composite materials as a reinforcing agent to enhance the mechanical properties of the composite. Figure 6 shows the microstructure of a brown part made from the mixture of CF and NG, in which long and thin CF was mixed uniformly with NG particles.

Electrical conductivity and flexural strength with different volume fractions of CF is shown in Fig. 7. Electrical conductivity decreased as CF increased. The carbon fibers orient randomly after the fabrication of bipolar plates, as shown in Fig. 6. The conductivity values of individual carbon fibers are highly anisotropic. The fibers oriented perpendicularly to the electric current offer higher resistance to the transport of electrons than those with parallel orientations [18, 23]. The carbon fibers with orientations perpendicular to the current transport break the contacts of NG particles and consequently increase the electrical resistance. Flexural strength increased substantially (from 35 MPa to 40 MPa) after introducing CF, as expected, and kept increasing with increases in the CF fraction, as shown in Fig. 7. When the CF content was 25vol%, the flexural strength was almost 50 MPa, which was 1.5 times of the measured flexural strength without CF.

3.5 Effect of Carbon Black

It was reported that nano-sized CB could be dispersed among NG particles to increase the electrical conductivity of graphite composite bipolar plates fabricated using compression molding [18, 19]. Chen, et al. [14, 15] also used an epoxy resin containing CB powder to infiltrate bipolar plates fabricated using the SLS process with the intent to improve electrical conductivity. In our present study, CB powder was mixed with NG powder to fabricate bipolar plates using the SLS process. Figure 8 shows the microstructure of a brown part made from 16vol% CB, 49vol% NG and 35vol% binder. As shown in Fig. 8(b), the surface of the NG particle was covered by the nano-sized CB particles.

The variation of electrical conductivity and flexural strength with different volume fractions of CB is shown in Fig. 9. As the content of CB increased, conductivity gradually decreased. After the fraction of CB reached 5vol%, electrical conductivity fell below 100 S/cm. This is because CB has lower intrinsic conductivity than NG. In the ball-milling process, three powders, CB, NG and binder, were mixed together. Nano CB particles with large surface areas tended to agglomerate on and cover the whole surface of NG particles (see Fig. 8), which hindered the contacts between NG particles. This CB effect is different from that seen in compression molding [18], where improved electrical conductivity was reported when CB powder was added at less than 4vol%. The reason for the difference is that, in compression molding, NG and CB are mixed in liquid resin first, where CB can disperse well and fill the small voids between the NG particles rather than agglomerating and covering the surface of the NG particles; thus, the electric current travels through those conductive CB particles instead of the insulating resin, thereby reducing resistance. In terms of flexural strength of the CB/NG/binder (Fig. 9), a similar result with the SG/NG/binder was obtained when adding CB to NG. Flexural strength decreased slightly when the CB content increased, possibly because the coverage of CB on the surface of NG makes it difficult for liquid resin (matrix) to fully wet the surface of NG particles (main filler); therefore, after the resin cures, the interface between the filler and matrix weakens, and flexural strength declines.

3.6 Percolation Model for Electrical Conductivity

From the electrical conductivity measurement results, NG powder gives the highest electrical conductivity compared with other graphite materials due to its high intrinsic conductivity. The conductivity decreased when SG, CF or CB was added to the NG/binder composite. Moreover, electrical conductivity decreased rapidly when other graphite powders were introduced to the NG/binder. After that, the conductivity decreased slightly as the amount of other graphite materials increased, and it eventually maintained consistency. This phenomenon is similar to the phenomenon observed in the case of mixing a conductor (metallic powder) and an insulator (polymer powder), which is explained by the percolation theory [23-25]. The composite behaves as an insulator when the volume fraction of the conductive filler is below a specific value known as the percolation threshold. Above this critical content, an infinite conductive cluster is formed, and the composite becomes conductive. A sharp conductivity change occurs within a very narrow concentration range.

Take the SG/NG/binder as an example. This composite can be seen as a binary composite (instead of three phases) by adding various volume fractions of the SG/binder mixture into the NG/binder mixture because the volume fraction of binder content is the same, 35vol%, in the SG/NG/binder, SG/binder, and NG/binder. In other words, the SG/NG/binder composite is formed by adding one conductive composite with lower conductivity (SG/binder) into another, higher-conductivity composite (NG/binder). In this way, it can be explained similarly using the conduction mechanism of adding conductive filler into the insulating matrix in the percolation theory. The SG/NG/binder composite maintains its initially high conductivity before the volume fraction of the

introduced SG falls below a specific value (the percolation threshold). Above this threshold, the conductivity decreases sharply within a small volume fraction range; after that, the composite maintains a low conductivity and remains almost unchanged.

We propose a modified power-law equation based on the percolation model [25] to predict the conductivity of the SG/NG/binder composite as follows:

$$\sigma = \begin{cases} \sigma_H, & p < p_c \\ \sigma_H - \sigma_0 (p - p_c)^c, & p \geq p_c \end{cases}$$

$$\sigma = \begin{cases} \sigma_H, & p < p_c \\ \sigma_H - \sigma_0 (p - p_c)^c, & p \geq p_c \end{cases} \quad (1)$$

where σ is the electrical conductivity of the final composite, and p is the volume fraction of the SG/binder in the mixture of the SG/binder and the NG/binder. p can be calculated from the volume fraction of SG (V_{SG}) in the SG/NG/binder mixture (note that the binder fraction is 35vol%) as

$$p = \frac{V_{SG}}{65} \quad (2)$$

p_c is the percolation threshold, which is the volume fraction at which the conductivity starts to decrease, c is the critical exponent, and σ_0 is the constant of proportionality and can be related to the conductivity of the two mixed composites, σ_H and σ_L, by

$$\sigma_H - \sigma_L = \sigma_0 (1 - p_c)^c \quad (3)$$

Substitute Equation (3) into (1),

$$\sigma = \begin{cases} \sigma_H, & p < p_c \\ \sigma_H - (\sigma_H - \sigma_L)\left(\frac{p - p_c}{1 - p_c}\right)^c, & p \geq p_c \end{cases} \quad (4)$$

From Equation (4), the conductivity of the SG/NG/binder with a given volume fraction of SG can be calculated once the percolation threshold p_c and the critical exponent c have been determined. Because the percolation threshold is the critical content of the SG/binder after which the conductivity begins to decrease sharply, this threshold can be determined from the experimental results. Here, for the SG/NG/binder, $p_c = 4.6\%$ corresponds to $V_{SG} = 3\ vol\%$. The critical exponent, $c = 0.14$, is determined using Equation (4) with the experimental data in Fig. 5 and the least squares method to minimize errors. Here, $\sigma_H = 388\ S/cm$ is the conductivity of the NG/binder composite, and $\sigma_L = 25\ S/cm$ is the conductivity of the SG/binder composite. Figure 10(a) shows the comparison of the analytical results using the percolation model and the experimental results for the SG/NG/binder composite.

Following the same procedure, the parameters in Equation (4) determined for the CF/NG/binder composite from the experimental results (Fig. 7) are $\sigma_H = 388\ S/cm$, $\sigma_L = 60\ S/cm$, $p_c = 3\%$ ($V_{CF} = 2\ vol\%$), and $c = 0.07$. Also, the parameters for the CB/NG/binder composite are $\sigma_H = 388\ S/cm$, $\sigma_L = 50\ S/cm$, $p_c = 1.2\%$ ($V_{CB} = 0.8\ vol\%$), and $c = 0.08$. The comparisons of the analytical results and the experimental results for the CF/NG/binder and the CB/NG/binder are shown in Fig. 10(b) and (c), respectively. Figure 10 shows that the results calculated from Equation (4) agree very well with the experimental results, indicating that the proposed equation based on the percolation model is able to predict the electrical conductivity of the mixture with two different conductive composites.

3.7 Comparison with Compression Molding and Injection Molding

The properties of bipolar plates obtained using the SLS process are compared with those obtained using the CM and IM processes, as shown in Table 4. The density of SLS-fabricated bipolar plates is lower than those by CM and IM. This is because the porous brown parts from SLS green parts are not completely infiltrated by resin, and only the surface is fully filled during the infiltration process, leaving the part inside porous. The electrical conductivities of commercially available products provided by SGL [7], Schunk [20] and BMCI [21] are slightly higher than 100 S/cm. The electrical conductivity of the bipolar plates developed in the National Physical Laboratory (NPL), India [18], ranges from 143 to 500 S/cm when different graphite materials are used in compression molding. For the SLS process, the electrical conductivity values we obtained range from 120 S/cm to 380 S/cm, which is comparable to those achieved using the CM and IM processes. In terms of flexural strength, the values of bipolar plates fabricated using SLS are also comparable to those fabricated using CM and IM, even without using pressure in the SLS process. This is because the bipolar plates get their strength primarily from cured resin, so whether or not pressure is involved has little effect.

4. Fabricated Bipolar Plate and PEM Fuel Cell In-situ Test

Several bipolar plates with the serpentine flow field design were fabricated using the SLS process, as shown in Fig. 11. The material composition in this fabrication was 45vol%

NG, 10vol% CF, 10vol% SG and 35vol% binder. The electrical conductivity measured was around 120 S/cm, and the flexural strength was 40 MPa. The feature dimensions were: active area - 50×50 mm^2, thickness - 4 mm, channel width - 1.5 mm and depth - 1.5 mm.

A single fuel cell unit was assembled using two fabricated bipolar plates (Fig. 11), two metal end plates, and one commercial membrane electrode assembly (MEA). The MEA comprises a loading of 0.5 mg/cm^2 Pt as the catalyst on both the anode and cathode sides, Nafion® 115 as the membrane, and a carbon cloth as the gas diffusion layer (GDL). The performance was measured using a fuel cell test station (Greenlight Innovation, G40) under the operation condition given in Table 5. Current density was varied, and the corresponding voltage was recorded after the steady state was reached. The polarization curve and the curve of power density versus current density are shown in Fig. 12. The performance of the fuel cell shows a typical polarization curve, indicating that the graphite composite bipolar plates fabricated with the SLS process satisfy the application requirements of PEM fuel cells. The power density continually increases as the current density increases, and it reaches the maximum of around 0.38 W/cm^2 when the current density is around 1.0 A/cm^2. The performance of the fuel cell with these bipolar plates is compared to that with bipolar plates made by the CM process reported by NPL [8] in Fig. 12, showing a very close performance achieved for bipolar plates made by the SLS process.

5. Conclusions

Different graphite materials, including natural graphite, synthetic graphite, carbon black, and carbon fiber, were investigated using the selective laser sintering process to fabricate graphite composite bipolar plates, and their effects on electrical conductivity and mechanical strength were studied. Natural graphite is good for electrical conductivity, and carbon fiber significantly increases flexural strength. Nano-sized carbon black, which covers the surface of natural graphite particles, negatively effects both electrical conductivity and flexural strength. Synthetic graphite decreases electrical conductivity and has a slight negative effect on flexural strength. The electrical and mechanical properties of graphite composite bipolar plates fabricated using the selective laser sintering were comparable to those obtained using injection molding and compression molding. A power-law equation based on the percolation theory was proposed to predict the electrical conductivity of the graphite composite with two conductive fillers. The analytical results agree well with the experimental results. Finally, bipolar plates were fabricated using the selective laser sintering process with the material composition of 45vol% natural graphite, 10vol% carbon fiber, 10vol% synthetic graphite and 35vol% binder, and their performance in a single PEM fuel cell unit was shown comparable to bipolar plates made by the compression molding.

Acknowledgements

This project is funded by the Air Force Research Laboratory contract #FA8650-04-C-5704 and by the National Science Foundation grant #CMMI-1131659.

References

[1] Tsuchiya H, Kobayashi O. Mass production cost of PEM fuel cell by learning curve. Int J Hydrogen Energy 2004;29:985-90.

[2] Hermann A, Chaudhuri T, Spagnol P. Bipolar plates for PEM fuel cells: A review. Int J Hydrogen Energy 2005;30:1297-302.

[3] Department of Energy. Technical Plan – Fuel cells. http://www1.eere.energy.gov/hydrogenandfuelcells/mypp/pdfs/fuel_cells.pdf, last accessed in September 2011.

[4] Mehta V, Cooper JS. Review and analysis of PEM fuel cell design and manufacturing. J Power Sources 2003;114:32-53.

[5] Du L, Jana SC. Highly conductivity epoxy/graphite composites for bipolar plates in proton exchange membrane fuel cells. J Power Sources 2007;172:734-41.

[6] Kakati BK, Sathiyamoorthy D, Verma A. Electrochemical and mechanical behavior of carbon composite bipolar plate for fuel cell. Int J Hydrogen Energy 2010;35:4185-94.

[7] Muller A, Kauranen P, Ganski AV, Hell B. Injection moulding of graphite composite bipolar plates. J Power Sources 2006;154:467-71.

[8] Dhakate SR, Mathur RB, Kakati BK, Dhami TL. Properties of graphite-composite bipolar plate prepared by compression molding technique for PEM fuel cell. Int J Hydrogen Energy 2007;32:4537-43.

[9] Wolf H, Willert-Porada M. Electrically conductive LCP-carbon composite with low carbon content for bipolar plate application in polymer electrolyte membrane fuel cell. J Power Sources 2006;153:41-6.

[10] Blunk R, Elhamid MHA, Lisi D, Mikhail Y. Polymeric composite bipolar plates for vehicle application. J Power Sources 2006;156:151-7.

[11] Li X, Sabir I. Review of bipolar plates in PEM fuel cells: Flow-field designs. Int J Hydrogen Energy 2005;30:359-71.

[12] Carlson EJ, Kopf P, Sinha J, Sriramulu S, Yang Y. Cost analysis of PEM fuel cell system for transportation. Subcontract Report, National Renewable Energy Laboratory, Cambridge, Massachusetts, September 30, 2005.

[13] Chen S, Bourell DL, Wood KL. Fabrication of PEM fuel cell bipolar plates by indirect SLS. In: Proceedings of the International SFF Symposium 2004, p244-56.

[14] Chen S, Murphy J, Herlehy J, Bourell DL, Wood KL. Development of SLS fuel cell current collectors. Rapid Prototyping Journal 2006;12(5):275-82.

[15] Chen S, Bourell DL, Wood KL. Improvement of electrical conductivity of SLS PEM fuel cell bipolar plates. In: Proceedings of the International SFF Symposium 2005, p458-67.

[16] Alayavalli K, Bourell DL. Fabrication of Electrically Conductive, Fluid Impermeable Direct Methanol Fuel Cell (DMFC) Graphite Bipolar Plates by Indirect Selective Laser Sintering (SLS). In: Proceedings of the International SFF Symposium 2008, p186-93.

[17] Alayavalli K, Bourell DL. Fabrication of modified graphite bipolar plates by indirect selective laser sintering (SLS) for direct methanol fuel cells. Rapid Prototyping Journal 2010;16(4):268-74.

[18] Mathur RB, Dhakate SR, Gupta DK, Dhami TL, Aggarwal RK. Effect of different carbon fillers on the properties of graphite composite bipolar plate. J Mater Process Technol 2008;203:184-92.

[19] Lee JH, Jang YK, Hong CE, Kim NH, Li P, Lee HK. Effect of carbon fillers on properties of polymer composite bipolar plates of fuel cells. J Power Sources 2009;193:523-9.

[20] Schunk Kohlenstofftechnik GmbH. Schunk-Molded Bipolar Plates for Fuel Cells. 2008.

[21] Bulk Molding Compounds, Inc. BMC 940 Data Sheet. 2009.

[22] Bourell DL, Leu MC, Chakravarthy K, Guo N, Alayavalli K. Graphite-based indirect laser sintered fuel cell bipolar plates containing carbon fiber additions. CIRP Annals – Manufacturing Technology 2011;60: 275-8.

[23] Antunes RA, de Oliveira MCL, Ett G, Ett V. Carbon materials in composite bipolar plates for polymer electrolyte membrane fuel cells: A review of the main challenges to improve electrical performance. J Power Sources 2011;196:2945-61.

[24] Sun Y, Bao HD, Guo ZX, Yu J. Modeling of the electrical percolation of mixed carbon fillers in polymer-based composites. Macromolecules 2009;42:459-63.

[25] Zelinka SL, Glass SV, Stone DS. A percolation model for electrical conduction in wood with implications for wood – water relations. Wood and Fiber Science 2008;40(4):544-52.

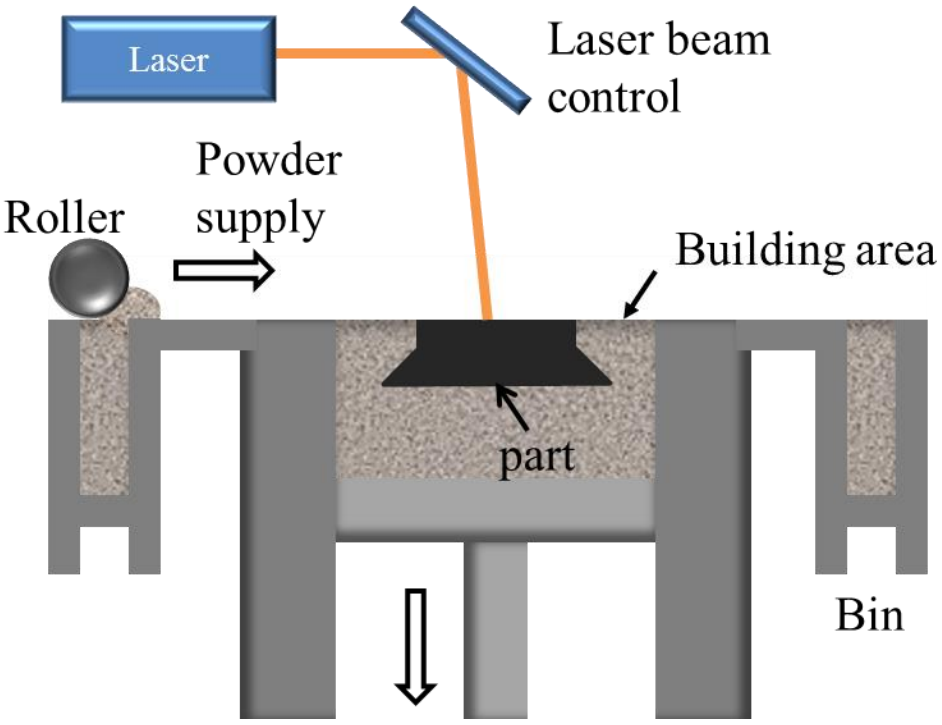

Fig. 1 Schematic of the selective laser sintering process.

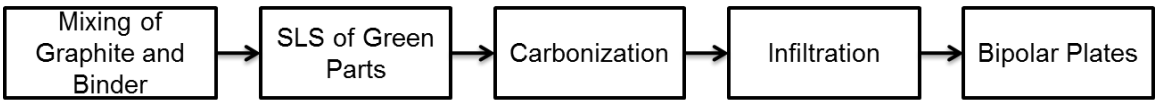

Fig. 2 SLS fabrication process of bipolar plates.

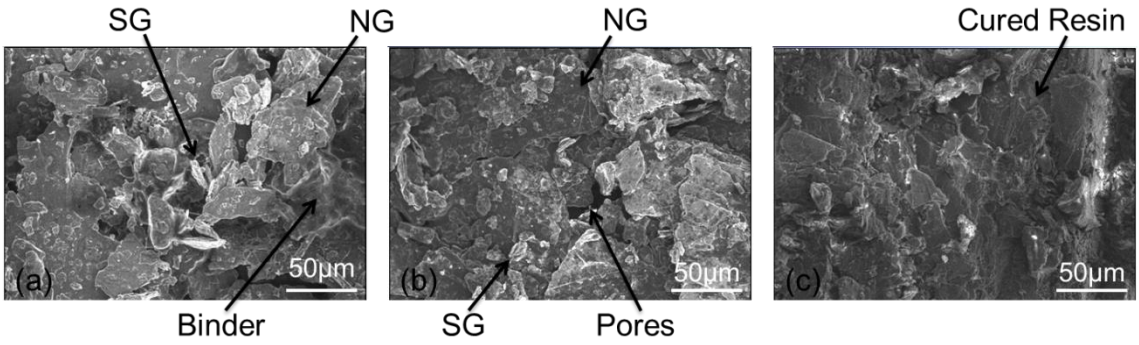

Fig. 3 Change of microstructures during the fabrication process: (a) green part; (b) brown part; (c) infiltrated part. The material composition is 15vol% SG, 50vol% NG and 35vol% binder.

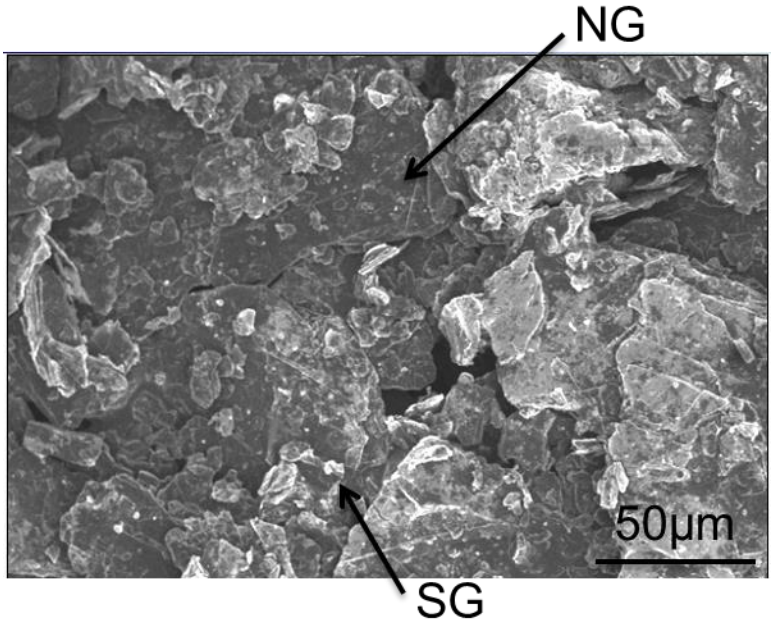

Fig. 4 Microstructure of a brown part made from 15vol% SG, 50vol% NG and 35vol% binder.

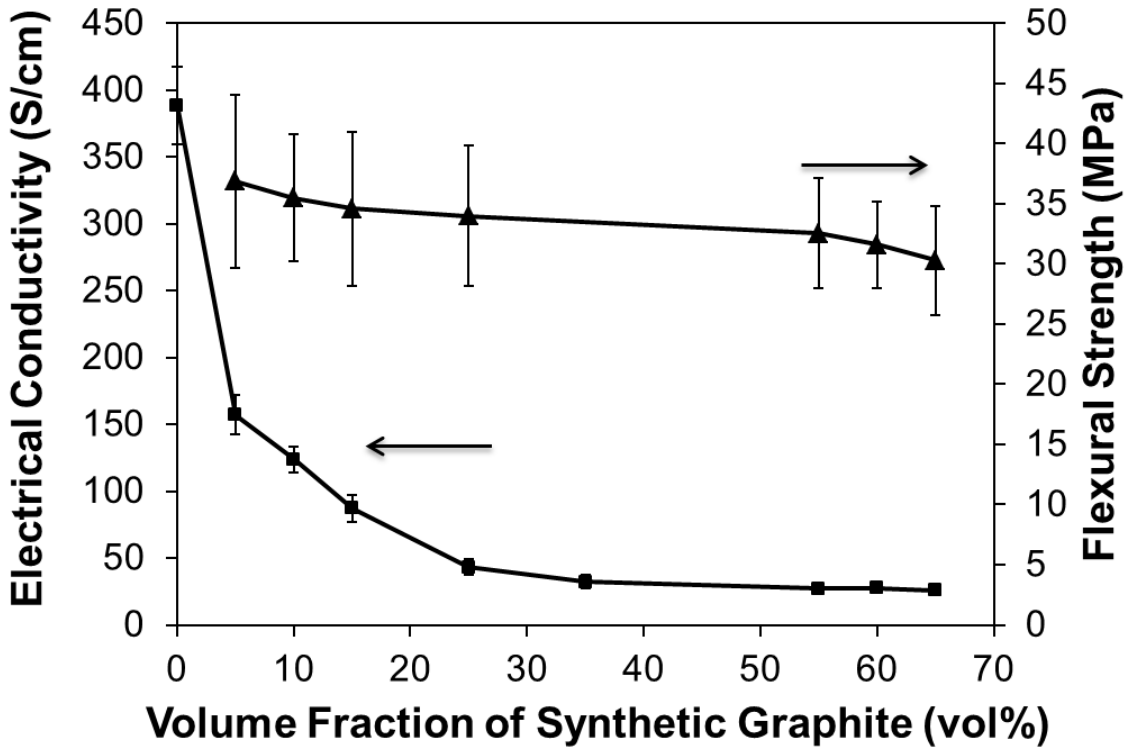

Fig. 5 Electrical conductivity and flexural strength of SG/NG/binder varies with different SG fractions (keeping binder at 35vol%, with the rest being NG).

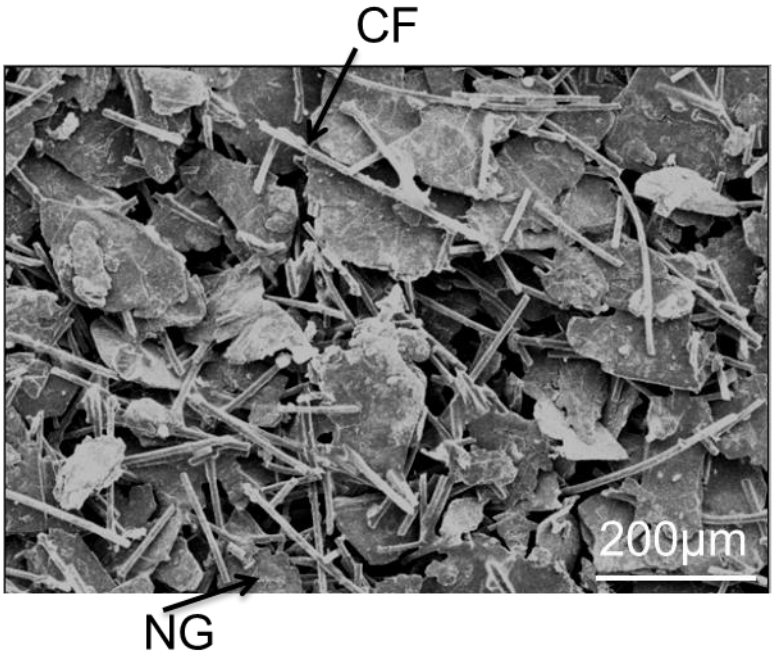

Fig. 6 Microstructure of a brown part made from 25vol% CF, 40vol% NG and 35vol% binder.

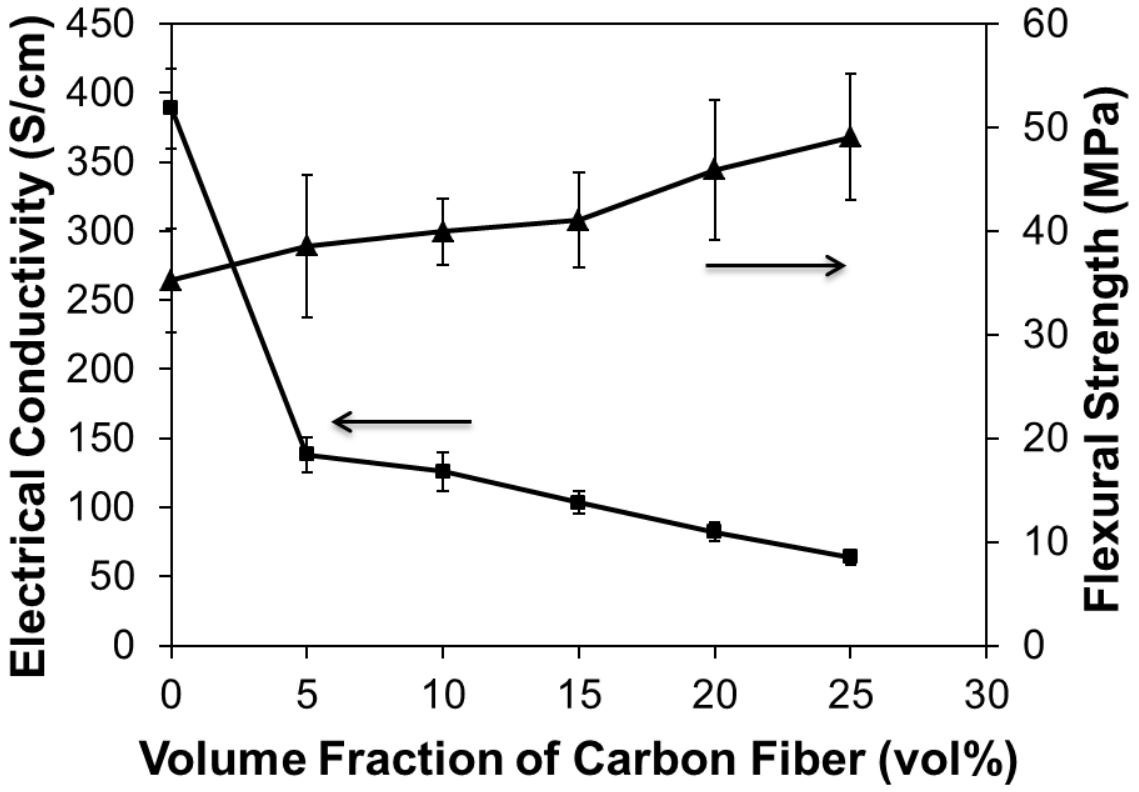

Fig. 7 Electrical conductivity and flexural strength of CF/NG/binder varies with different carbon fiber fractions.

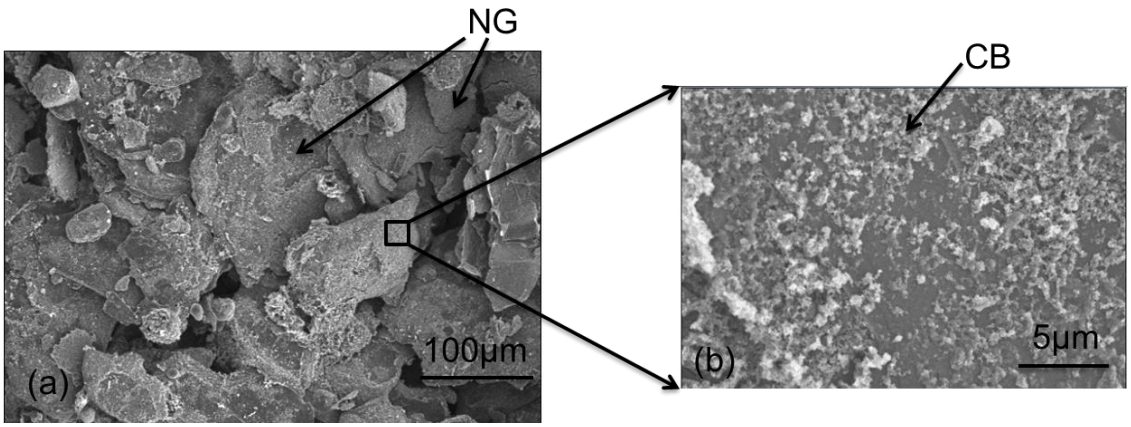

Fig. 8 (a) Microstructure of a brown part made from the mixture of NG and CB; (b) detailed view of the surface of an NG particle (16vol% CB, 49vol% NG and 35vol% binder).

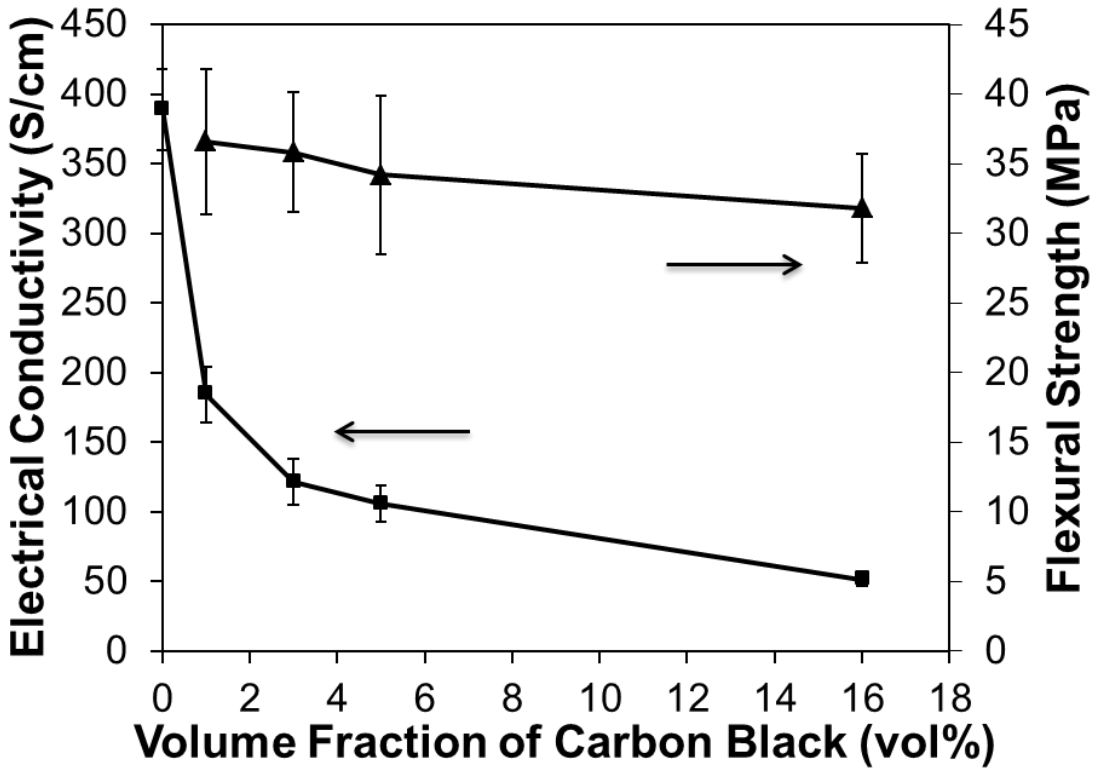

Fig. 9 Electrical conductivity and flexural strength of CB/NG/binder varies with different CB fractions.

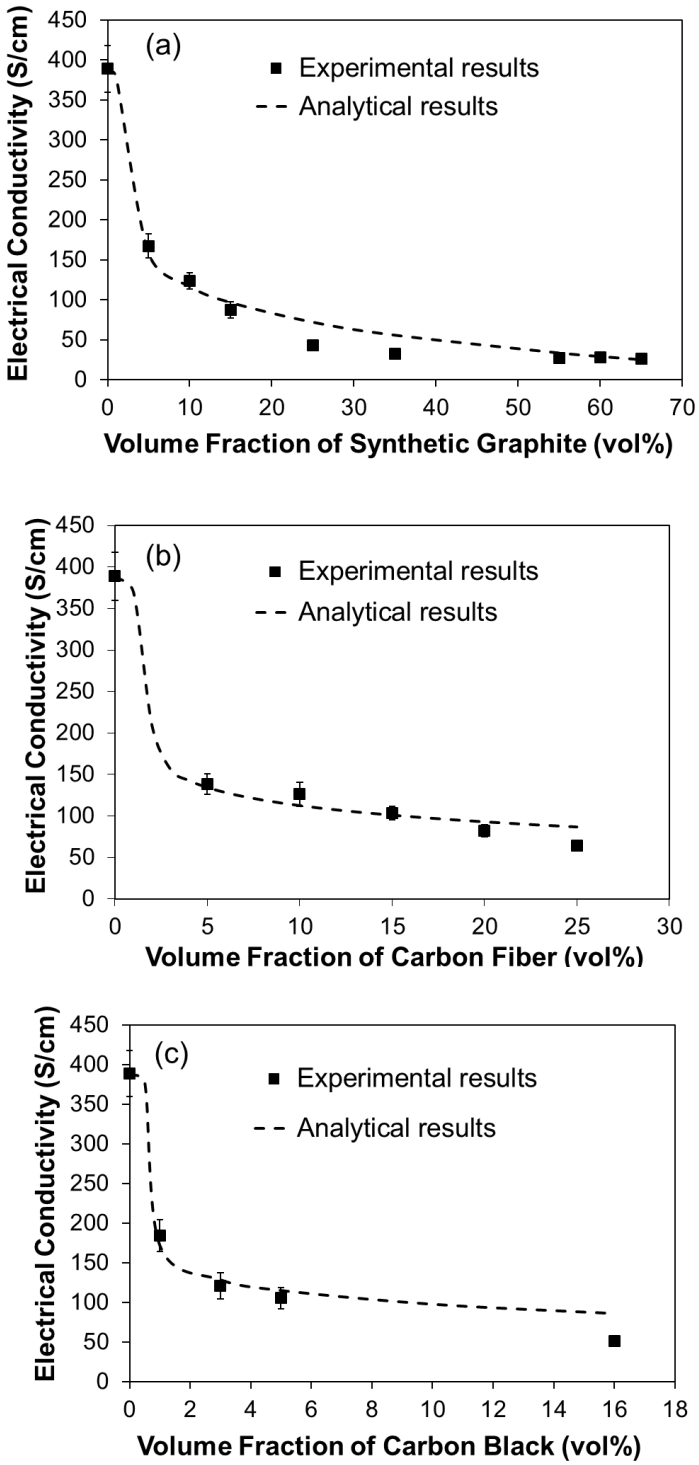

Fig. 10 The comparison of analytical results and experimental results for (a) SG/NG/binder, (b) CF/NG/binder, (c) CB/NG/binder.

Fig. 11 Bipolar plate with a serpentine flow field (active area: 50×50 mm^2, thickness: 4 mm, channel width: 1.5 mm and depth: 1.5 mm).

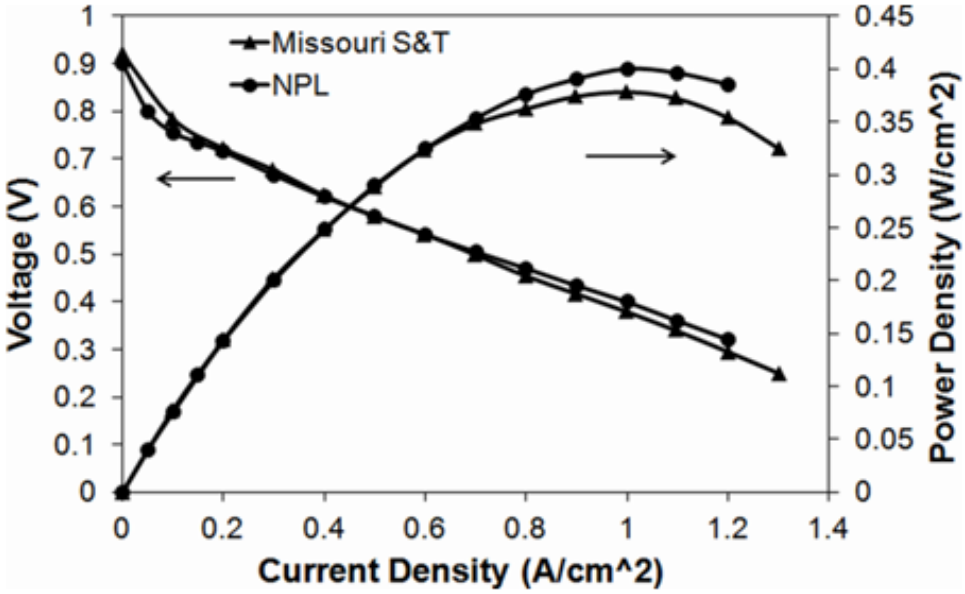

Fig. 12 The polarization curve and power density curve obtained from the in-situ test of the single fuel cell unit and the comparison of fuel cell performance between SLS and CM built bipolar plates.

Table 1 Comparison of time and cost consumed for SLS and conventional processes at the R&D stage.

	CM & IM [12]	SLS
Cost for one design	$5,000-$25,000	<$100
Lead time	4-6 weeks	4-7 days

Table 2 Properties of the graphite materials* used in the study.

Properties	Natural Graphite (3610)	Synthetic Graphite (4437)	Carbon Black (5303)	Carbon Fiber (AGM99)
Size (μm)	75-150	10-45	<0.03	Diameter 7.4 Length 150
Theoretical Density (g/cm^3)	2.26	2.26	1.8	1.75
Surface Area (m^2/g)	1.27	11.46	254	1.87
Typical Conductivity** (S/cm)	27.78	17.24	2.93	-

* The properties are provided by Asbury Graphite Mills, Inc., NJ, USA.

** The listed conductivity is the conductivity of the powder, not the intrinsic conductivity of the material.

Table 3 Properties of bipolar plates before and after infiltration.

	Flexural strength (MPa)	Electrical conductivity (S/cm)
Before infiltration	2.03±0.96	46.5
After infiltration	33.4±4.5	43.2

*The material used was 25vol% SG, 40vol% NG and 35vol% binder.

Table 4 Comparison of the properties of graphite composite bipolar plates fabricated using different methods.

Properties	Supplier					
	Missouri S&T[b]	SGL PPG86[a] [7]	SGL BBP4[a] [7]	Schunk FU4369[a] [20]	BMCI 940-8649[a] [21]	NPL[b] [18]
Process	SLS	IM	IM	CM	CM	CM
Density (g/cm^3)	1.25~1.58	1.85	1.98	1.90	1.82	>1.85
Electrical conductivity (S/cm)	120-380	55.6	125	111	100	143-500
Flexural strength (MPa)	~40	40	50	40	40	45

a: Commercial product; b: Research stage.

Table 5 Operation condition for the in-situ test of the single fuel cell unit.

Temperature	Back pressure	H_2 flow rate	Air flow rate	Humidity
75 ℃	2.0 atm	9.92×10^{-7} kg/s	2.6×10^{-5} kg/s	100%

PAPER

II. Network Based Optimization Model for Pin-Type Flow Field of Polymer Electrolyte Membrane Fuel Cell

Nannan Guo, Ming C. Leu, and Umit O. Koylu

Department of Mechanical and Aerospace Engineering

Missouri University of Science and Technology, Rolla, MO 65409, USA

Corresponding author: Nannan Guo

Email: ngzn6@mail.mst.edu

Abstract

The flow field of a bipolar plate distributes reactants for polymer electrolyte membrane (PEM) fuel cells and removes the produced water from the fuel cells. It greatly influences the performance of fuel cells, especially the concentration losses. Pin-type design, as one of the widely utilized flow field configurations, has the advantage of low pressure drop but the disadvantage of uneven flow distribution and stagnant areas. In this paper, a network-based optimization model was developed to optimize the pin-type flow field configuration. Two optimization cases, uniform flow distribution with and without considering reactant consumption along flow channels, were investigated and the corresponding optimized designs were developed. Three-dimensional numerical simulations of PEM fuel cell were conducted to validate the proposed optimization model and also to compare the performance of the fuel cells using the optimized designs and the regular pin-type design. The numerical results verified the designs generated with the

present optimization model. Both the optimized designs exhibited substantially higher fuel cell performance compared to the regular pin-type configuration. Moreover, the optimized design with considering reactant consumption performed even better than the one without considering the consumption, emphasizing the significance of reactant consumption in the flow field optimization model.

Keywords: Optimization model; Pin-type configuration; Flow field; Flow distribution; PEM fuel cell.

1. Introduction

As an energy conversion device, polymer electrolyte membrane (PEM) fuel cell has great advantages such as low-temperature operation, high power density, fast start-up, system robustness, and low emissions. It is a very promising alternative power conversion device for portable electronics, automotive applications, and off-grid power supplies [1]. The flow field of a bipolar plate distributes fuel gases to reaction sites and removes reaction products (i.e., liquid water) out of the fuel cell, significantly affecting the performance of PEM fuel cells. Past studies have demonstrated that the power density of a fuel cell could be improved greatly by properly designing the flow fields [2-7].

Mathematic models have been developed by researchers to optimize flow field designs in order to improve PEM fuel cell performance. These models can be categorized into three approaches, namely, numerical simulation models, analytical models, and network

models (also called discrete analytical models) [8]. Wang et al. [9] integrated a conjugated-gradient scheme and a three-dimensional fuel cell numerical model to enhance the oxygen transport rate and local current density by optimizing the depth of tapered flow channels of serpentine designs. Jang et al. [10] combined a simplified conjugate-gradient method and a CFD code to maximize the current density by optimizing the baffles locations within an interdigitated configuration. Xing et al. [11] developed a self-automated geometry optimization approach by integrating a commercial software COMSOL Multiphysics^{TM} for fuel cell simulation and MATLAB for optimization. They investigated an air-breathing PEM fuel cell and optimized the channel-to-rib ratio at the anode and the open ratio at the cathode in order to achieve a higher fuel cell power density. Numerical simulation models are usually more accurate, but they cost more computational time and money, especially for the purpose of optimization because the CAD model and corresponding mesh have to be regenerated for new geometrical parameters at each iteration step.

Analytical models have been developed by establishing fluid mechanics principles in a set of straight channels to study the flow distribution and pressure drop in a flow field. Maharudrayya et al. [12, 13] developed one-dimensional models based on mass and momentum balance equations in the inlet and exhaust gas headers for Z- and U-type parallel-channel configurations as well as multiple parallel-channel configurations. The resulting coupled ordinary differential equations were analytically solved to obtain explicit solutions for the flow distribution in the individual channels and for the pressure drop over the entire flow field. Wang et al. [8, 14] also developed a general analytical

model based on mass and momentum conservation to explicitly calculate the flow distribution and pressure drop in parallel-channel configurations.

In a network model, channel networks are described analogically as electric circuit networks. Similar to Ohm's law, pressure drop is assumed to be proportional to flow rates. The relationship among pressure drop, flow rate and flow resistance could be built using the Hagen-Poiseuille equation. The advantages of the network method are its flexibility for establishing complex networks and easy application to various flow configurations. Tondeur et al. [15, 16] developed a network based model to investigate the flow and pressure distribution in 2D intersecting channels (meshes) with different numbers of meshes. A uniform flow distribution in rectangular lattice networks was achieved by configuring the flow resistances on the periphery of the lattice. Peng et al. [17] and Zhang et al. [18] proposed a flow network based model to calculate the flow distribution within interdigitated and parallel channels and optimize the dimension of each channel in order to obtain an even flow distribution. Peng et al. [19] found that the inhomogeneous compression of the gas diffusion layer (GDL) would cause the GDL intrude into the channels and eventually change the flow distribution. Therefore, they proposed a multi-objective optimization model based on the network approach to eliminate the non-uniform distribution in the flow field by taking the GDL intrusion into account.

As one of the commonly utilized configurations, pin-type configuration provides low pressure drop because of the multiple flow paths, but non-uniform flow and stagnant

areas tend to occur at various places of the channels. This significantly decreases the reactants transport efficiency and thus the overall fuel cell performance. Therefore, it is necessary and valuable to investigate and optimize the flow distribution of pin-type configuration in order to eliminate the stagnant areas and hence improve its performance. To our knowledge, no study has been reported on optimizing pin-type configuration for PEM fuel cell so far. Additionally, previously reported analytical models and network models have treated the flow rate over the flow field as constant and have not taken the consumption of reactant gases along the flow channels by electrochemical reactions into consideration. Reactant consumption has a significant effect on the flow field designs as it dramatically changes the flow distribution in a fuel cell. For example, as reactant gases flow through a fuel cell, the flow rate gradually decreases due to the reactant consumption, and hence the channels near the inlet transport higher flow rates than those near the outlet. If the typical input stoichiometry of 2.0 is used, the difference between the flow rates at inlet and outlet could be as high as 50%.

In the present study, an optimization model of pin-type configuration was developed based on the network approach. The model was constructed by establishing the flow relationships over the entire channel network and then setting objective function and constraints, and solved using the Quasi-Newton algorithm. In order to demonstrate the effect of reactant consumption on the flow field designs, two different optimization scenarios, uniform flow velocity distribution with and without considering reactant consumption, were investigated and compared. A three-dimensional, two-phase numerical simulation model of PEM fuel cell was applied to study the flow distribution

of the optimized designs in the entire fuel cell unit and to validate the proposed optimization model. Finally, the fuel cell performance of the optimized designs was compared with that of the regular pin-type design, to investigate how these optimized designs would influence the final fuel cell performance.

2. Optimization Model

2.1 Flow relationship

The optimization model was developed based on the following assumptions:

1) The flow is laminar;
2) The reactant gases are viscous and incompressible;
3) A constant resistance coefficient, which is estimated empirically, exists at each junction of channels;
4) Reactants are consumed uniformly over the entire active area. Uniform consumption of reactants is a desirable situation for flow field designs. Pin-type designs normally could not achieve this situation due to stagnant areas. However, after optimization the optimized pin-type design would be very close to uniform consumption, since the optimization model uses uniform flow distribution as the objective function, which ensures uniform reactant supply and leads to uniform consumption in the optimized design.

A pin-type configuration can be represented as a lattice channel network and each channel is treated as a link connecting two nodes, as shown in Fig. 1. A flow field

composed of $N \times M$ nodes is considered and the total number of channels is $2NM - N - M$. Channel (k, l) is designated as the channel connecting two neighboring nodes designated by k and l. For the Hagen-Poiseuille flow, the relationship between pressure drop and flow rate in each channel (k, l) is

$$\Delta p_{kl} = \frac{128 \mu L_{kl} q_{kl}}{\pi {D_{kl}^h}^4} \tag{1}$$

where μ is the fluid viscosity, L_{kl} is the channel length, q_{kl} is the volumetric flow rate, D_{kl}^h is the hydraulic diameter. For a channel with rectangular cross-section (width: w, depth: d), the hydraulic diameter is

$$D_{kl}^h = \frac{4A_{kl}^c}{P_{kl}^c} = \frac{2w_{kl}d_{kl}}{w_{kl}+d_{kl}} \tag{2}$$

where A_{kl}^c and P_{kl}^c are the channel's cross-sectional area and perimeter, respectively. The volumetric flow rate is

$$q_{kl} = v_{kl} A_{kl}^c \tag{3}$$

where v_{kl} is the average flow velocity in the channel. Analogy to an electric circuit network, the pressure drop in Equation (1) can be expressed in terms of flow rate and flow resistance as

$$\Delta p_{kl} = r_{kl} q_{kl} \tag{4}$$

where r_{kl} is the flow resistance in the channel, which is related to the channel's geometric dimensions

$$r_{kl} = \frac{128 \mu L_{kl}}{\pi {D_{kl}^h}^4} \tag{5}$$

To take the pressure losses at the conjunction of channel segments into account, a constant resistance coefficient of 3.6e5 [16], r_c, is introduced to the flow resistance, r_{kl}, in equation (5)

$$r_{kl} = \frac{128\mu L_{kl}}{\pi D_{kl}^{h\,4}} + r_c \tag{5'}$$

Two cases were considered to establish the mass conservation equations in this study: 1) without reactant consumption, and 2) with uniform reactant consumption.

1) Mass conservation without reactant consumption

For a given node k, the sum of all the in-flow rates (+) and the out-flow rates (-) should equal to zero,

$$\sum_k q_{kl} = 0 \tag{6}$$

where $\sum_k$ indicates the summation of all the channels connected to the node k. Substituting Equation (4) into (6), a linear equation system of pressure can be established for each node k

$$\sum_k \frac{\Delta p_{kl}}{r_{kl}} = \sum_k \frac{P_l - P_k}{r_{kl}} = 0 \tag{7}$$

This equation system has $N \times M$ equations and $N \times M$ unknowns, which consist of the pressure value at each node. By solving them, the pressure at every node can be determined. In a pin-type configuration, there are three types of conjunctions, T corner, L corner and 90° cross, as shown in Fig. 1. For each type of conjunction, including the inlet and outlet of the flow field, Equation (7) can be expressed, respectively, as

T corner:

$$\frac{P_{i,j-1} - P_{i,j}}{r_{(i,j)(i,j-1)}} + \frac{P_{i,j+1} - P_{i,j}}{r_{(i,j)(i,j+1)}} + \frac{P_{i+1,j} - P_{i,j}}{r_{(i,j)(i+1,j)}} = 0 \tag{8-1}$$

L corner:

$$\frac{P_{i,j-1} - P_{i,j}}{r_{(i,j)(i,j-1)}} + \frac{P_{i+1,j} - P_{i,j}}{r_{(i,j)(i+1,j)}} = 0 \tag{8-2}$$

90° cross:

$$\frac{P_{i,j-1}-P_{i,j}}{r_{(i,j)(i,j-1)}}+\frac{P_{i-1,j}-P_{i,j}}{r_{(i,j)(i-1,j)}}+\frac{P_{i+1,j}-P_{i,j}}{r_{(i,j)(i+1,j)}}+\frac{P_{i,j+1}-P_{i,j}}{r_{(i,j)(i,j+1)}}=0 \quad (8\text{-}3)$$

Inlet node:

$$Q+\frac{P_{1,2}-P_{1,1}}{r_{(1,1)(1,2)}}+\frac{P_{2,1}-P_{1,1}}{r_{(1,1)(2,1)}}=0 \quad (8\text{-}4)$$

Outlet node:

$$\frac{P_{N-1,M}-P_{N,M}}{r_{(N,M)(N-1,M)}}+\frac{P_{N,M-1}-P_{N,M}}{r_{(N,M)(N,M-1)}}-Q=0 \quad (8\text{-}5)$$

where subscripts (i,j) represent the coordinates of the nodes of channel network.

2) Mass conservation with uniform reactant consumption

During a fuel cell operation, the total flow rate in channels keeps decreasing from inlet to outlet since the reactant gases are consumed gradually by electrochemical reactions. This makes the flow characteristics substantially different from the one with constant flow rate (without reactant consumption). For improving flow field optimization and therefore enhancing fuel cell performance, it is necessary to take the reactant consumption into consideration. Since reactants are assumed to be consumed uniformly over the entire active area, that is, at each node, $Q/(\eta(N\times M))$ is consumed, where Q is the inlet flow rate and η represents the stoichiometry. Therefore, Equations (6) and (7) are modified to

$$\sum_k q_{kl}=\frac{Q}{\eta(N\times M)} \quad (9)$$

$$\sum_k \frac{P_k-P_l}{r_{kl}}=\frac{Q}{\eta(N\times M)} \quad (10)$$

2.2 Objective function

Uniform flow velocity distribution could reduce the stagnant areas in pin-type configuration and hence improve the fuel cell performance. To achieve the state of uniform flow distribution, the standard deviation of flow velocity of all channels was used as the objective function:

$$Minimize\ E = \sqrt{\frac{\sum_{(k,l)}(v_{kl}-\bar{v})^2}{2NM-N-M}} \tag{11}$$

where $\sum_{(k,l)}$ indicates the sum of all the channels, and $\bar{v} = \frac{\sum_{(k,l)} v_{kl}}{2NM-N-M}$ is the mean flow velocity.

2.3 Constraints

The total channel surface area directly influences the mass transport efficiency and the electrical conductivity of bipolar plate. The total surface area of all the channel segments is

$$S_c = \sum_{(k,l)} L_{kl} w_{kl} \tag{12}$$

A larger total surface area of all channels would be good for mass transport but would reduce the conduction of electricity due to the smaller contact area between bipolar plates and gas diffusion layers. Therefore, a compromise between mass transport and electrical conductivity is needed in order to decide a proper channel surface area. For the purpose of providing an illustrated example, a typical channel surface area of 60% was used in this work [4], i.e.,

$$S_c = 0.6A \tag{13}$$

where A is the active area of the fuel cell. In addition, considering the feasibility of bipolar plate, the channel width was restricted to the range of 0.5-2.5 mm, i.e.,

$$0.5 \leq w_{kl} \leq 2.5 \tag{14}$$

2.4 Solving optimization problem

The model was formatted into a constrained optimization problem with channel widths as design variables. A MATLAB optimization tool box with quasi-Newton algorithm was employed and the corresponding program was developed to solve this problem. To start the calculation, an initial set of channel width values (e.g., 1.5 mm for all channels) was used. Then, the flow resistance for each channel was determined from Equation (5′) and the pressure value at each node was calculated by solving the linear equation system given by either Equation (7) or Equation (10). Subsequently, the flow velocity in each channel was obtained from Equations (4) and (3). The iteration process continued until the minimum velocity deviation was achieved following either Equation (11). Two optimization cases were investigated, including optimized I design which did not consider the reactant consumption along the flow channels and optimized II design which considered the reactant consumption. For each case, both flow fields with 3×3 (active area: 10×10 mm^2) and 11×11 nodes (active area: 50×50 mm^2) were investigated. 3×3 nodes design was used to validate the optimization model while 11×11 nodes design was used to obtain a practical flow field design. Table 1 gives the values of the flow field parameters used in the optimization model. It should be noted that although the

optimization was performed for the anode, it would be valid for cathode too, since anode and cathode sides are essentially the same in terms of flow distribution. Although liquid water would be generated in the cathode, the optimization model presented in this paper is still valid for the cathode. Also, although the optimized design was developed under one unique mass flow rate, it is also an optimal configuration for other flow rates, because the flow resistance of a flow field only relates to the geometrical dimensions of the flow channels but not to the flow rates, as indicated in Equation (5).

3. Numerical Simulation

A three-dimensional, two-phase finite element method (FEM) simulation model [20-25] was used to validate the proposed optimization model and to investigate the performance of PEM fuel cells using the optimized designs discussed above. Since the proposed optimization model could not directly use fuel cell performance as the objective function, it was necessary to numerically investigate the fuel cell performance of these optimized designs in order to quantify how the designs would affect the fuel cell performance. The FEM simulation model included continuity, momentum and species equations for the transport phenomena of the species within the fuel cell. Current density distribution was obtained by solving the electron and proton transport equations. Electrochemical reactions in the catalyst layers were characterized by the Butler-Volmer equation. Water content in the membrane and water saturation in other components was considered to model liquid water formation and transport inside the fuel cell. The detailed governing

equations involved in the PEM fuel cell transport phenomena can be found in reference [26].

A PEM fuel cell module from the commercial software ANSYS Fluent was employed to solve the governing equations. Model parameters, given in Table 2, were based on Iranzo's reports [26, 27], which have verified that these parameters could provide a very accurate prediction of the experimental results. The PEM fuel cells using the optimized flow field designs and the regular pin-type design were studied using this numerical model under the operation conditions given in Table 3. The total number of volume elements in the entire fuel cell computation domain was around 573,000 for each design. The total numbers of volume elements were around 85,250 and 55,120, in the flow channel and GDL, respectively. The convergence criteria were set to 10^{-7} all equations. The velocity distribution within the flow field and fuel cell polarization curves were obtained and studied. The accuracy of the presented optimization model was verified by comparing the analytical results from the optimization model with the numerical results from the FEM simulation. Besides the PEM fuel cell simulation model, a model simulating only the flow in channels, referred as channel flow simulation model, was also developed to study the case of the optimized I design, in which no reactant consumption was considered.

4. Results and Discussion

4.1 Optimized designs with 3×3 nodes

Figure 2 shows the variation in the standard deviation of velocity at each iteration step for both designs with 3×3 and 11×11 nodes in the case of considering reactant consumption. Different initial guess values of 1.0 mm, 1.5 mm and 2.0 mm were used, and the optimization model converged to the same point, indicating that the present model was not sensitive to initial values. In Fig. 2(a), the standard deviation of flow velocity in the design with 3×3 nodes reduced from as high as 11.00 before optimization to only 0.007 after optimization, demonstrating that the optimization algorithm worked properly. Figure 3 shows the channel width and flow velocity in each channel before and after optimization for the case of considering reactant consumption. Figure 3(a) shows that the velocity in each channel varied significantly as expected when a constant channel width of 1.5 mm was used. The velocity in these channels near the inlet and outlet was much higher than those at the middle of the flow field, and the velocity distribution was symmetric along the diagonal of inlet and outlet, because of the symmetric characteristic of pin-type configuration. Another point worth mentioning is that the velocity of the two channels connecting to the inlet was about twice of the velocity of the two connecting to the outlet, demonstrating the setting of the optimization model that half of the reactant was consumed as it went across the flow field in this case. After optimization, a uniform flow velocity distribution was achieved as shown in Fig. 3(b) where every channel had essentially the same velocity magnitude. The channel width distribution after optimization was also symmetric along the diagonal of the inlet and outlet. This agreed with the symmetric flow situation within a pin-type configuration.

4.2 Validation of optimization model

4.2.1 Case for not considering consumption

The numerical simulation results for pin-type designs with 3×3 nodes were investigated and compared to the analytical results to validate the optimization model. Since the numerical simulation model used has been experimentally verified by other researchers, as mentioned in Section 3, it is a reliable source to confirm the accuracy of the optimization model. Experimental study will be carried out to validate the optimization model in the future. Figure 4 shows the numerical results obtained from the channel flow simulation model for the regular pin-type design and the optimized I design. In the regular pin-type design (Fig. 4(a)), the flow velocities in the two channels near inlet and the two channels near outlet were much higher than the other channels. Most of the reactant flowed through the peripheral channels while very little reactant went through the inner four channels. After optimization, Fig. 4(b) clearly shows that a uniform flow distribution was achieved in the channels of the optimized I design.

Mean values of the velocity magnitude of each channel from both the optimization model and channel flow simulation model were compared in Fig. 5. For the numerical results, the mean value was obtained by integrating velocity at the middle cross-section of each channel normalized by the cross-sectional area. Both Figs. 5(a) and 5(b) show that the analytical results were very close to the numerical results, confirming that the optimization model was accurate enough to predict the flow properties in the pin-type

configuration. Additionally, compared with the regular pin-type design in Fig. 5(a), the optimized I design in Fig. 5(b) had nearly the same mean velocity in each channel, indicating again that the optimization model worked properly.

4.2.2 Case for considering consumption

Figure 6 shows the velocity distribution of the anode channels obtained from the PEM fuel cell simulation model for three different designs, regular pin-type, optimized I, and optimized II. The regular pin-type design in Fig. 6(a) had a higher flow velocity in the channels near the inlet than that in the other channels. However, different from the one in Fig. 4(a), the flow velocity in the channels near the outlet was lower than that at the inlet due to the consumption of reactant along the flow channels. Although the optimized I design showed a uniform flow distribution when only flow in channels was considered, it did not provide an optimum distribution in a real fuel cell operation. As shown in Fig. 6(b), the velocity in the channels at the half flow field near the outlet was lower than that at the other half near the inlet. In contrast, by considering the reactant consumption, the optimized II design improved the flow velocity distribution, as shown in Fig. 6(c), and provided a much more uniform flow distribution than the other two designs when used in a fuel cell unit.

Figure 7 shows the comparison of the mean velocities from the optimization model and the PEM fuel cell simulation model. The results for regular pin-type design and optimized II design are shown in Figs. 7(a) and 7(b), respectively. The analytical results

from the optimization model with considering the reactant consumption agreed well with the numerical results of the three-dimensional PEM fuel cell simulation model. The negligible errors could be resulted from the approximation of the flow resistance at corners and junctions, and the non-uniform reactant consumption rates at different areas of the flow field in fuel cell operation.

4.3 Optimized designs with 11×11 nodes

Figure 2(b) shows that the standard deviation of flow velocity decreased dramatically from 5.2 to around 0.2 after optimization for the optimized II design with 11×11 nodes. The optimization results are shown in Fig. 8 and also the corresponding CAD models constructed from the optimized channel dimension data. Figure 8(a) shows the initial mesh of a 50×50 mm^2 flow field with a constant channel width of 1.5 mm and the corresponding CAD model is shown in Fig. 8(d). Figures 8(b) and 8(e) show that the channel width in the optimized I design was symmetric along both the diagonals from the inlet to outlet and from the top left to bottom right, while, for the optimized II design in Figs. 8(c) and 8(f), the channel width distribution was symmetric only along the diagonal of the inlet and outlet, and the channels at the half flow field near the inlet side were wider than those near the outlet side (divided by the diagonal of the top left to bottom right, as indicated in Fig. 8(b)). This is because that in the case of the optimized I design the total flow rate kept constant along the entire flow field and therefore there was no difference between the flow channels near the inlet and those near the outlet, but for the optimized II design the flow rate kept decreasing along the flow field due to reactant

consumption and hence the channels near the outlet were narrower than those near the inlet. It is worth mentioning that although these optimized designs have varied channels, they can be easily fabricated with the Selective Laser Sintering process developed in our previous studies [28-30].

4.4 Comparison of flow distribution

Figure 9 shows the velocity distribution in the flow channels of anode from the PEM fuel cell simulation model. To give a detailed comparison, the flow velocity magnitudes in the channels along x direction (as indicated in Fig. 9(a)) are plotted in Fig. 10. The velocity distribution in the channels along y direction was the same as that along x direction, because the flow velocity distribution was symmetric along the diagonal of the inlet and outlet as can be seen in Fig. 9.

As shown in Figs. 9(a) and 10(a), the regular pin-type design had a much higher velocity at the area of inlet and outlet but a much lower velocity at the area of top left and bottom right corners, where some of the channel segments had nearly zero velocity, implying poor mass transport and water removal ability. In contrast, the flow velocity distribution was nearly uniform in the optimized II design, except a few channel segments near the inlet and outlet, as shown in Figs. 9(c) and 10(c). In Fig. 10(c), all the middle channels had similar flow velocities although the beginning of the 1^{st} and 2^{nd} channels and the ending of the 11^{th} channel had a higher velocity, which was due to the higher volumetric flow rates in these channels as well as the limitation on the maximum channel width (i.e.,

2.5 mm in Equation (14)) restricting the further reduction of the velocities in these channels. No stagnant areas were found in any of the channels of the optimized II design since all the velocity was greater than 0.3 m/s, as shown in Fig. 10(c).

The optimized I design did not take the reactant consumption into consideration, which, however, had a significant effect on fuel cell flow field designs. Comparison of Figs. 10(b) and 10(c) clearly shows that the optimized II design had a much more uniform flow distribution than the optimized I design. Figure 10(b) shows that flow velocity had a large divergence at the beginning and the ending of each channel. The reason was that, without considering the reactant consumption, the channel dimension tended to be larger than needed and consequently the velocity decreased dramatically at the channel segments that were far away from the inlet and outlet, e.g., at the beginning of the 11^{th} channel and the ending of the 1^{st} channel in Fig. 10(b). These places can easily form stagnant areas.

The standard deviations and average flow velocities obtained from the PEM fuel cell simulation model for the three different designs are given in Table 4. The average flow velocities for the three designs were essentially the same. The small difference was caused by round-off errors. However, the optimized II design had the lowest velocity deviation, around 0.167, while the regular pin-type design had the highest deviation of 2.379. If only the inner channels were considered (Fig. 9(c)), the standard deviation for the optimized II design was even lower, only 0.052.

Figure 11 shows the water saturation distribution in the cathode GDL for the regular pin-type design and the optimized II design. The water saturation describes the ratio of the volume occupied by the liquid water to the total volume of the porous medium. A higher degree of water saturation means a higher possibility of flooding in these areas. Figure 11(a) shows the regular pin-type design has higher water saturation, as expected, especially around the upper and right edges. This is because the flow velocities in these areas were low, as seen from Fig. 9(a), and also the water from upstream accumulated in these areas. As a comparison, the optimized II design showed significant reduction on water saturation inside the GDL, indicating that the optimized II design enhanced the water removal capability. The optimized II design had a uniform and high flow velocity distribution (> 0.3 m/s in all the channels) and water could be easily removed in all the channels, while the regular pin-type design had large nearly-zero-velocity areas (stagnant areas) and thus liquid water tended to accumulate in these places and blocked the channels. From this point of view, although the liquid water was not directly considered in the optimization model, the uniform flow velocity distribution, which was the objective function of the optimization model, did imply a good water removal capability of a flow field. Therefore, the optimized II design did solve the major drawback of water flooding in the regular pin-type design.

4.5 Fuel cell performance

Figure 12 shows the polarization curves of the three different designs from the PEM fuel cell simulation. Both the optimized designs, regardless of considering reactant

consumption or not, showed a substantially better performance than the regular pin-type design, indicating that the proposed optimization model can improve the pin-type design and the fuel cell performance by optimizing the flow velocity distribution. By taking the reactant consumption into consideration, the optimized II design further improved the fuel cell power density by about 10% compared to the optimized I design because the former model was closer to the real fuel cell operation, and as such, the optimized result was more accurate and the flow distribution was more uniform. The uniform flow distribution can circumvent the two essential drawbacks of the pin-type configuration, uneven flow and stagnant areas. Future work will include experimental studies of the fuel cell performance using these optimized designs to validate the numerical results obtained in the present paper.

5. Conclusions

In order to enhance the PEM fuel cell performance, an optimization model based on flow network was proposed to optimize the pin-type flow field configuration. Different optimization cases, optimized I design without considering reactant consumption and optimized II design with considering reactant consumption, were investigated. A three-dimensional, two-phase PEM fuel cell numerical model was built to validate the proposed optimization model and to study the performance of the fuel cells using the optimized flow field designs. The flow velocity distributions obtained from the numerical simulations agreed well with the results from the optimization model, showing that the optimized II design had the lowest standard deviation of flow velocity and thus the most

uniform flow distribution. In terms of fuel cell performance, both the optimized designs exhibited substantially higher performance than the regular pin-type design. The optimized II design performed 10% higher than the optimized I design, indicating it was essential for flow field optimization model to take the reactant consumption along the flow channels into consideration.

Acknowledgements

This paper is based upon work supported by the National Science Foundation under Grant #CMMI-1131659. Any opinions, findings, and conclusions or recommendations expressed in this paper are those of the authors and do not necessarily reflect the views of the National Science Foundation.

References

[1] Blunk R, Elhamid MH, Lisi D, Mikhail Y. Polymeric composite bipolar plates for vehicle application. J Power Sources 2006;156:151-7.

[2] Watkins DS, Dircks KW, Epp DG. Fuel cell fluid flow field plate. US Patent No. 5,108,849, 1992.

[3] Watkins DS, Dircks KW, Epp DG. Novel fuel cell fluid flow field plate. US Patent No. 4,988,583, 1991.

[4] Li X, Sabir I. Review of bipolar plates in PEM fuel cells: flow-field designs. Int J Hydrogen Energy 2005;30:359-71.

[5] Hamilton PJ, Pollet BG. Polymer electrolyte membrane fuel cell (PEMFC) flow field plate design, materials and characterisation. Fuel Cells 2010;10:489-509.

[6] Li X, Sabir I, Park J. A flow channel design procedure for PEM fuel cells with effective water removal. J Power Sources 2007;163:933-42.

[7] Misran E, Daud WRW, Majlan EH. Review on serpentine flow field design for PEM fuel cell system. Key Eng Mater 2010;447-448:559-63.

[8] Wang J. Theory of flow distribution in manifolds. Chem Eng J 2011;168:1331-45.

[9] Wang XD, Huang YX, Cheng CH, Jang JY, Lee DJ, Yan WM, Su A. An inverse geometry design problem for optimization of single serpentine flow field of PEM fuel cell. Int J Hydrogen Energy 2010;35:4247-57.

[10] Jang JY, Cheng CH, Huang YX. Optimal design of baffles locations with interdigitated flow channels of a centimeter-scale proton exchange membrane fuel cell. Int J Heat Mass Transfer 2010;53:732-43.

[11] Xing XQ, Lum KW, Poh HJ, Wu YL. Geometry optimization for proton-exchange membrane fuel cells with sequential quadratic programming method. J Power Sources 2009;186:10-21.

[12] Maharudrayya S, Jayanti S, Deshpande AP. Pressure drop and flow distribution in multiple parallel-channel configurations used in proton-exchange membrane fuel cell stacks. J Power Sources 2006;157:358-67.

[13] Maharudrayya S, Jayanti S, Deshpande AP. Flow distribution and pressure drop in parallel-channel configurations of planar fuel cells. J Power Sources 2005;144:94-106.

[14] Wang J. Pressure drop and flow distribution in parallel-channel configurations of fuel cells: Z-type arrangement. Int J Hydrogen Energy 2010;35:5498-509.

[15] Tondeur D, Fan Y, Luo L. Flow distribution and pressure drop in 2D meshed channel circuits. Chem Eng Sci 2011;66:15-26.

[16] Tondeur D, Fan Y, Commenge JM, Luo L, Uniform flows in rectangular lattice networks. Chem Eng Sci 2011;66:5301-12.

[17] Peng L, Lai X, Yi P, Mai J, Ni J. Design, optimization, and fabrication of slotted interdigitated thin metallic bipolar plates for PEM fuel cells. J Fuel Cell Sci Tech 2011;8:0110021-8.

[18] Zhang W, Hu P, Lai X, Peng L. Analysis and optimization of flow distribution in parallel-channel configurations for proton exchange membrane fuel cells. J Power Sources 2009;194:931-40.

[19] Peng L, Mai J, Hu P, Lai X, Lin Z. Optimum design of the slotted-interdigitated channels flow field for proton exchange membrane fuel cells with consideration of the gas diffusion layer intrusion. Renew Energ 2011;36:1413-20.

[20] Ferng YM, Su A. A three-dimensional full – cell CFD model used to investigate the effects of different flow channel designs on PEMFC performance. Int J Hydrogen Energy 2007;32:4466-76.

[21] Le AD, Zhou B. A general model of proton exchange membrane fuel cell. J Power Sources 2008;182:197-222.

[22] Hontanon E, Escudero MJ, Bautista C, Garcia-Ybarra PL, Daza L. Optimisation of flow-field in polymer electrolyte membrane fuel cells using computational fluid dynamics techniques. J Power Sources 2000;86:363-8.

[23] Barreras F, Lozano A, Valino L, Marin C, Pascau A. Flow distribution in a bipolar plate of a proton exchange membrane fuel cell: experiments and numerical simulation studies. J Power Sources 2005;144:54-66.

[24] Cheddie D, Munroe N. Review and comparison of approaches to proton exchange membrane fuel cell modeling. J Power Sources 2005;147:72-84.

[25] Manso AP, Marzo FF, Garmendia Mujika M, Barranco J, Lorenzo A. Numerical analysis of the influence of the channel cross-section aspect ratio on the performance of a PEM fuel cell with serpentine flow field design. Int J Hydrogen Energy 2011;36:6795-808.

[26] Iranzo A, Munoz M, Rosa F, Pino J. Numerical model for the performance prediction of a PEM fuel cell. Model results and experimental validation. Int J Hydrogen Energy 2010;35:11533-50.

[27] Iranzo A, Munoz M, Pino J, Rosa F. Update on numerical model for the performance prediction of a PEM fuel cell. Int J Hydrogen Energy 2011;36:9123-7.

[28] Guo N, Leu MC. Experimental study of polymer electrolyte membrane fuel cells using a graphite composite bipolar plate fabricated by selective laser sintering. Int SFF Symp, Austin Aug 2010;212-25.

[29] Bourell DL, Leu MC, Chakravarthy K, Guo N, Alayavalli K. Graphite-based indirect laser sintered fuel cell bipolar plates containing carbon fiber additions. CIRP Ann-Manuf Techn 2011;60:275-8.

[30] Guo N, Leu MC. Effect of different graphite materials on the electrical conductivity and flexural strength of bipolar plates fabricated using selective laser sintering. Int J Hydrogen Energy 2012;37:3558-66.

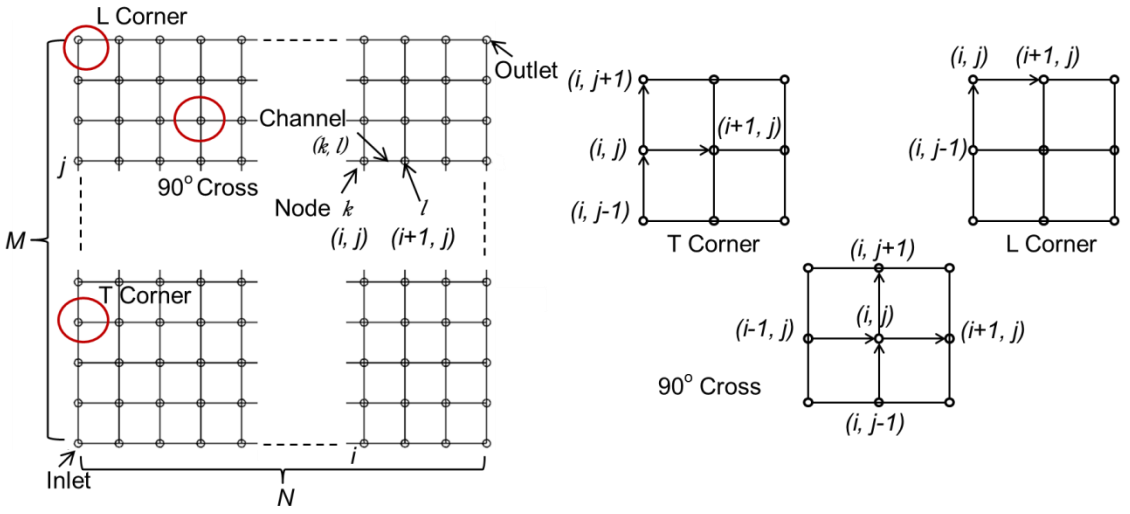

Fig. 1 Channel network of a pin-type flow field configuration with $N \times M$ nodes and three types of conjunctions, T corner, L corner and 90° cross.

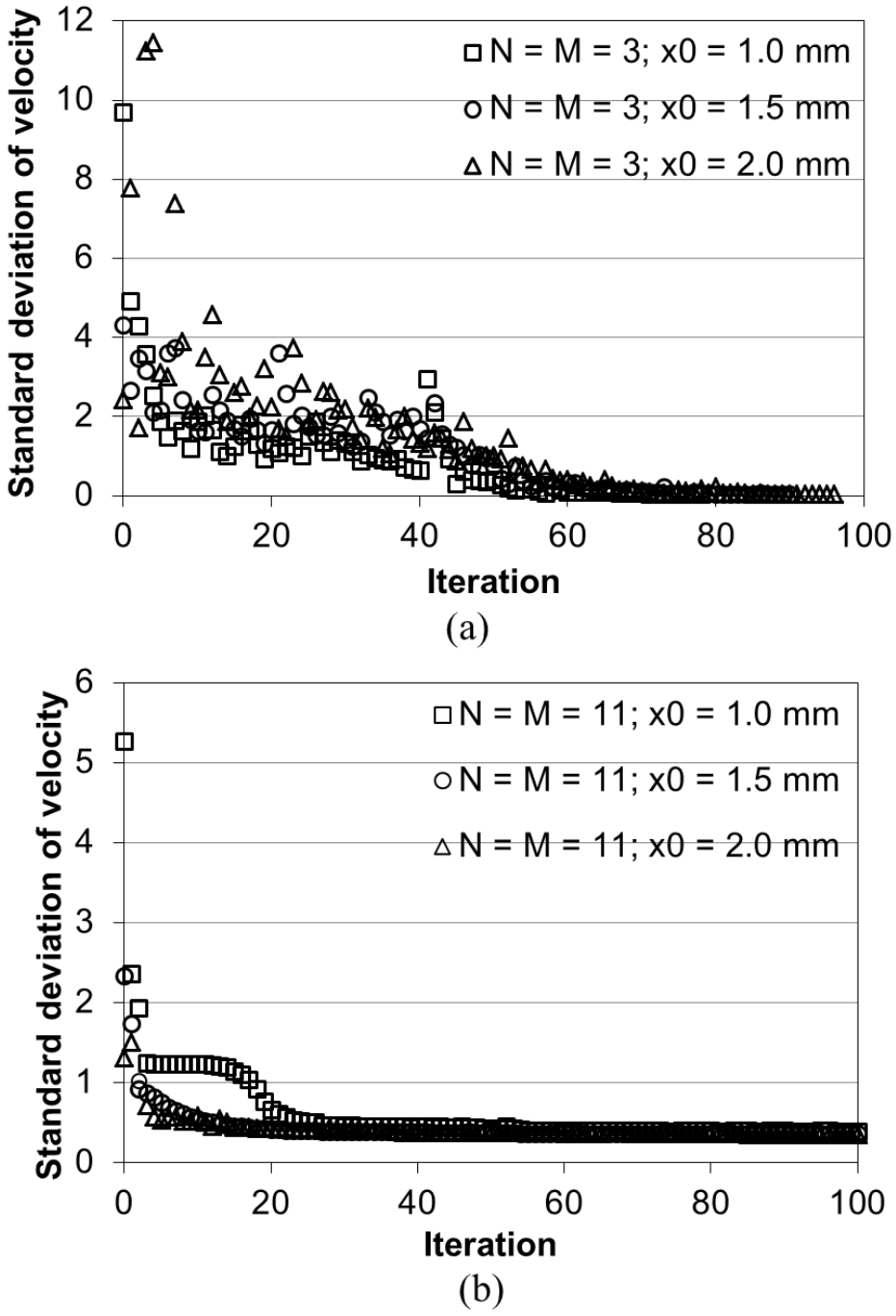

Fig. 2 Variation in the standard deviation of velocity at various iteration steps for the optimized II design with (a) 3×3 nodes and (b) 11×11 nodes.

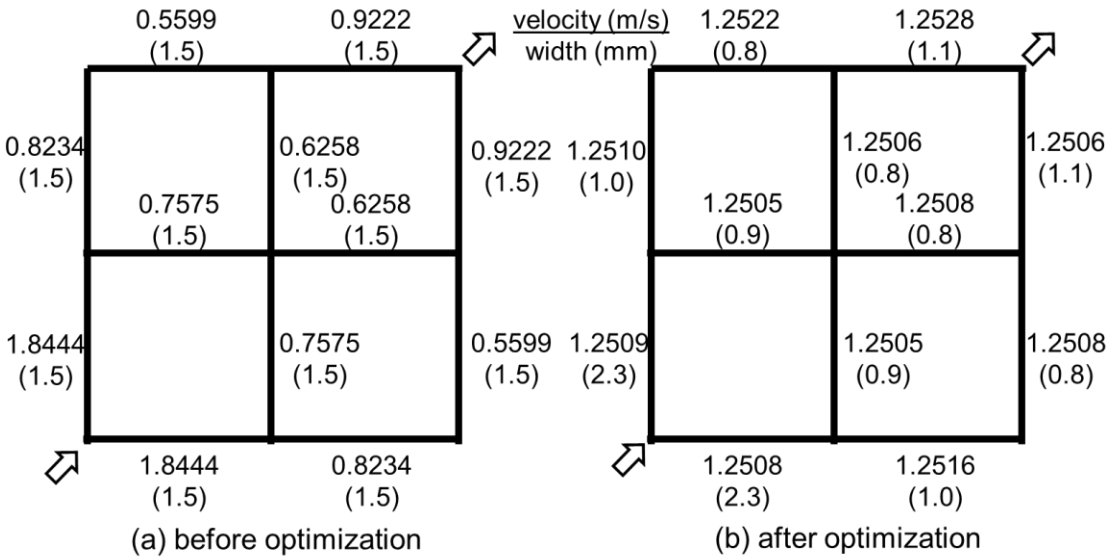

Fig. 3 Channel width (below) and flow velocity (above) of each channel (a) before and (b) after optimization in the case of considering reactant consumption.

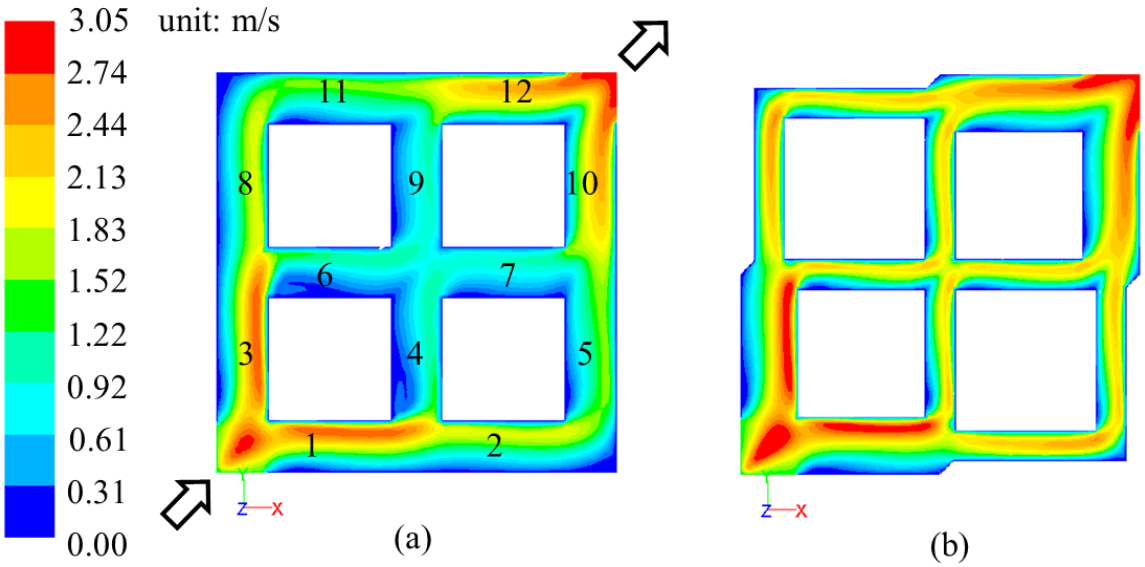

Fig. 4 Flow velocity distribution obtained from the channel flow simulation model for (a) the regular pin-type design and (b) the optimized I design.

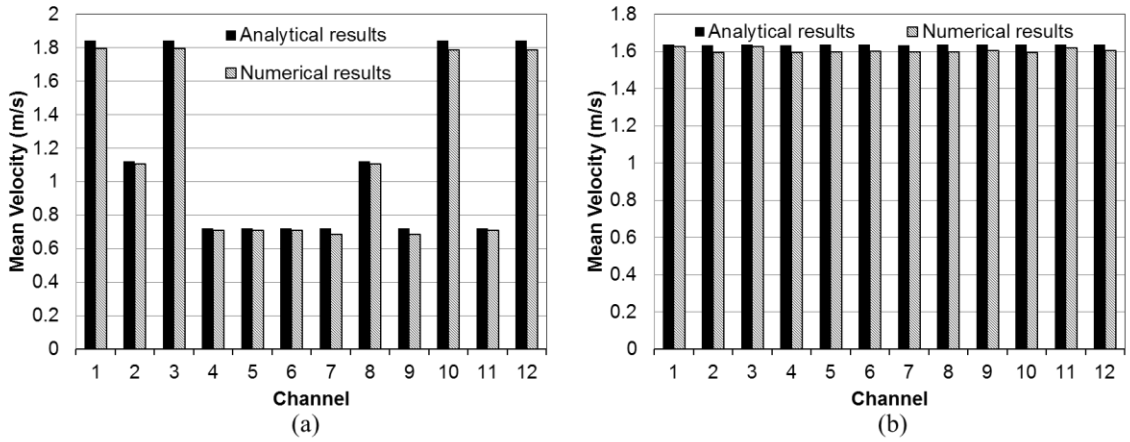

Fig. 5 Comparison of the analytical results from the optimization model and the numerical results from the channel flow simulation model, for (a) the regular pin-type design and (b) the optimized I design. The channel number was indicated in Fig.4 (a).

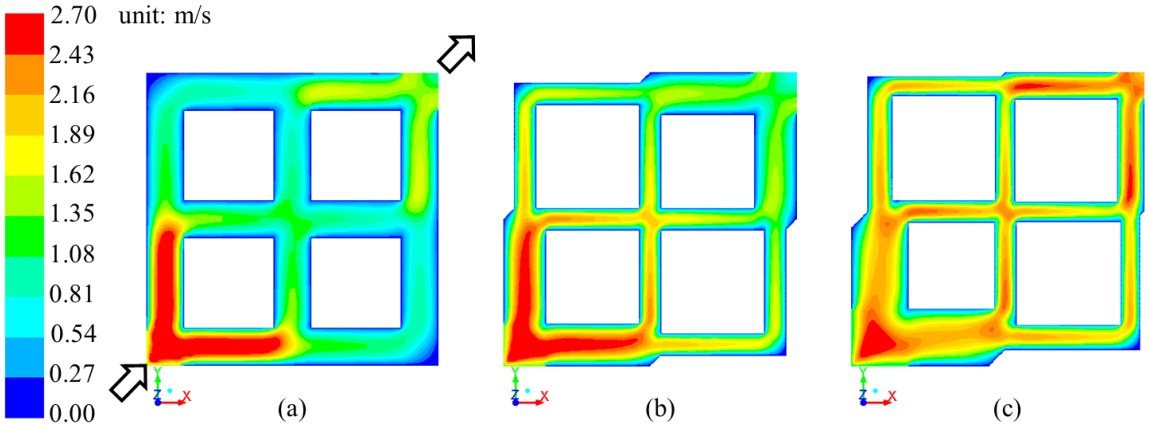

Fig. 6 Velocity distribution obtained from the PEM fuel cell simulation model for (a) the regular pin-type design, (b) the optimized I design, and (c) the optimized II design.

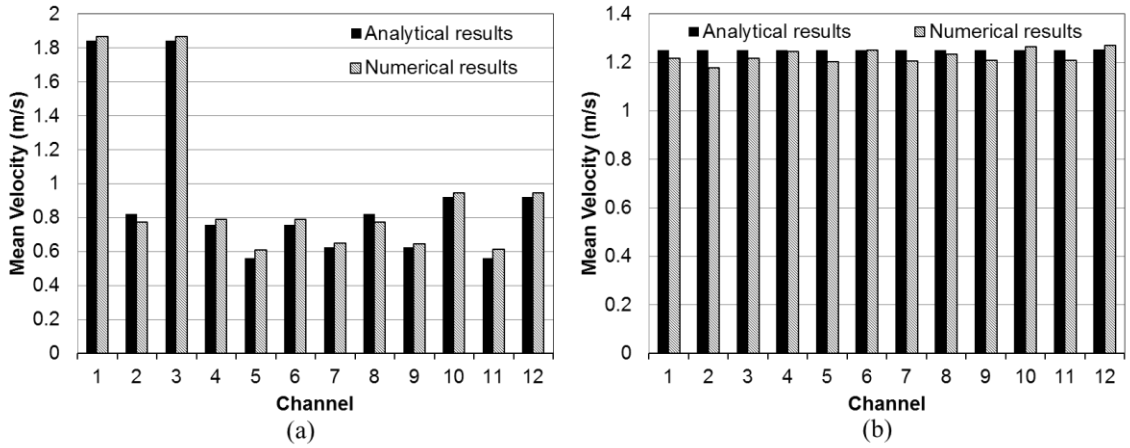

Fig. 7 Comparison of the analytical results from the optimization model and the numerical results from the PEM fuel cell simulation model, for (a) the regular pin-type design and (b) the optimized II design.

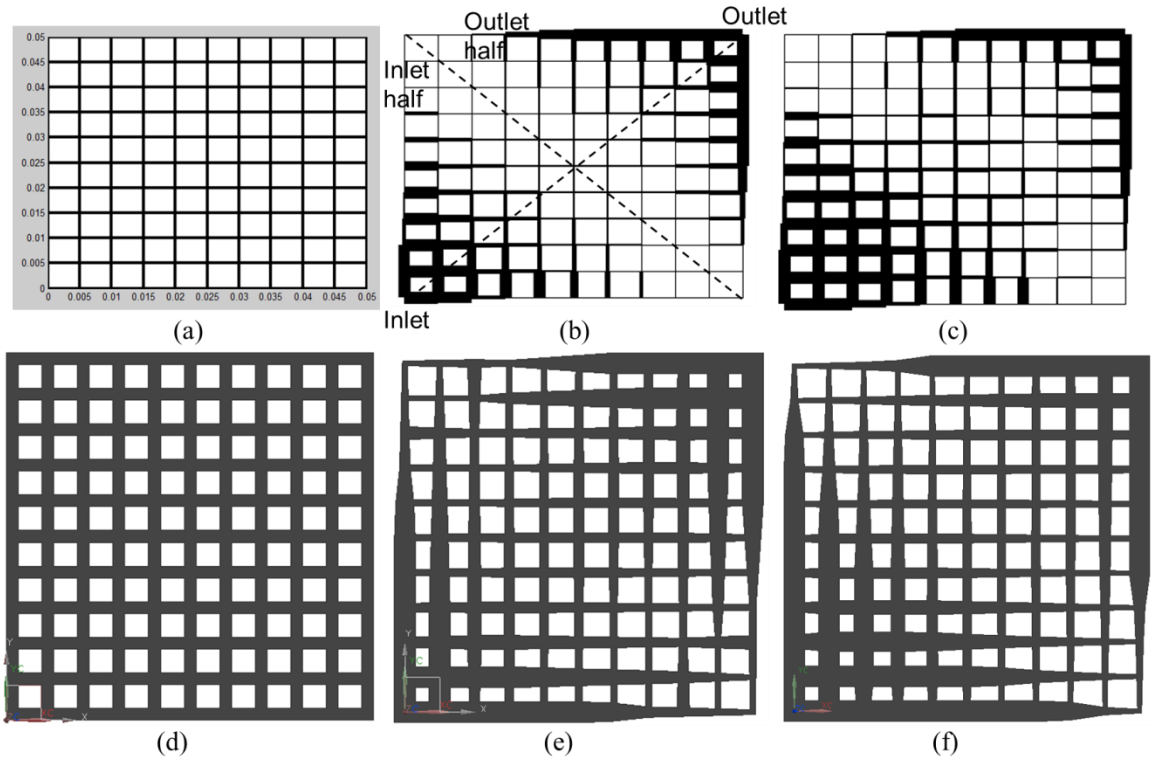

Fig. 8 Results from the optimization model and the corresponding CAD models for a flow field with 11×11 nodes: (a, d) initial regular pin-type design with constant channel width of 1.5 mm, (b, e) optimized I design, and (c, f) optimized II design.

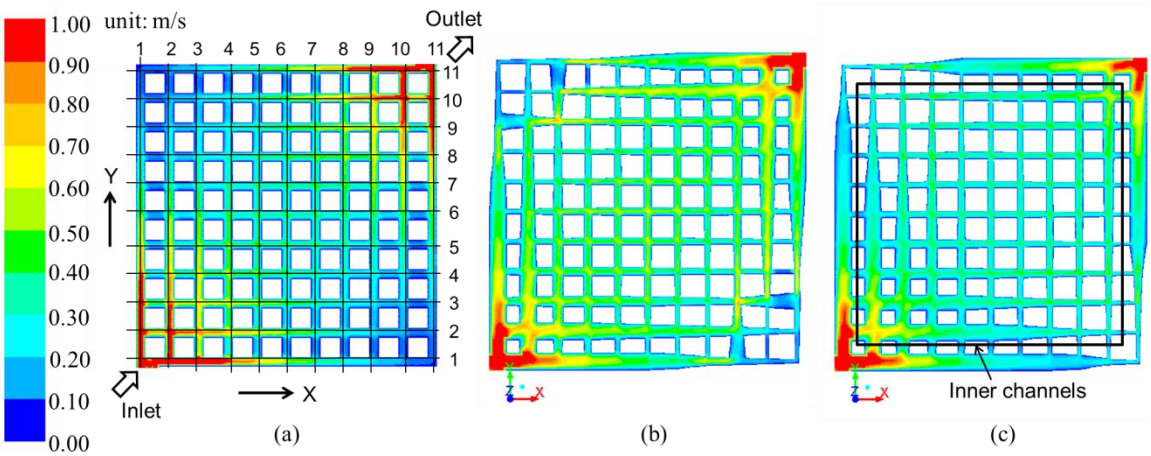

Fig. 9 Flow velocity distribution in the flow channels for (a) the regular pin-type design, (b) the optimized I design, and (c) the optimized II design.

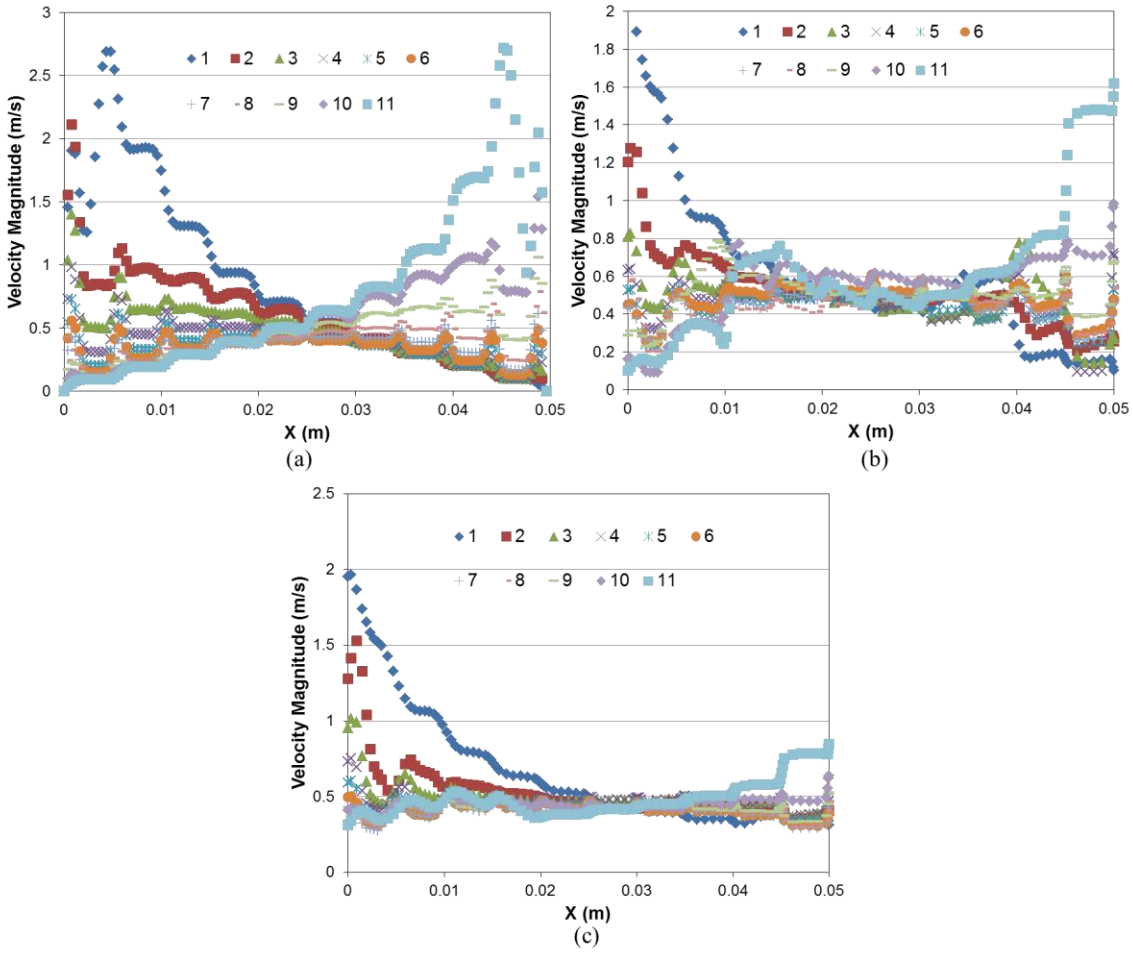

Fig. 10 Velocity distribution in the channels along x-direction for (a) the regular pin-type design, (b) the optimized I design, and (c) the optimized II design.

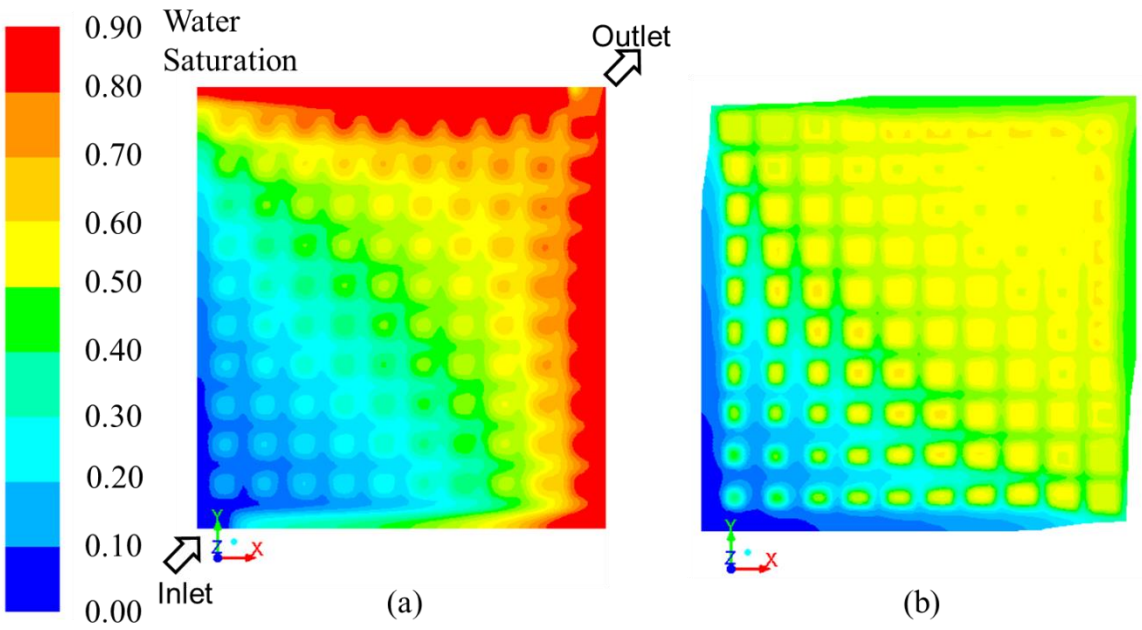

Fig. 11 Water saturation in the cathode GDL for (a) the regular pin-type design, and (b) the optimized II design.

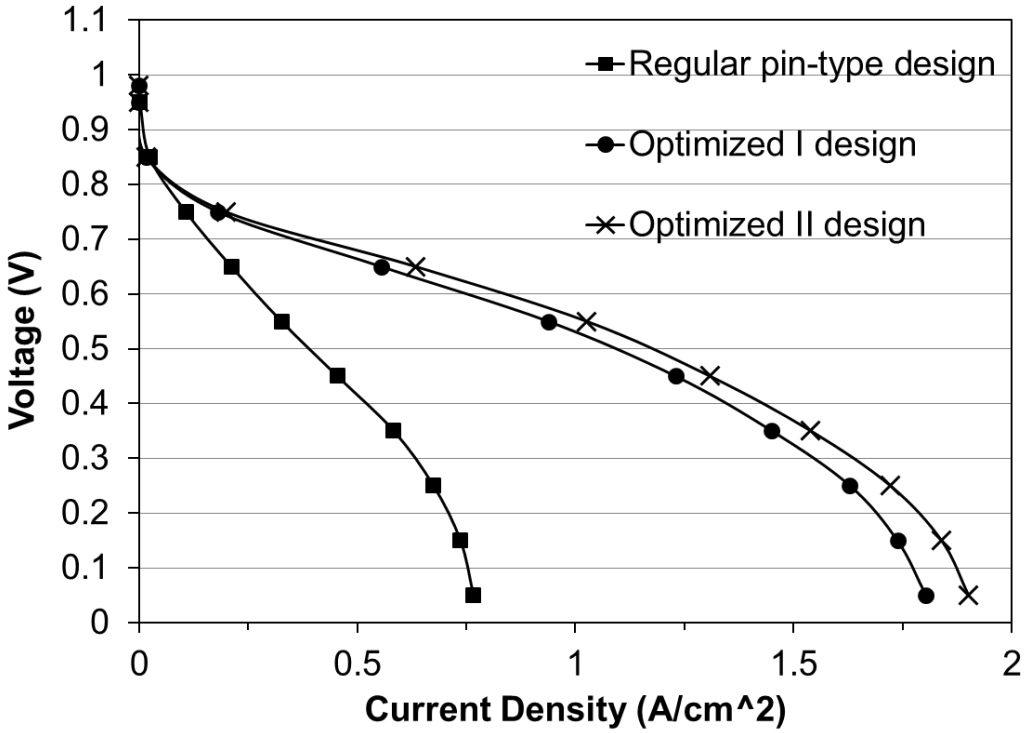

Fig. 12 Comparison of the polarization curves obtained from the PEM fuel cell simulations of the three different flow field designs. For each fuel cell simulation, the same flow field design was used for both the anode and cathode sides.

Table 1 Parameters in the optimization model.

Inlet flow rate	Stoichiometry	Active area	Channel depth	Fluid viscosity
4.3e-6 m^3/s	2.0	10×10 mm^2 (3×3 nodes) 50×50 mm^2 (11×11 nodes)	1.0 mm	9.93e-6 kg/m·s

Table 2 Parameters in the fuel cell simulation model.

Reference exchange current density at anode, referred to m^2 Pt (A/m^2 Pt)	4.48e5
Reference exchange current density at cathode, referred to m^2 Pt (A/m^2 Pt)	4.48
Charge transfer coefficient at anode	1.0
Charge transfer coefficient at cathode	1.0
Concentration exponent at anode	0.5
Concentration exponent at cathode	1.0
Pore blockage saturation exponent	2.0
Open circuit voltage (V)	0.98
H_2 diffusivity (m^2/s)	8.0e-5
O_2 diffusivity (m^2/s)	2.0e-5
H_2O diffusivity (m^2/s)	5.0e-5
Membrane equivalent weight (kg/kmol)	1100
Catalyst layer surface-to-volume ratio (1/m)	1.25e7
GDL electric conductivity ($1/\Omega$ m)	280
GDL porosity	0.82
GDL wall contact angle (deg)	110
GDL viscous resistance at anode ($1/m^2$)	1.0e12
GDL viscous resistance at cathode ($1/m^2$)	3.86e12
Bipolar plate electric conductivity ($1/\Omega$ m)	92600

Table 3 Operation parameters in the fuel cell simulation model for different flow field designs.

Operation temperature (K)	353
Operation pressure (atm)	1.0
Anode stoichiometry	2.0
Cathode stoichiometry	2.0
Relative humidity at anode (%)	0
Relative humidity at cathode (%)	100

Table 4 Standard deviation and average velocity in different designs with 11×11 nodes obtained from the PEM fuel cell simulation model.

Design	Standard deviation	Average velocity (m/s)
Regular pin-type design	2.379	0.4948
Optimized I design	0.259	0.5108
Optimized II design	0.167	0.5051

PAPER

III. Performance Investigation of PEM Fuel Cells Using Graphite Composite Plates Fabricated by Selective Laser Sintering

Nannan Guo

Department of Mechanical and Aerospace Engineering,

Missouri University of Science and Technology,

Rolla, MO 65409, USA

Email: ngzn6@mail.mst.edu

Ming C. Leu

Department of Mechanical and Aerospace Engineering,

Missouri University of Science and Technology,

Rolla, MO 65409, USA

Abstract

Selective Laser Sintering (SLS) was used to fabricate graphite composite plates for Polymer Electrolyte Membrane (PEM) fuel cells, which has the advantages of reducing time and cost associated with the research and development of bipolar plates. Graphite composite plates with three different designs, i.e., parallel in series, interdigitated, and bio-inspired, were fabricated using the SLS process. The performance of these SLS fabricated plates was studied experimentally within a fuel cell assembly under various

operating conditions. The effect of temperature, relative humidity, and pressure on fuel cell performance was investigated. In the tests conducted in this study, the best fuel cell performance was achieved with a temperature of 65 - 75 ℃, relative humidity of 100%, and back pressure of 2 atm. The performance of fuel cell operating over an extended time was also studied, with the result showing that the SLS fabricated graphite composite plates provided a relatively steady fuel cell output power.

Keywords: Selective Laser Sintering, PEM fuel cell, graphite composite plate, in-situ performance, operating parameters

1. Introduction

A Polymer Electrolyte Membrane (PEM) fuel cell is an electrochemical cell that converts chemical energy from hydrogen and oxygen into electrical energy. PEM fuel cell has great advantages such as high efficiency, low-temperature operation, high power density, and “green” emissions. The potential applications include portable power supply, automotive system and distributed power system. Bipolar plate, which constitutes more than 30% of the total cost in a fuel cell stack, is a vital component in a PEM fuel cell [1]. It supplies hydrogen and oxygen to reaction sites, removes the reaction products out of the fuel cell, and collects the generated current. Bipolar plate significantly influences the performance of a PEM fuel cell. The flow field configuration of a bipolar plate, which is used to distribute reactant gases, has a great effect on transport efficiency and thus fuel

cell concentration losses. Studies [2-5] have shown that the power density of a fuel cell can be increased significantly if the bipolar plate has a proper flow field design.

Graphite/polymer composites are promising materials for producing bipolar plates, due to their light weight and excellent chemical resistance [6-13]. Two fabrication methods for mass producing these bipolar plates are injection molding (IM) [6] and compression molding (CM) [7]. Although these methods are suitable for mass production, they are not time-efficient or cost-effective for research and development (R&D) of bipolar plates, because for each different design an expensive mold has to be fabricated. Selective Laser Sintering (SLS), as an additive manufacturing technology, has been applied to fabricate graphite composite bipolar plates for fuel cells [14-19]. Compared with CM and IM, SLS can fabricate graphite composite bipolar plates at a lower cost and a shorter lead time, especially for the purpose of researching and developing new bipolar plate designs. Compared with CNC machining, SLS process does not require any fixtures, has the ability to build flow channels with various cross-section shapes such as triangular and semi-circular, and enables more design feasibility. Many studies have been conducted to investigate the fabrication process, material issues and properties (e.g., electrical conductivity and strength) of the SLS fabricated bipolar plates. For example, Chen et al. [15,16] studied the effect of SLS process parameters, different infiltration processes and infiltrated materials on the electrical conductivity of the fabricated bipolar plates. Bourell et al. [18] and Guo et al. [19] investigated the properties of the SLS fabricated bipolar plates using carbon fiber, natural graphite, and nano-size carbon black. However, very few studies have reported the in-situ performance of the SLS fabricated bipolar plates,

especially systematic studies with different operation conditions. Such studies are very valuable for fuel cell developers to utilize SLS process for R&D of bipolar plates, since operating parameters have a significant influence on PEM fuel cell performance [20-24].

In this study, graphite composite plates with various flow fields, including parallel in series, interdigitated and bio-inspired designs, were fabricated using the SLS process. The in-situ performance of these plates was studied experimentally under various operating conditions. The effect of temperature, relative humidity, and pressure on fuel cell performance was investigated. The performance characteristics of the fuel cells with different flow field designs were compared. The fuel cell performance over an extended time was also tested to investigate the water management capability of the fabricated plates.

2. Experiments

2.1 Materials

Natural graphite (3610) and synthetic graphite (4437), obtained from Asbury Graphite Mills, Inc. (New Jersey, USA), were used to fabricate graphite composite plates. The particle sizes of natural graphite and synthetic graphite were 75-150 μm and 10-45 μm, respectively. Phenolic powder (GP-5546, Georgia Pacific) with an average size of 15 μm was used as binder in the SLS process. A mixture of liquid epoxy resin (EPON^{TM} Resin

828) and curing agent (EPIKURE^{TM} 3230) was used to infiltrate the porous brown parts after carbonization.

2.2 Fabrication process

Natural graphite, synthetic graphite and binder with a volume percentage of 55%, 10% and 35%, respectively, were ball milled together for 12 hours to achieve a uniform mixture. An SLS machine (Sinterstation 2000) was used to build green parts from this mixture. The SLS process is depicted in Fig. 1. The three-dimensional model of an endplate was converted into slices, and then a laser beam scanned the powder bed according to the cross-section of each slice. The binder was melted by laser to bind the graphite particles. After one layer was scanned, the powder bed was lowered by one layer of thickness, and a new layer of the powder material was fed onto the top of the previous layer. The process was repeated until the plate was finished. The SLS process parameters used were as follows: fill laser power (14 W), outline laser power (4 W), laser scan speed (1.5 m/s), layer thickness (0.1 mm), and laser scan spacing (0.08 mm). The temperatures of the part bed and feed bins were maintained at 60 ^{o}C and 40 ^{o}C, respectively. A carbonization process was then used to heat the green parts in a furnace filled with Argon gas in order to dissociate the binder and convert it into carbon residue to get brown parts. The heating schedule was from room temperature to 200 ^{o}C with a rate of 60 ^{o}C/h, followed by a slower rate of 30 ^{o}C/h to 600 ^{o}C, and then a 50 ^{o}C/h rate to 1000 ^{o}C, maintained for 1 hour. The brown part, which was porous and weak, was infiltrated with a liquid resin to become gas impermeable and to increase its mechanical strength. For

infiltration, brown parts were immersed in the mixture of liquid epoxy resin and a curing agent, taken out after 20 minutes to have their surfaces cleaned, and then placed in an oven at 80 ^{o}C for 30 minutes to cure the infiltrated resin. The final part had an electrical conductivity of ~120 S/cm and a flexural strength of ~40 MPa, which were higher than the target values set by the U.S. Department of Energy [25] and comparable to those fabricated by CM and IM [19].

2.3 Flow field designs

Three flow field configurations, namely, parallel in series [4] (or parallel discontinuous [26]), interdigitated and bio-inspired designs, were used in this study. The parallel in series design (Fig. 2(a)) consisted of a series of four connected Z-type parallel channels. The interdigitated design (Fig. 2(b)) was composed of two sets of dead-end parallel channels, one of which was connected to the inlet and the other to the outlet. This caused a convective flow through the gas diffusion layer (GDL) under the rib, thus enhancing the mass transport of reactant gases [27]. The bio-inspired design was inspired by the vein structures of leaves, which transport mass efficiently from one central source to the whole surface of a leaf, mirroring the function of bipolar plate flow fields [2]. The developed bio-inspired "leaf" design (Fig. 2(c)) consisted of three generations of channels. At the end of all of the channels, reactants were forced to flow through the GDL and merge into the outlet. The active area, channel width and channel depth of all three designs were the same at 50×50 mm^2, 1.5 mm and 1.5 mm, respectively. Land width of the parallel in series and interdigitated designs were 1.0 mm. The contact areas between GDLs and

graphite plates for the parallel in series, interdigitated, and bio-inspired designs were 40%, 40%, and 45% of the active area, respectively. All three plate designs were fabricated using the SLS process. The fabricated plates are shown in Fig. 3.

2.4 Fuel cell testing

A single fuel cell unit was assembled using two fabricated plates, two end plates, and one commercial membrane electrode assembly (MEA), as illustrated in Fig. 4(a). The actual fuel cell unit is shown in Fig. 4(b). Two gold-plated copper plates were used to collect the generated current. The MEA (from FuelCellsEtc) comprised a loading of 4 mg/cm^2 platinum-black (PtB) as the catalyst on both anode and cathode sides, Nafion® 115 as the electrolyte membrane, and carbon cloth as the GDL. Fuel cell performance was measured using a fuel cell test station (Greenlight Innovation, G40) under different temperature, humidity and pressure conditions. The temperature varied from 55 ^oC to 85 ^oC, the relative humidity for both anode and cathode varied from 25% to 100%, and the back pressure varied from 0 to 2 atm. Table 1 provides the details about the experiment sets. A thermocouple mounted inside one of the end plates was used to measure the temperature of the fuel cell. The flow rates of hydrogen and air were controlled by two separate mass flow controllers and set at 300 ml/min and 1050 ml/min, respectively, for all of the experiments. This was corresponded to a stoichiometry of 2.0 at anode and 3.0 at cathode for a current density of 1.0 A/cm^2. The relative humidity was controlled by adjusting the dew point temperature of the inlet flow. Before any test was performed Nitrogen gas was purged into the anode to ensure no oxygen was present. Then, temperature and humidity

were set first at the same time and after reaching the setting point pressure was set (if needed). The dew point temperature was kept lower than the fuel cell temperature during the whole process to prevent water vapor from condensing. It usually took 40-60 minutes to reach the setting temperature and humidity and less than 5 minutes to reach the setting pressure. After the setting operation conditions were reached, it usually took 20-60 minutes for fuel cell to reach the steady output, which was totally 60-120 minutes to reach the steady output from room conditions. During this whole phase, the fuel cell was operated at around 0.7 V. After that, testing was begun by increasing the current density and recording the corresponding voltage after 90 seconds delay ensuring the output was relatively steady. The current density continued increasing until the setting point was reached. After that, the current density was set back to zero, and two more tests were performed following the same procedure. The final result for each condition was obtained by taking the average of the three tests.

3. Results and Discussion

3.1 Effect of temperature

The performance of a PEM fuel cell is characterized by its polarization curve. Figure 5 shows the polarization curves of the three flow field designs at different temperatures, with 100% humidity and ambient pressure. The performance of all the three designs increased when the temperature increased from 55 ℃ to 65 ℃. After 65 ℃, the performance of the fuel cell remained almost the same from 65 ℃ to 75 ℃, and then

decreased from 75 ℃ to 85 ℃. Although the three designs showed a similar trend, the parallel in series design experienced a large increase from 55 ℃ to 65 ℃ and a significant drop from 75 ℃ to 85 ℃, while for the interdigitated and bio-inspired designs, the performance difference among the different temperatures was relatively small. This indicates that the last two designs could broaden the operating temperature range of PEM fuel cells and enable fuel cells work at a relatively lower or higher temperature without sacrificing the output power. According to the fuel cell theory, the output voltage of a fuel cell equals the thermodynamic voltage (theoretical potential) subtracted by the various overvoltage losses [28]:

$$V = E_T - \eta_{act} - \eta_{ohmic} - \eta_{conc} \tag{1}$$

where V is the output voltage of a fuel cell, E_T is the thermodynamic voltage of a fuel cell at temperature T, η_{act} represents the activation losses, η_{ohmic} represents the ohmic losses from ionic and electronic resistance, and η_{conc} represents the concentration losses due to poor mass transport of reactants. The relationship between thermodynamic voltage and temperature is given by

$$E_T = E^0 + \frac{\Delta \hat{s}}{nF}(T - T_0) \tag{2}$$

where E^0 is the thermodynamic voltage under the standard temperature and pressure (25 ℃ and 101.3 KPa), $\Delta \hat{s}$ is the change in entropy for the chemical reaction, n is the number of moles of electrons transferred, and F is the Faraday constant. As Eq. (2) reveals, because $\Delta \hat{s}$ is negative, the thermodynamic voltage E_T decreases as the temperature increases. On the other hand, an increase in temperature reduces activation losses η_{act}. Activation losses are caused by the need to overcome an activation barrier associated

with the electrochemical reaction. Increasing the reaction temperature increases the thermal energy available in the reactant gases and makes the molecules more excited, consequently less energy is sacrificed for the molecules to overcome the activation barrier and thus less activation losses are suffered [29]. When temperature is below 80 ℃, the ionic conductivity of Nafion membrane increases with the increase of temperature [30],

$$\sigma = (0.005193\lambda - 0.00326)\exp\left[1268\left(\frac{1}{303} - \frac{1}{T}\right)\right],\ 298 \leq T \leq 353 \quad (3)$$

where T is the temperature (unit: K) and λ is the water content in Nafion. However, as temperature is above 80 ℃, the Nafion membrane tends to be dehydrated quickly and easily, and thus the ionic conductivity decreases and the ohmic losses increases. This is why the performance of all the three designs decreased from 75 ℃ to 85 ℃. High temperature also enhances the diffusion of reactants and thus reduces the concentration losses. The effect of temperature on the fuel cell performance is a combination of all these influences. Fig. 5 shows the fuel cell performance under different temperatures was very close to each other at low current densities. This is because of the balance between the negative effect on reducing thermodynamic voltage and the positive effect on reducing activation losses. At the intermediate and high current densities, as the temperature increased, initially the positive effects on the reduction of concentration losses and ohmic losses were greater than the negative effects on the reduction of thermodynamic voltage. Thus, the overall performance of the fuel cell increased. However, after the temperature exceeded 65 ℃, these two opposite effects tended to balance each other and the overall fuel cell performance barely changed from 65 ℃ to 75 ℃. Finally, the negative effects surpassed the positive effect, reducing the performance of

the fuel cell as the operating temperature continued increasing. The experimental results of the SLS fabricated plates agreed well with the analytical reasoning and showed that the range of 65 ℃ to 75 ℃ was the optimum operating temperature for all of the three designs. The similar trend was also observed by other researchers using the graphite plates [24].

3.2 Effect of relative humidity

The performance of fuel cells with SLS fabricated graphite composite plates was investigated under different relative humidity, with the temperature kept at 75 ℃ and the back pressure at 0 atm. Both anode and cathode were operated at the same relative humidity. The performance results for the fuel cells with different designs are given in Fig. 6. It can be seen that relative humidity had a significant effect on fuel cell performance. The performance increased greatly as humidity increased from 25% to 75% and the rate of this increase slowed down slightly after reaching 75%. The performance of all the three different flow field designs showed the same trend. Relative humidity mainly affects the ionic conductivity of the polymer electrolyte (Nafion). The proton-conducting capability of Nafion depends on the sulfonic acid ($SO_3^-H^+$) functional group. In the presence of water, the protons (H^+) will detach from the sulfonic acid and form hydronium complexes (H_3O^+), which can transport in the aqueous phase though the membrane if sufficient water exists in the membrane. Therefore, to maintain a high conductivity, Nafion has to be fully hydrated by water. The proton conductivity of Nafion, σ, can be estimated from the water content, λ, in Eq. (3). From Eq. (3) the proton

conductivity of Nafion increases linearly with the increase in its water content. The water content in Nafion is defined as the ratio of the number of water molecules to the number of charged sites ($SO_3^-H^+$), which can be estimated from the relative humidity a_w using the following formula [30]:

$$\lambda = 0.0043 + 17.81a_w - 39.85a_w^2 + 36.0a_w^3, \ 0 < a_w \leq 1 \quad (4)$$

From the above relationship, water content increases with increase in operating humidity; as a result, the fuel cell performance would increase greatly because of the reduction of ohmic losses. The experimental results from the fuel cells using SLS fabricated plates in Fig. 6 agreed with this analytical rationale.

3.3 Effect of back pressure

Figure 7 shows the effect of back pressure on the performance of fuel cells using the SLS fabricated plates. The results show that the fuel cell performance increased greatly as the back pressure increased from 0 atm to 2 atm. Pressure has two positive effects on fuel cell performance, i.e., reducing activation losses and concentration losses. High pressure increases the activity of molecules, and therefore less activation losses are suffered. The increase of back pressure also increases the concentration of reactant gases at both anode and cathode, according to the ideal gas law:

$$c_R^* = \frac{n}{V} = \frac{P}{RT} \quad (5)$$

where c_R^* is the reactant concentration, n is the number of moles of reactant gas, V is the volume of gas, P is the pressure, and R is the ideal gas constant. The high reactant

concentration significantly increases the reaction rate, thus increasing fuel cell output power density. Additionally, the high pressure applied on the flow field forces the reactants to flow into the porous GDL, which also improves the supply efficiency of reactants towards the catalyst layers (reaction sites). Therefore, more reactants take part in the electrochemical reaction and less concentration losses are suffered, resulting in higher performance. The high operating pressure also benefits the removal of water droplets formed within the GDL and channels, keeping the fuel cell from flooding [31]. Figure 7(a) shows that the voltage dropped dramatically after the current density rose above 800 mA/cm^2 for ambient pressure in the parallel in series design, while at pressures of 1 atm and 2 atm, the voltage showed no such remarkable decrease until reaching 1100 mA/cm^2. This indicates less concentration losses were experienced at higher operating pressure. The similar trend was observed for the other two flow field designs. Operating at high pressure might not be a system-efficient solution for large power application due to the requirement of additional power consumption to supply the high-pressure reactant gases flow, while it is still beneficial for small power applications in which no supplemental power is needed for gas flow.

3.4 Comparison of different flow field designs

Figure 8 shows the performance comparison of PEM fuel cells using three different flow field designs at ambient pressure ((a, b)) and 2 atm (c, d). The temperature was 75 ℃, and the relative humidity was 100%. The pressure differences between the inlet and outlet for the parallel in series, interdigitated, and bio-inspired designs were around 100 Pa, 320 Pa

and 480 Pa, respectively. From the results of ambient pressure, the bio-inspired design performed highest among the three flow field designs, with a maximum power density of around 0.5 W/cm^2 (Fig. 8(b)), which was about 20% ~ 25% higher than the other two designs. This is due to the higher mass transport capability of the bio-inspired design. The polarization curves in Fig. 8(a) show that the three designs performed very similarly in the low current density region. However, as the current density increased, concentration losses became significant after 800 mA/cm^2 and 1000 mA/cm^2 for the parallel in series and interdigitated designs, respectively, while no remarkable concentration losses was associated with the bio-inspired design until 1300 mA/cm^2. This result agrees with others' studies which show that the flow field design has little influence on the cell performance at low current density, while significant effect at high operating current density [4,32]. Figures 8 (c) and (d) show that the performance difference of the three designs became smaller when operating at 2 atm. The possible explanation is that with the increased back pressure and thus reactant concentration, almost all of the available reaction sites at the catalyst layer have been utilized for all of the designs, and the limitation of reaction sites becomes the main hindrance to fuel cell performance instead of concentration losses.

3.5 Water management test

The PEM fuel cell with the SLS fabricated plates was operated over an extended time to study the water management capability of these plates. The parallel in series design (Fig. 2(a)) was used in this study and the operating condition was set at 75 ℃, 100% relative

humidity, and ambient pressure. After the operating condition had been reached, a constant current density of 750 mA/cm^2 was drawn out from the fuel cell and the voltage was recorded every 10 seconds for 6 hours by the test station. This current density was very close to the point at which the fuel cell with the parallel in series design produced the maximum power density and the maximum amount of water, as shown in Fig. 8(b). The result is shown in Fig. 9, in which the x axis is the operating time and the y axis is the variation in cell voltage. As the PEM fuel cell warmed up, the voltage slowly increased over the first 120 minutes; after that, the voltage kept relatively steady at 0.535 V for the rest of the testing, with a very small variation, around $\pm$0.005 V. Fig. 9(b) details the performance from the 170th minute to the 179th minute. The voltage decreased suddenly around the 174th minute; 80 seconds later, it returned to the steady-state voltage; then, around the 176th minute, another small drop occurred but quickly recovered. These voltage drops were caused by the accumulation of liquid water within the pores of GDL and the channels, where the water droplets tended to block the pathway of reactant gases [33,34]. When the liquid water was removed out of the fuel cell by the flow of the reactant, which can be observed from the transparent outlet pipe, the voltage returned to the steady state. Then, once again, as the reaction continued, the produced liquid water slowly accumulated inside the fuel cell reducing the voltage, and quickly the voltage increased to the normal value as the water was dragged out of the fuel cell. This result indicates that water does not create a significant blockage within the fuel cell over an extended operation and the SLS fabricated plates could provide a fuel cell with a relatively steady performance by preventing the fuel cell from flooding.

4. Conclusions

Graphite composite plates were fabricated using the Selective Laser Sintering (SLS) process, which has the advantages of reducing the development time and cost and providing a great design flexibility of plates. The fabricated plates were assembled into a fuel cell unit whose performance was tested under different operating conditions, with the temperature varying from 55 ℃ to 85 ℃, relative humidity from 25% to 100%, and back pressure from 0 atm to 2 atm. Fuel cell performance increased with temperature increase from 55 ℃ to 75 ℃, but after that, the performance decreased with temperature increase. Both relative humidity and back pressure had a significant effect on the performance of fuel cells; the higher humidity or back pressure resulted in the higher power density of fuel cell. All the experimental results agreed well with the analytical model based on PEM fuel cell thermodynamics and electrochemistry. The performance of fuel cell using the parallel in series, interdigitated, and bio-inspired designs was compared with each other and the results showed that the bio-inspired design enhanced the fuel cell performance by 20% ~ 25% at ambient pressure. The extended operation result of the PEM fuel cell demonstrated that the SLS fabricated plates could provide a fuel cell with a relatively steady performance. All these results led to the conclusion that SLS process is a great alternative to compression molding or injection molding for the purpose of research and development of bipolar plates due to the cost and time effective development of different flow field designs.

Acknowledgements

This project is funded by the National Science Foundation grant #CMMI-1131659.

References

[1] Tsuchiya, H., and Kobayashi, O., 2004, "Mass Production Cost of PEM Fuel Cell by Learning Curve," Int. J. Hydrogen Energy, 29, pp. 985-990.

[2] Kloess, J. P., Wang, X., Liu, J., Shi, Z., Guessous, L., 2009, "Investigation of Bio-inspired Flow Channel Designs for Bipolar Plates in Proton Exchange Membrane Fuel Cells," J. Power Sources, 188, pp. 132-140.

[3] Ramos-Alvarado, B., Hernandez-Guerrero, A., Elizalde-Blancas, F., Ellis, M. W., 2011, "Constructal Flow Distributor as a Bipolar Plate for Proton Exchange Membrane Fuel Cells," Int. J. Hydrogen Energy, 36, pp. 12965-12976.

[4] Manso, A. P., Marzo, F. F., Barranco, J., Garikano, X., Mujika, M., 2012, "Influence of Geometric Parameters of the Flow Fields on the Performance of a PEM Fuel Cell. A Review," Int. J. Hydrogen Energy, http://dx.doi.org/10.1016/j.ijhydene.2012.07.076

[5] Aiyejina, A., and Sastry, M. K. S., 2012, "PEMFC Flow Channel Geometry Optimization: A Review," J. Fuel Cell Sci. Tech., 9, pp. 011011-1-24.

[6] Muller, A., Kauranen, P., Ganski, A., Hell, B., 2006, "Injection Moulding of Graphite Composite Bipolar Plates," J. Power Sources, 154, pp. 467-471.

[7] Dhakate, S. R., Mathur, R. B., Kakati, B. K., Dhami, T. L., 2007, "Properties of Graphite-Composite Bipolar Plate Prepared by Compression Molding Technique for PEM Fuel Cell," Int. J. Hydrogen Energy, 32, pp. 4537-4543.

[8] Mathur, R. B., Dhakate, S. R., Gupta, D. K., Dhami, T. L., Aggarwal, R. K., 2008, "Effect of Different Carbon Fillers on the Properties of Graphite Composite Bipolar Plate," J. Mater. Process. Technol., 203, pp. 184-192.

[9] Blunk, R., Elhamid, M. H., Lisi, D., Mikhail, Y., 2006, "Polymeric Composite Bipolar Plates for Vehicle Application," J. Power Sources, 156, pp. 151-157.

[10] Du, L., and Jana, S. C., 2007, "Highly Conductive Epoxy/graphite Composites for Bipolar Plates in Proton Exchange Membrane Fuel Cells," J. Power Sources, 172, pp. 734-741.

[11] Lee, J. H., Jang, Y. K., Hong, C. E., Kim, N. H., Li, P., Lee, H. K., 2009, "Effect of Carbon Fillers on Properties of Polymer Composite Bipolar Plates of Fuel Cells," J. Power Sources, 193, pp. 523-529.

[12] Hsiao, M. C., Liao, S. H., Yen, M. Y., Su, A., Wu, I. T., Hsiao, M. H., Lee, S. J., 2010, "Effect of Graphite Sizes and Carbon Nanotubes Content on Flowability of Bulk-molding Compound and Formability of the Composite Bipolar Plate for Fuel Cell. J. Power Sources, 195, pp. 5645-5650.

[13] Yen, C. Y., Liao, S. H., Lin, Y. F., Huang, C. H., Lin, Y. Y., Ma, C. M., 2006, "Preparation and Properties of High Performance Nanocomposite Bipolar Plate for Fuel Cell," J. Power Sources, 162, pp. 309-315.

[14] Guo, N., and Leu, M. C., 2010, "Effect of Different Graphite Materials on Electrical Conductivity and Flexural Strength of Bipolar Plates Fabricated by Selective Laser Sintering," International SFF Symposium, Austin, TX, pp. 482-492.

[15] Chen, S., Bourell, D. L., Wood, K. L., 2004, "Fabrication of PEM Fuel Cell Bipolar Plates by Indirect SLS," International SFF Symposium, Austin, TX, pp. 244-256.

[16] Chen, S., Murphy, J., Herlehy, J., Bourell, D. L., 2006, "Development of SLS Fuel Cell Current Collectors," Rapid Prototyping Journal, 12(5), pp. 275-282.

[17] Wu, M., Leu, M. C., Guo, N., 2012, "Simulation and Testing of Polymer Electrolyte Membrane Fuel Cell Bipolar Plates Fabricated by Selective Laser Sintering," Proc. of ASME International Symposium on Flexible Automation, St. Louis, MO, Paper No. ISFA2012-7249.

[18] Bourell, D. L., Leu, M. C., Chakravarthy, K., Guo, N., Alayavalli, K., 2011, "Graphite-based Indirect Laser Sintered Fuel Cell Bipolar Plates Containing Carbon Fiber Additions," CIRP Ann–Manuf. Techn., 60, pp. 275-278.

[19] Guo, N., and Leu, M. C., 2012, "Effect of Different Graphite Materials on the Electrical Conductivity and Flexural Strength of Bipolar Plates Fabricated Using Selective Laser Sintering," Int. J. Hydrogen Energy, 37, pp. 3558-3566.

[20] Amirinejad, M., Rowshanzamir, S., Eikani, M. H., 2006, "Effects of Operating Parameters on Performance of a Proton Exchange Membrane Fuel Cell," J. Power Sources, 161, pp. 872-875.

[21] Wang, L., Husar, A., Zhou, T., Liu, H., 2003, "A Parametric Study of PEM Fuel Cell Performances," Int. J. Hydrogen Energy, 28, pp. 1263-1272.

[22] Ghosh, P. C., Wüster, T., Dohle, H., Kimiaie, N., Mergel, J., Stolten, D., 2006, "Analysis of Single PEM Fuel Cell Performances Based on Current Density Distribution Measurement," J. Fuel Cell Sci. Tech., 3, pp. 351-357.

[23] Jang, J. H., Chiu, H. C., Yan, W. M., Sun, W. L., 2008, "Effects of Operating Conditions on the Performances of Individual Cell and Stack of PEM Fuel Cell," J. Power Sources, 180, pp. 476-483.

[24] Wang, L., and Liu, H., 2004, "Performance Studies of PEM Fuel Cells with Interdigitated Flow Fields," J. Power Sources, 134, pp. 185-196.

[25] Department of Energy, accessed in August 2012, "Technical Plan – Fuel cells," http://www1.eere.energy.gov/hydrogenandfuelcells/mypp/pdfs/fuel_cells.pdf

[26] Maharudrayya, S., Jayanti, S., Deshpande, A. P., 2006, "Pressure Drop and Flow Distribution in Multiple Parallel-channel Configurations Used in Proton-exchange Membrane Fuel Cell Stacks," J. Power Sources, 157, pp. 358-367.

[27] Nguyen, T. Y., 1996, "A Gas Distributor Design for Proton Exchange Membrane Fuel Cells," J. Electrochem. Soc., 143(5), pp. 103-105.

[28] O'hayre, R. P., Cha, S. W., Colella, W. G., Prinz, F. B., 2009, Fuel Cell Fundamentals (2nd ed.), John Wiley & Sons, Inc., Hoboken, New Jersey, pp. 195-197.

[29] Bard, A. J., and Faulkner, L. R., 2001, Electrochemical Methods: Fundamental and Applications (2nd ed.), John Wiley & Sons, New York, Chap. 3.

[30] Springer, T. E., Zawodzinski, T. A., Gottesfeld, S., 1991, "Polymer Electrolyte Fuel Cell Model," J. Electrochem. Soc., 138(8), pp. 2334-2342.

[31] Li, H., Tang, Y., Wang, Z., Shi, Z., et al., 2008, "A Review of Water Flooding Issues in the Proton Exchange Membrane Fuel Cell," J. Power Sources, 178, pp. 103-117.

[32] Jeon, D. H., Greenway, S., Shimpalee, S., Van Zee, J. W., 2008, "The Effect of Serpentine Flow-field Designs on PEM Fuel Cell Performance," Int. J. Hydrogen Energy, 33, pp. 1052-1066.

[33] Spernjak, D., Prasad, A. K., Advani, S. G., 2007, "Experimental Investigation of Liquid Water Formation and Transport in a Transparent Single-serpentine PEM Fuel Cell," J. Power Sources, 170, pp. 334-344.

[34] Barbir, F., Gorgun, H., Wang, X., 2005, "Relationship between Pressure Drop and Cell Resistance as a Diagnostic Tool for PEM Fuel Cells," J. Power Sources, 141, pp. 96-101.

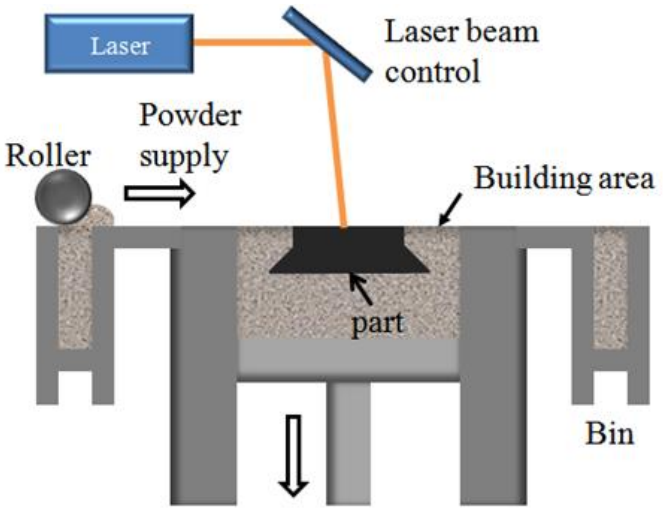

Fig. 1 Fabrication process of Selective Laser Sintering.

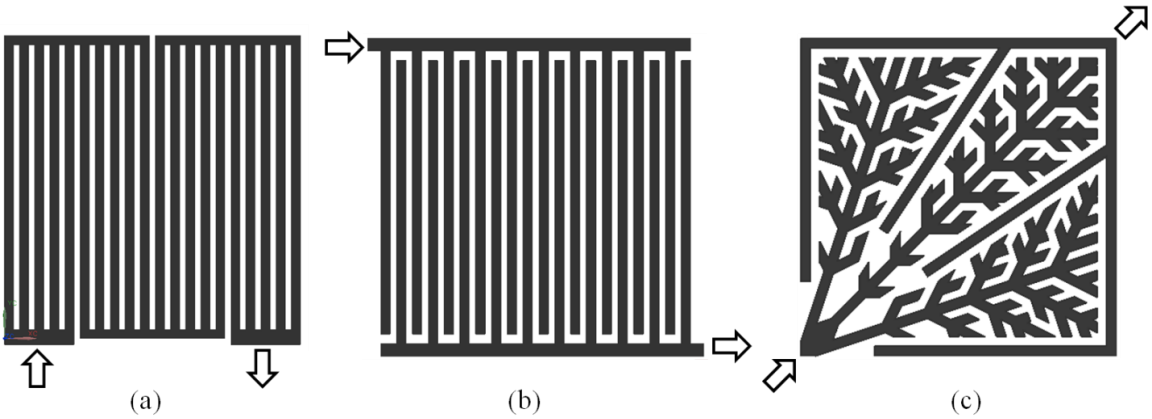

Fig. 2 Different flow field designs: (a) parallel in series design, (b) interdigitated design, (c) bio-inspired design. The dark portion was the flow channels.

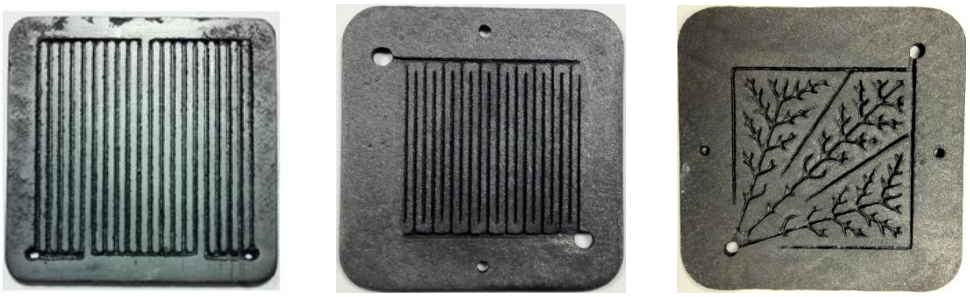

(a) (b) (c)

Fig. 3 Graphite composite plates fabricated using the SLS process: (a) parallel in series design, (b) interdigitated design, (c) bio-inspired design.

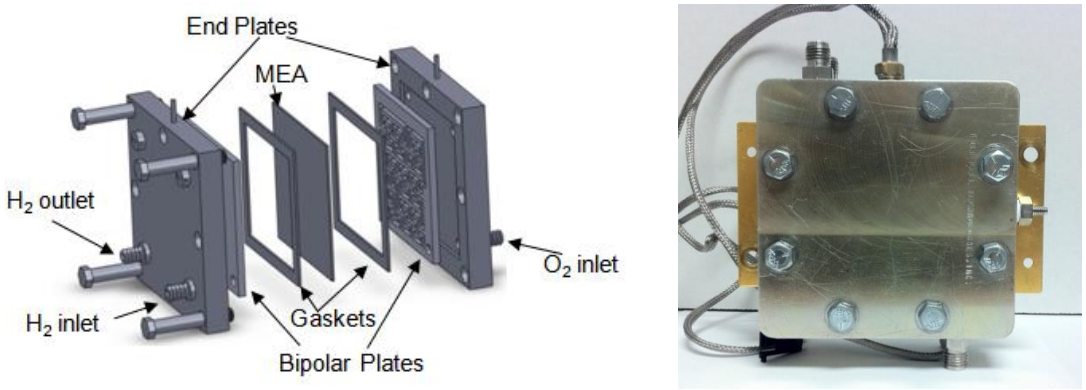

(a) (b)

Fig. 4 (a) Major components in a PEM fuel cell; (b) Actual fuel cell assembly used in the study.

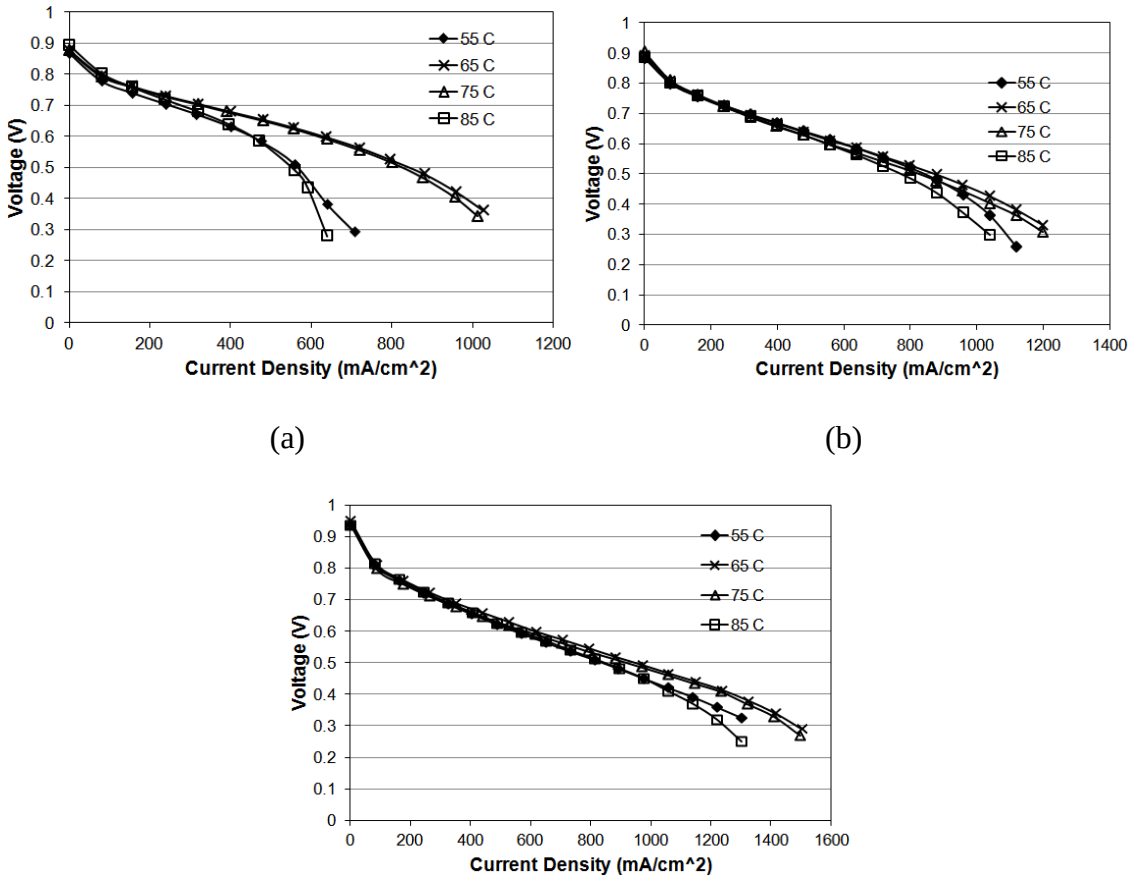

Fig. 5 Effect of temperature on fuel cell performance. The relative humidity was kept at100%, and back pressure at 0 atm. (a) Parallel in series design, (b) interdigitated design and (c) bio-inspired design.

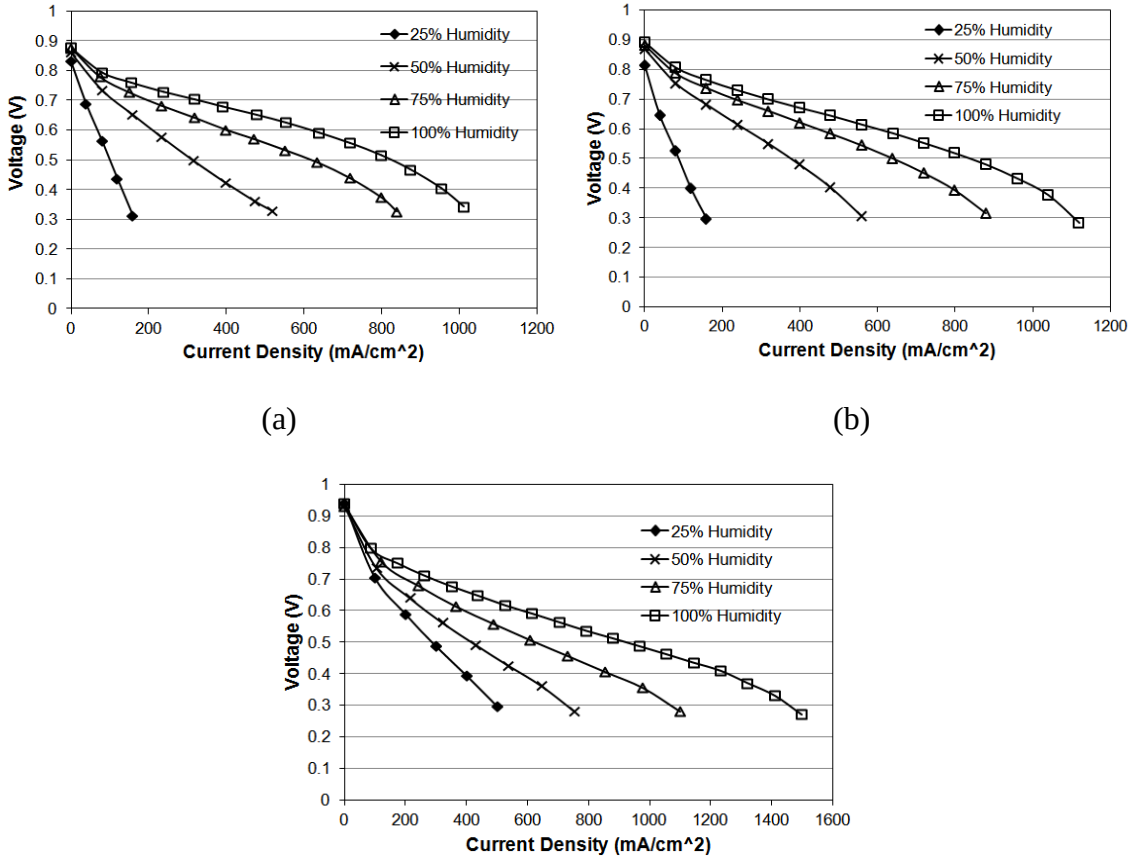

Fig. 6 Effect of relative humidity on fuel cell performance. Temperature was maintained at 75 ℃ and back pressure at 0 atm. (a) Parallel in series design, (b) interdigitated design and (c) bio-inspired design.

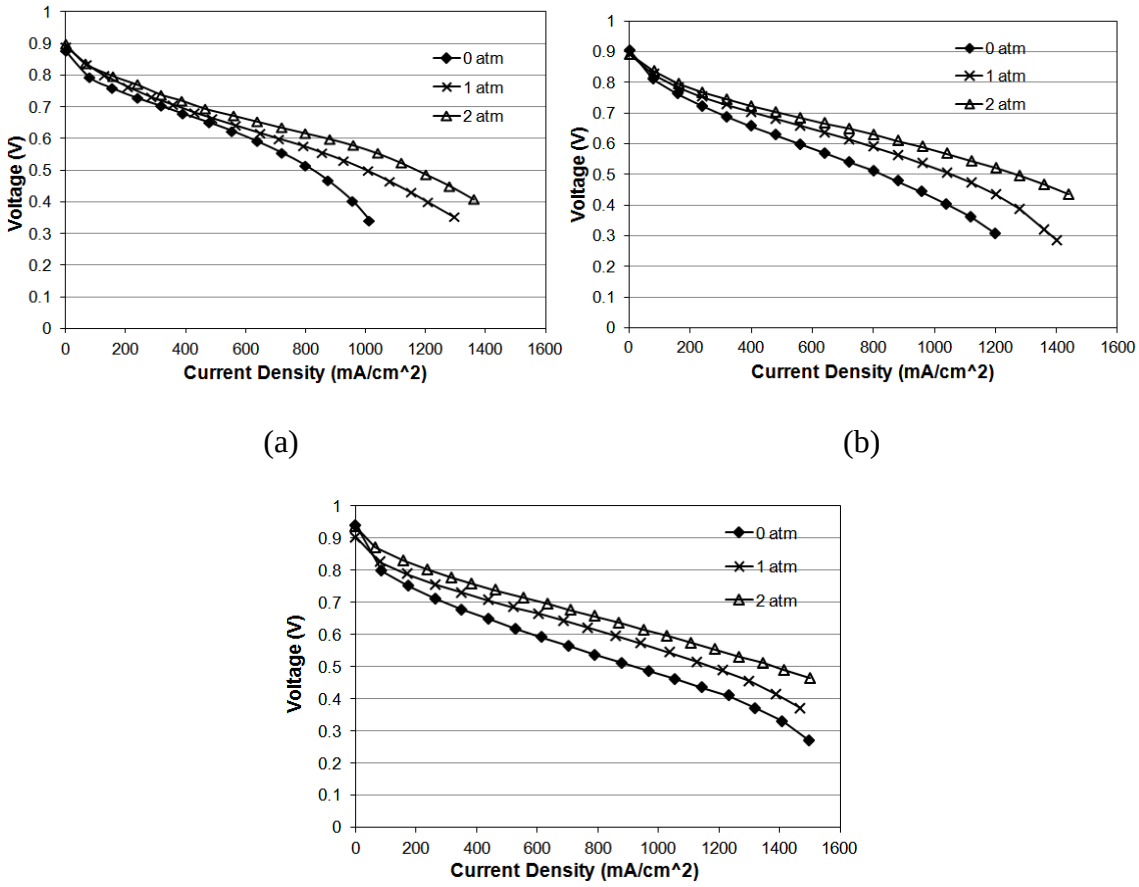

Fig. 7 Effect of back pressure on fuel cell performance. Temperature was maintained at 75 ℃ and relative humidity at 100%. (a) Parallel in series design, (b) interdigitated design and (c) bio-inspired design.

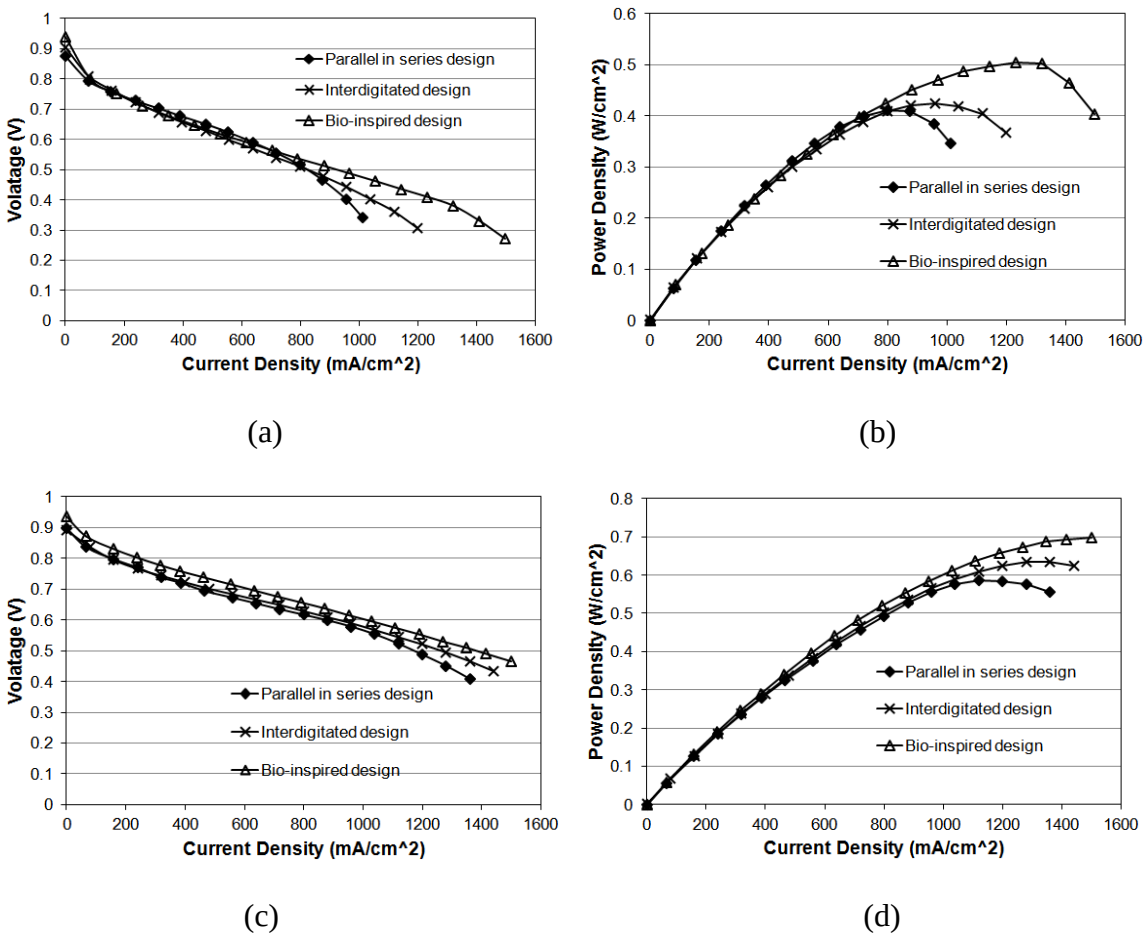

Fig. 8 Comparison of fuel cell performance of parallel in series, interdigitated and bio-inspired designs at (a, b) ambient pressure and (c, d) back pressure of 2 atm. Temperature was 75 ℃ and humidity was 100%.

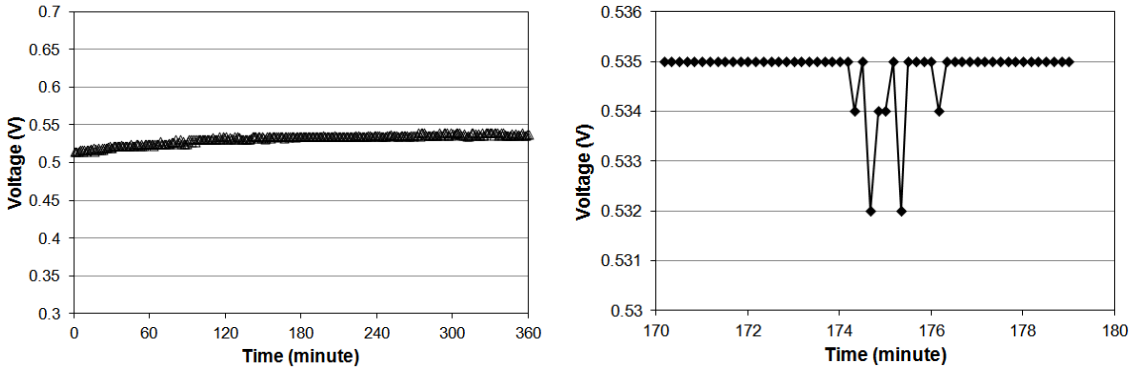

(a) (b)

Fig. 9 (a) Six-hour performance of the PEM fuel cell using the SLS fabricated graphite composite plates with the parallel in series design in Fig. 2(a); (b) detailed performance from the 170th minute to the 179th minute.

Table 1 Operating conditions for fuel cell testing experiments.

	Temperature (℃)	Relative humidity		Back pressure (atm)
		Anode	Cathode	
Temperature study	55	100%	100%	0
	65	100%	100%	0
	75	100%	100%	0
	85	100%	100%	0
Relative humidity study	75	25%	25%	0
	75	50%	50%	0
	75	75%	75%	0
	75	100%	100%	0
Back pressure study	75	100%	100%	0
	75	100%	100%	1
	75	100%	100%	2

PAPER

IV. Bio-inspired Flow Field Designs for Polymer Electrolyte Membrane Fuel Cells

Nannan Guo, Ming C. Leu, Umit O. Koylu

Department of Mechanical and Aerospace Engineering, Missouri University of Science and Technology, Rolla, MO 65409, USA

Abstract

The branching structures found in biological systems have evolved to an optimum arrangement that could distribute nutrients efficiently in the system. Since the flow fields of Polymer Electrolyte Membrane (PEM) fuel cells serve similar functions to the nutrient transport systems in plants and animals, it is expected that flow fields with a similar hierarchical structure could optimize the transport efficiency of reactants and improve the performance of the fuel cell. In this paper, a series of bio-inspired flow field designs inspired by the venation structure of a tree leaf is developed. Two different configurations, interdigitated and non-interdigitated, are considered in implementing the hierarchical structures. Murray's law, which is known as an optimum configuration found in biological circulatory systems, is used to determine the flow channel widths of different generations. The bio-inspired design using Murray's law is compared to a design with constant channel width. Both numerical and experimental studies are carried out to investigate these bio-inspired designs. The mass, velocity, and pressure distributions within the channels and the gas diffusion layers, as well as the fuel cell

performance, are studied for different flow field designs. The results show that the bio-inpsired interdigitated designs substantially improve the fuel cell performance by 20-25% compared to the conventional designs.

Keywords: Bio-inspired designs; Bipolar plates; Murray's law; Fuel cell performance; Numerical simulation.

1. Introduction

The flow field of a bipolar plate is one of the most important features of Polymer Electrolyte Membrane (PEM) fuel cell designs. Studies have demonstrated that the power density of a fuel cell can be increased significantly with a proper flow field design [1,2]. Beside the conventional flow field patterns, researchers have begun to investigate flow field designs with inspirations from the nature [3-8], since the flow fields of PEM fuel cells and the nature's biological structures such as leaf veins (see Fig. 1) and blood vessels have very similar functions, i.e., effectively distributing materials from one central source to other places.

The leaf veins and blood vessels found in biological circulatory systems are usually arranged in hierarchical structures, and a distinctive feature of this arrangement is their multi-stage division or bifurcation. The branching structures have evolved, through natural selection, to an optimum arrangement that minimizes the amount of biological work required to transport nutrients and maintain the system. At each generation, the

characteristic dimension of the vascular segments generally becomes smaller, both in length and diameter. The relationship between the diameter of the parent vessel and the optimum diameters of the daughter vessels was first derived by Murray using the principle of minimum work, known as Murray's law [9]. It states that when a parent blood vessel branches into daughter vessels, the cube of the radius of the vessel is equal to the sum of the cubes of the radii of daughter blood vessels. It has been applied to mathematically determine the channel dimensions of bio-inspired structures in many fields, e.g., microfluidic networks [10,11] and tissue engineering [12]. Due to similar functions, flow fields with configurations similar to the natural structures are expected to improve the performance of fuel cells.

Significant differences between the flow fields in PEM fuel cells and biological structures should be considered in developing bio-inspired flow field designs. Take the venation of a leaf as an example. Firstly, leaf veins are composed of two transport ducts; xylem, which transports water from roots to tissues, and phloem, which transports synthesized chemical products from a leaf towards the rest of the plant. On the other hand, the flow field in a fuel cell comprises only one transport duct, in which both reactants and products are transported in the same direction and in the same duct (especially on the cathode side) while the inlet and the outlet are located in different places. Secondly, all generations of veins are connected to each other except the highest generation, which is open ended, as shown in Fig. 1(b) [13,14]. Because veins are connected to adjacent veins, a number of loops form a network leading to redundancy in the flow path. This is beneficial for plants since the flow can bypass a damaged region using the neighboring

network if a vein is damaged, but this would cause a serious problem in the fuel cell flow field designs because of the formation of stagnant areas. Therefore, it is challenging for bio-inspired flow field designs to address these differences while taking advantage of the structures of leaf veins.

Researchers have come up with various bio-inspired flow field designs using layouts similar to natural structures. These bio-inspired flow fields have been demonstrated to have great potential for distributing reactants effectively and therefore enhancing the fuel cell performance. Chapman et al. [3] reported that their bio-mimetic designs could enhance the performance of PEM fuel cell by about 16%. Tuber et al. [4] investigated a fractal design that used multiple parallel branching channels to transport reactants from inlet to outlet. Their experimental results showed that the fuel cell performance was slightly higher than the conventional parallel design but lower than the conventional serpentine design due to multiple parallel channels and water blockage in these channels. Kloess et al. [5] combined serpentine and interdigitated patterns with a leaf/lung layout in order to create bio-inspired flow layouts that reduced pressure loss and increased power density compared to the traditional serpentine and interdigitated fuel cells. Roshandel et al. [6] developed a leaf-like parallel flow field design that showed more uniform species and velocity distribution along the channels than those in the conventional parallel and serpentine designs. However, very few of these designs implemented the hierarchical structures of biological distribution systems, which could be a major benefit of using bio-inspired flow fields.

This study presents a series of bio-inspired flow field designs by mimicking the hierarchical structures of leaf veins. These designs have multiple (three in the present paper) generations of channels with each generation branching out from its parent branch, similar to the structures that can be found in leaf veins. Two different configurations, interdigitated and non-interdigitated, are investigated in implementing the bio-inspired leaf pattern in the fuel cell flow field. Murray's law is applied to determine the corresponding channel widths of different generations, and the bio-inspired design using Murray's law is compared with the bio-inspired design using constant channel width. Both numerical and experimental studies are carried out to investigate these bio-inspired designs as well as the traditional designs for comparison.

2. Bio-inspired Flow Field Design

2.1 Murray's law

The derivation of Murray's law is based on the minimum energy consumption in a biological structure to distribute mass in the circulatory system and to maintain metabolic processes. This implies that a branching system that obeys Murray's law has the least resistance to flow. Murray assumed that two energy terms contribute to the cost of maintaining blood flow in any section of a vessel: (a) the energy required to overcome viscous drag in a fluid obeying Poiseuille's law, and (b) the energy metabolically required to maintain the volume of blood and vessel tissue involved in the flow. The derivation of Murray's law was described in detail in references [9,12,15] and

summarized here for the completeness of the paper. To simplify the analysis, each segment of the transport pathway is considered to be a circular pipe of radius r and length L. If Q denotes the volumetric flow rate, and Δp represents the pressure drop along the segment, then the power required per unit length, P_V, to overcome the viscous losses, is defined as

$$P_V = \left(\frac{\Delta p}{L}\right) Q \tag{1}$$

The volumetric flow rate for fully-developed laminar flow in a pipe can be found from the Hagen-Poiseuille formula:

$$Q = \frac{\pi r^4 \Delta p}{8\mu L} \tag{2}$$

where μ is the dynamic viscosity, which is a measure of the fluid's resistance to flow. Substituting $\Delta p/L$ from equation (2) into equation (1) allows the viscous power requirement to be expressed as:

$$P_V = \frac{8\mu Q^2}{\pi r^4} \tag{3}$$

Murray assumed that the power associated with the metabolic requirements of a biological system could be directly related to the volume of each segment. The metabolic power per unit length, P_m, required to maintain the blood cells and the walls of a vascular system, can then be written as:

$$P_m = k_m \pi r^2 \tag{4}$$

where k_m is a metabolic constant. Dealing with cardiovascular systems, Murray referred to this power requirement as the "cost of blood volume". Therefore, total power required to operate the system is:

$$P = P_V + P_m = \frac{8\mu Q^2}{\pi r^4} + k_m \pi r^2 \tag{5}$$

For a given flow rate, Q, the optimum vessel dimension that minimizes the power can be found by differentiating equation (5) with respect to the radius and equating the resultant expression to zero,

$$\frac{dP}{dr} = -\frac{32\mu Q^2}{\pi r^5} + 2\pi k_m r = 0 \tag{6}$$

At the optimum conditions, it can readily be shown from equation (6) that the volumetric flow rate is related to the optimum vessel diameter, d_{opt}:

$$Q = \frac{\pi}{32}\sqrt{\frac{k_m}{\mu}}\, d_{opt}^3 = M d_{opt}^3 \tag{7}$$

where $M = \pi/32\sqrt{k_m/\mu}$ is a constant. The optimum relationship between the parent diameter, d_0, and daughter branches (d_{1a}, d_{1b} and d_{1c}) can be derived from equation (7) using the continuity principle at the bifurcation,

$$Q_0 = M d_0^3 = Q_{1a} + Q_{1b} + Q_{1c} = M d_{1a}^3 + M d_{1b}^3 + M d_{1c}^3 \tag{8}$$

which leads to the following relationship:

$$d_0^3 = d_{1a}^3 + d_{1b}^3 + d_{1c}^3 \tag{9}$$

This is known as the Murray's law. For a symmetric bifurcation, where $d_{1a} = d_{1b} = d_{1c}$, it follows that $d_0^3 = 3d_1^3$. Assuming that the branching parameter is held constant at each bifurcation, then the diameter of the nth generation can be written as:

$$d_n = \frac{d_0}{X^{n/3}} \tag{10}$$

where X is the number of branches for nth generation. If the diameter of the nth generation is known, then the diameter of mth ($m < n$) generation can be calculated from:

$$d_m = d_n(X)^{(n-m)/3} \tag{11}$$

For bipolar plate flow field of a fuel cell, hydraulic diameter should be used because of the rectangular geometry of the channels, i.e.:

$$d_m^H = d_n^H (X)^{(n-m)/3} \tag{12}$$

where, the hydraulic diameter for a rectangular channel is defined as:

$$d^H = \frac{4A_c}{P} = \frac{2WD}{W+D} \tag{13}$$

Here, A_c is the channel's cross-sectional area, P is the perimeter, W is the channel width, and D is the channel depth. As long as the hydraulic diameter is the same, the flow resistance in the channels is also the same irrespective of the variation of width and depth.

2.2 Flow field designs

A bio-inspired leaf flow field pattern in Fig. 2 was designed by mimicking the hierarchical structures of leaf veins. The whole flow field was divided into three sub-areas, and each sub-area had one hierarchical structure (branch) to supply reactants. The left branch and the right branch were taken to be identical. To reduce design complexity, the hierarchical structures were restricted to three generations, i.e., primary, secondary and tertiary generations. The angles between different channels were 45°. Figure 2(a) shows the bio-inspired leaf design with interdigitated configuration and constant channel width of 1.5 mm. The inlet branches were not directly connected to the outlet channels. The flow was forced to go through the gas diffusion layer (GDL) from the end of each channel to the outlet channels. As a comparison, a variation of the bio-inspired leaf design using a non-interdigitated configuration was also developed as shown in Fig. 2(b),

in which the second generation channels were connected to the outlet channels but the other inlet channels were not connected to either the outlet channels or the other adjacent channels. The reason for disconnecting these channels was to minimize the flow loops in the flow field, thus alleviating the stagnant flow problem. Both of these two designs had the same channel width, 1.5 mm, for all the branches. Another bio-inspired leaf design with interdigitated configuration was developed using the Murray's law to determine the channel width of different generations. The tertiary channel width was chosen as 1.0 mm, other generations' widths were determined using Equations (12) and (13). The dimensions of the different generations of channels are given in Table 1, and the associated CAD model is shown in Fig. 2(c). The width difference between the middle branches and the leaf & right branches is due to the different numbers of the secondary and tertiary channels. In addition to these bio-inspired designs, two conventional designs, interdigitated and parallel-in-series, as shown in Fig. 3, were also investigated for purpose of comparison. Both of these two conventional designs had channel width of 1.5 mm and land width of 1.0 mm. All of the flow field designs had the same channel depth of 1.5 mm and the active area of 5×5 cm^2.

3. Fuel cell simulation model

The governing equations involved in the PEM fuel cell transport phenomena are summarized in the following [16-22]. The three-dimensional fluid flow and heat transfer were modeled using the Navier-Stokes transport equation

$$\frac{\partial}{\partial t}\int_V \rho\phi \, dV + \oint_A \rho\phi V \cdot dA = \oint_A \Gamma_\phi \nabla\phi \cdot dA + \int_V S_\phi \, dV \qquad (14)$$

where ρ is the density, ϕ is the transported quantity, t is the time, A is the area, V is the volume, Γ_ϕ is the transported quantity diffusivity, and S_ϕ is the source term. The first term in the equation corresponds to the transient transport of ϕ, the second term to the transport of ϕ by convection, the third term to the transport of ϕ by diffusion, and the fourth term to the source of ϕ. The different transport equations were assembled by using the appropriate variables to model the balances of continuity, momentum, energy and species [16]. Additionally, two potential equations were solved for the solid phase and the membrane phase, respectively,

$$\nabla \cdot \left(\sigma_j \nabla \varphi_j\right) + R_j = 0 \tag{15}$$

where σ is the electric conductivity, φ the electrical potential and R_j the volumetric transfer current.

Water liquid saturation equation was solved for modeling the two-phase flow. The saturation model approach was used for the liquid water formation and transport. The conservation equation for water saturation, s, is:

$$\frac{\partial(\epsilon \rho_l s)}{\partial t} + \nabla \cdot \left(\rho_l \vec{V}_l s\right) = r_w \tag{16}$$

where the subscript l stands for liquid water, $\vec{V}_l$ is the velocity vector, and r_w is the condensation rate. Inside the porous zones, the capillary force becomes the main driving force for liquid water transport, and therefore the convective term in the above equation was replaced by capillary diffusion term:

$$\frac{\partial(\epsilon \rho_l s)}{\partial t} + \nabla \cdot \left(\rho_l \frac{k s^3}{\mu_l} \frac{dp_c}{ds} \nabla s\right) = r_w \tag{17}$$

where k is the permeability, μ is dynamic viscosity, and p_c is the capillary pressure. The blocking of the porous media and the flooding of the reaction surface were modeled by multiplying the porosity and the active surface area by a factor (1-s). Species diffusivities were also corrected with s to account for the pore blockage. Therefore, the complete set of transport equations, that is, mass continuity, momentum in (x, y, z) directions, energy, chemical species (H_2, O_2, H_2O), solid phase potential, membrane phase potential, and liquid saturation, were solved in the present computational analysis.

The fluid flow pressure drop in gas diffusion and catalyst layers is mainly governed by flow in porous media, represented by adding a negative source in the momentum equations:

$$S_i = -(\frac{\mu}{k} v_i + C_2 \frac{1}{2} \rho v_{mag} v_i) \tag{18}$$

where S_i is the source term in i direction, C_2 the inertial resistance factor, v_i the velocity in i direction, and v_{mag} the velocity magnitude. For the velocity ranges typically found in fuel cell GDL and catalyst layer, only the viscous loss is significant, and therefore the pressure drop in the GDL is proportional to the local fluid velocity. The Stefan-Maxwell equation governs the multi-species diffusion in the GDL although the model presented in this work calculated species diffusivities according to:

$$D_i = \epsilon^{1.5}(1-s)^{r_s} D_i^{ref} \left(\frac{p_{ref}}{p}\right) (\frac{T_{ref}}{T})^{1.5} \tag{19}$$

where r_s is the pore blockage exponent and ϵ is the porosity. Volumetric sources were added to the energy equation, accounting for the reaction heat generation at the cathode catalyst layer, the Joule effect, and the latent heat in case phase change occurs.

The electrochemistry was modeled by computing the reactants' oxidation and reduction rates taking place at the catalyst surfaces. The source terms in the equations, or transfer currents, were calculated according to the general Butler-Volmer equations:

$$R_{an} = i_{ref}^{an}\left(\frac{[H_2]}{[H_2]_{ref}}\right)^{\gamma an}\left(e^{\frac{\alpha_{an}F\eta_{an}}{RT}} - e^{\frac{-\alpha_{cat}F\eta_{an}}{RT}}\right) \quad (20a)$$

$$R_{cat} = i_{ref}^{cat}\left(\frac{[O_2]}{[O_2]_{ref}}\right)^{\gamma cat}\left(e^{\frac{\alpha_{an}F\eta_{cat}}{RT}} + e^{\frac{-\alpha_{cat}F\eta_{cat}}{RT}}\right) \quad (20b)$$

A PEM fuel cell module from the commercial software ANSYS Fluent was employed to solve the governing equations [24,25]. A three-dimensional model based on the finite element method (FEM) was used to investigate the mass, velocity, and pressure distributions within different flow field designs and also the performances of the PEM fuel cells considered here. Model parameters and operation conditions were given in Tables 2 and 3, respectively.

4. Experiments

Graphite composite bipolar plates with the bio-inspired flow field designs in Fig. 2 and the conventional designs in Fig. 3 were fabricated using the Selective Laser Sintering (SLS) process. As one of the additive manufacturing processes, selective laser sintering fabricates parts layer by layer by directing a laser beam to selectively fuse material particles according to the geometry of each cross-section of a three-dimensional CAD model. This process is capable of building parts with complex geometries. The detailed fabrication process and parameters were given in [26,27]. Examples of the fabricated

parts are shown in Fig. 4. After the plates with flow channels were made, a single fuel cell unit was assembled using two fabricated plates and one commercial membrane electrode assembly (MEA). The MEA (FuelCellsEtc) contained a loading of 4 mg/cm^2 platinum-black (PtB) as the catalyst on both the anode and cathode sides, Nafion® 115 as the membrane, and a carbon cloth as the gas diffusion layer. Fuel cell performance was measured using a test station (Greenlight Innovation, G40), and the operation conditions are given in Table 3. Steady states were usually reached about 120 minutes after the pre-set conditions. Current density was increased by 40 mA/cm^2 each time, and the corresponding voltage was recorded after the steady state was reached. The current density was increased until the cell voltage dropped to 0.3 V. After that, current density was set to zero, and two more tests were performed. The final result for each condition was reported by taking the average of three measurements. The power density was obtained by multiplying current density and corresponding voltage.

5. Results and Discussion

5.1 Experimental results

Figure 5 shows the experimental results of the PEM fuel cells using four different flow field designs at the ambient pressure, temperature of 75 ℃, and relative humidity of 100%. The bio-inspired design using Murray's law performed highest among all of the flow fields considered, with a maximum power density slightly above 0.5 W/cm^2 (Fig. 5(b)), which was about 20-25% higher than the two conventional designs. This is due to

the higher mass transport capability of the bio-inspired design. The bio-inspired design using constant channel width performed slightly lower than the bio-inspired design using Murray's law, indicating that the use of Murray's law can improve the mass transport efficiency of the flow field, which will be discussed in detail later. The polarization curves in Fig. 5(a) show that the four designs performed very similarly in the low current density region. However, as the current density increased, concentration losses became significant after 800 mA/cm^2 and 1000 mA/cm^2 for the parallel-in-series and interdigitated designs, respectively, while no remarkable concentration losses were associated with the bio-inspired design until 1300 mA/cm^2. This observation agrees with other studies that showed that the flow field design had little influence on the cell performance at low current densities in contrast to its significant effect at high operating current densities [28]. This is expected as the concentration losses become more dominant at higher currents.

5.2 Validation of fuel cell simulation model

The experimental results of PEM fuel cell using different flow field designs were used to validate the simulations. Both the experiments and computations were conducted using the same operational parameters, which were given in Table 3. Figure 6 shows the comparison of the numerical and experimental results. The simulation model predicted the experimental results well with the difference within 10% for all the investigated designs, indicating that the computations were able to accurately model PEM fuel cells. After this validation, the fuel cell simulation model was used to study the mass, velocity

and pressure distributions of PEM fuel cells for the bio-inspired designs and the conventional designs.

5.3 Non-interdigitated and interdigitated configurations

The bio-inspired flow field designs with interdigitated (Fig. 2(a)) and non-interdigitated (Fig. 2(b)) configurations were compared. Figures 7 and 8 show the oxygen distribution, flow velocity, and pressure distribution obtained from the numerical simulations for these two different configurations. The channel width was set constant (i.e., without using Murray's law). From Figs. 7(a,b) and 8(a,b), the oxygen distribution in the GDLs and in the channels was both much more uniform for the interdigitated design than for the non-interdigitated design. Also, much higher oxygen concentration in the GDL was achieved for the interdigitated design.

In the non-interdigitated bio-inspired design, lower oxygen concentration existed near the ends of the primary and tertiary channels because only the secondary channels were connected to the outlet channels and the primary and tertiary channels had dead ends. Lower oxygen concentrations were also found in the branches far away from the central primary branches, as shown in Fig. 7(b). This is because gas prefers to flow along the shortest path, thus more oxygen flows along the channels near the central branch and less oxygen flows along the channels in the left and right branches. Additionally, by comparing the channels in the three generations, it can be seen that the primary and secondary channels had relatively high oxygen concentrations, as shown in Fig. 7(b).

Consequently the GDL areas under the primary and secondary channels received high oxygen supply but some of other areas were not be able to get sufficient oxygen supply, as shown in Fig. 7(a).

In comparison, since all the channels in the bio-inspired interdigitated design had dead ends, the flow resistance for each flow path mainly depended on the resistance across land area while the length difference between flow paths had negligible influence on flow resistance compared to the crossing land area. Consequently, oxygen distribution was more uniform in all the channels for the interdigitated design, except a few places around the end of the tertiary channel where slightly lower oxygen concentration was found, as indicated in Fig. 8(b). This is because these tertiary channels were adjacent to other inlet channels instead of outlet channels, therefore the driving force of the convective under-rib flow was much smaller, as can be seen from the velocity distribution in Fig. 8(c). Figure 8(a) shows that almost the entire GDL was fed with high concentration oxygen (greater than 15%). This is because the flow was forced to go through the GDL in the interdigitated bio-inspired design, hence higher transport capability towards the GDL and catalyst layers was achieved. The low concentration around the areas near the inlet is due to no channels (branches) in these areas, and the low concentration at the ends of several tertiary channels is due to the weak convective flow as discussed above. As a result, the performance of the interdigitated bio-inspired design was much higher than that of the non-interdigitated design, as can be seen in Fig. 9.

Figure 8(c) shows that the interdigitated design had a very high under-rib flow along the outlet collecting channels. A detailed comparison of the under-rib velocity distributions between the non-interdigitated and interdigitated designs is given in Fig. 10. It clearly shows that a strong under-rib flow existed in the interdigitated design but there was no under-rib flow in the non-interdigitated design. From the results of flow velocity distribution within channels in Fig. 7(d), the velocity was higher in the middle branch channels but lower in the two side branch channels for the non-interdigitated design because the flow resistance through the middle channels was lower due to shorter flow paths. However, the flow velocity distributions in the middle and side branches were almost the same for the interdigitated design (Fig. 8(d)) because the flow resistance through the three different branches was mainly determined by the flow resistance through the GDL and hence was almost the same. Pressure drop from inlet to outlet in the interdigitated bio-inspired design (Fig. 8(f)) was much larger than that in the non-interdigitated design (Fig. 7(f)), as expected, because of the larger flow resistance across the GDL in the interdigitated design.

5.4 Effect of channel width

It is well known that the channel dimensions of flow fields have significant effect on fuel cell performance, even for the same layout. To fully take advantage of bio-inspired designs, not only the hierarchical structures but also the channel dimensions of different generations should be taken into account. As mentioned in Section 2.1, the biological transport systems were generally found to obey Murray's law, which has been

mathematically proven to achieve the minimal energy consumption in transporting materials. A bio-inspired flow field design was developed using Murray's law, as shown in Fig. 2(c), and compared to the bio-inspired design using a constant channel width to investigate the effect of Murray's law on flow field designs.

Figure 11(b) and (d) shows that the oxygen distribution and flow velocity distribution in the design following Murray's law were very similar to that of the design with constant channel with (Fig. 8(b) and (d)). However, the tertiary channels in the design following Murray's law have slightly higher oxygen concentration. This is because the mass flow rate gradually decreased from parent channels to child channels with the consumption of reactants while the channel width also decreased according to Murray's law. Therefore, the oxygen concentration and flow velocity within the channels of different generations kept almost constant, benefiting the mass transport of reactants. In terms of the oxygen distribution in GDLs, since both of the designs (one following Murray's law and the other with constant channel width) used the interdigitated configuration, the dominating mechanism for the transport of reactants from the flow channels to the GDL was convective flow, which was driven by pressure differences between adjacent channels, especially in the area near the outlet channels. The oxygen distributions in the GDLs (Figs. 8(a) and 11(a)) were nearly the same due to the similar pressure distributions in these two designs. The channel width variation had much less effect on pressure distribution, as shown in Figs. 8(f) and 11(f). This is because the flow resistance caused by different channel widths was much smaller than that due to the cross-flow through the GDL. On the other hand, in the areas far away from the outlet channels, the transport

mechanism of reactants from the flow channels to the GDL was mainly diffusion driven by concentration gradients instead of convection due to small pressure differences between adjacent channels. Since the design according to Murray's law had slightly better reactant distribution in the channels, the diffusion to the GDL was more uniform (smaller blue areas) and thus the mass distribution on the GDL was slightly better in these areas than the design with constant channel width. Consequently, the fuel cell performance of the design following Murray's law was slightly better than the design with constant channel width, as shown in Fig. 5.

5.5 Comparison of bio-inspired and conventional designs

Two conventional designs, interdigitated and parallel-in-series, as shown in Fig. 3, were used to compare with the bio-inspired design. In order to have a fair comparison of flow patterns, the same constant channel width was used for all the three designs. Experimentally measured results on fuel cell performance were compared earlier in Fig. 5. The oxygen distributions within the GDLs obtained from the computational simulations are shown in Fig. 12. Figure 12(a) shows that the parallel-in-series design had several big stagnant areas along the parallel channels that were the main drawback of this design. The oxygen concentrations in these areas were very low and thus the overall fuel cell performance of the parallel-in-series design was the lowest among all the designs investigated, as can be seen from Fig. 5. The conventional interdigitated design considered here, as expected, had a higher performance than the parallel-in-series design due to the higher oxygen concentration in the GDL, as shown in Fig. 12(b). The pressure

difference between the adjacent inlet and outlet channels forced the convective flow under the ribs between them, which increased the mass transport efficiency. However, oxygen concentrations in the channels and under the ribs were distinctly different while the concentrations in the channels were higher than those under the ribs. In comparison, the oxygen concentration distribution in the GDL was much more uniform irrespective of under channels or ribs in the bio-inspired interdigitated design with constant channel width in Fig. 12(c). Smaller differences on oxygen concentration were found between the areas under channels and ribs in the bio-inspired design although several small stagnant areas existed, as discussed in Section 5.3. As a result, the bio-inspired design had higher performance than the conventional designs, as shown in Fig. 5.

6. Summary and Conclusions

Bio-inspired flow field designs with hierarchical structures similar to leaf veins were developed and fabricated using the selective laser sintering process. Both numerical and experimental studies were carried out to investigate the bio-inspired flow field designs. To implement the hierarchical structure in the flow field while minimizing the loop number, two configurations, non-interdigitated and interdigitated, between the inlet branches and outlet collecting channels were investigated and compared. The simulation results showed that the bio-inspired design with interdigitated configuration had more uniform and higher oxygen distribution in the GDL and hence higher fuel cell performance, but its pressure drop was higher than that of the non-interdigitated design as expected. A bio-inspired design with interdigitated configuration was improved by

applying Murray's law to determine the channel dimensions of different generations in order to further take advantage of the optimum transport structures in biological systems. The results demonstrated that, after applying Murray's law, the oxygen distribution as well as the fuel cell performance improved slightly. The bio-inspired designs were compared to two conventional flow field designs: parallel-in-series and interdigitated. The experimental results showed that the peak power density of the fuel cell using the interdigitated bio-inspired design was 20-25% higher than that of the two conventional designs, demonstrating the significant advantages of the bio-inspired design developed in this study.

Acknowledgements

This project is funded by the National Science Foundation, Grant No. CMMI-1131659.

References

[1] A.P. Manso, F.F. Marzo, J. Barranco, X. Garikano, M. Mujika, Int. J. Hydrogen Energy 37 (2012) 15256-15287.

[2] X. Li, I. Sabir, Int. J. Hydrogen Energy 30 (2005) 359-371.

[3] A. Chapman, I. Mellor, The Eighth Grove Fuel Cell Symposium, London, 2003.

[4] K. Tuber, A. Oedegaard, M. Hermann, C. Hebling, J. Power Sources 131 (2004) 175-181.

[5] J.P. Kloess, X. Wang, J. Liu, Z. Shi, L. Guessous, J. Power Sources 188 (2009) 132-140.

[6] R. Roshandel, F. Arbabi, G. Karimi Moghaddam, Renew. Energ. 41 (2012) 86-95.

[7] A. Arvay, J. French, J.-C. Wang, X.-H. Peng, A.M. Kannan, Int. J. Hydrogen Energy 38 (2013) 3717-3726.

[8] N. Guo, M.C. Leu, M. Wu, Proceedings of International SFF Symposium, Austion, TX, 2011, 607-623.

[9] T.F. Sherman, J. Gen. Physiol. 78 (1981) 431-453.

[10] R.W. Barber, D.R. Emerson, Microfluid. Nanofluidics 4 (2008) 179-191.

[11] D.R. Emerson, K. Cieslicki, X.J. Gu, R.W. Barber, Lab Chip 6 (2006) 447-454.

[12] R.W. Barber, D.R. Emerson, Altern. Lab. Anim. 38 (2010) 67-79.

[13] S. Bohn, B. Andreotti, S. Douady, J. Munzinger, Y. Couder, Phys. Rev. E 65 (2002) 061914.

[14] M. Durand, D. Weaire. Phys. Rev. E 70 (2004) 046125.

[15] P.R. Painter, P. Eden, H.-U. Bengtsson, Theor. Biol. Med. Model. 3 (2006) 31-40.

[16] A. Iranzo, M. Munoz, F. Rosa, J. Pino, Int. J. Hydrogen Energy 35 (2010) 11533-11550.

[17] R.P. O'Hayre, S.W. Cha, W.G. Colella, F.B. Prinz, Fuel cell fundamentals, second ed., John Wiley & Sons, Hoboken, New Jersey, 2009, 169-179.

[18] Y.M. Ferng, A. Su, Int. J. Hydrogen Energy 32 (2007) 4466-4476.

[19] A.D. Le, B. Zhou, J. Power Sources 182 (2008) 197-222.

[20] E. Hontanon, M.J. Escudero, C. Bautista, P.L. Garcia-Ybarra, L. Daza, J. Power Sources 86 (2000) 363-368.

[21] F. Barreras, A. Lozano, L. Valino, C. Marin, A. Pascau, J. Power Sources 144 (2005) 54-66.

[22] N. Guo, M.C. Leu, U.O. Koylu, Int. J. Hydrogen Energy 38 (2013) 6750-6761.

[23] D. Cheddie, N. Munroe, J. Power Sources 147 (2005) 72-84.

[24] A.P. Manso, F.F. Marzo, M. Garmendia Mujika, J. Barranco, A. Lorenzo, Int. J. Hydrogen Energy 36 (2011) 6795-6808.

[25] A. Iranzo, M. Munoz, J. Pino, F. Rosa, Int. J. Hydrogen Energy 36 (2011) 9123-9127.

[26] N. Guo, M.C. Leu, Int. J. Hydrogen Energy 37 (2012) 3558-3566.

[27] N. Guo, M.C. Leu, Proceedings of International SFF Symposium, Austion, TX, 2012, 212-225.

[28] D.H. Jeon, S. Greenway, S. Shimpalee, J.W. Van Zee, Int. J. Hydrogen Energy 33 (2008) 1052-1066.

(a) 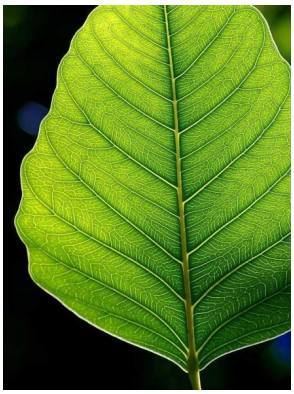 (b) 

Fig. 1 Examples of flow patterns in nature: (a) leaf veins and (b) details of the venation network structure of a leaf [13].

(a) (b) (c)

Fig. 2 Bio-inspired leaf flow field designs with three generations of channels: primary, secondary and tertiary generations. (a) Interdigitated flow field design with constant channel width of 1.5 mm; (b) Non-interdigitated bio-inspired design with constant channel width of 1.5 mm; (c) Interdigitated design with varying channel width determined by Murray's law in Table 1. (The dark color portion is the flow channels)

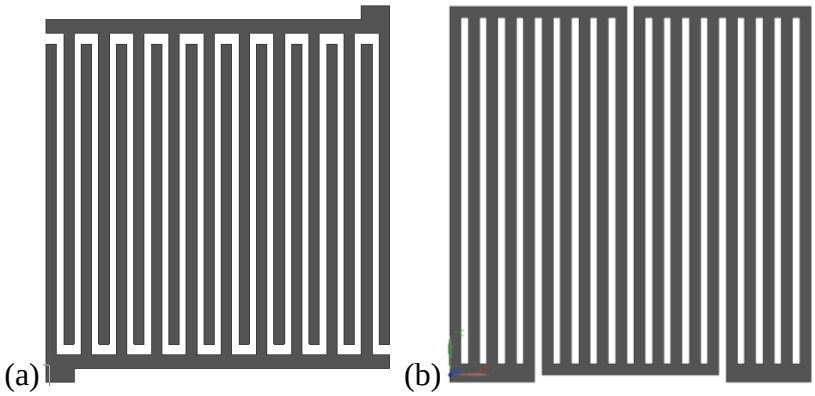

(a) (b)

Fig. 3 (a) Conventional interdigitated design and (b) parallel in series design that are used to compare with the bio-inspired designs. The channel width is 1.5 mm and land width is 1.0 mm.

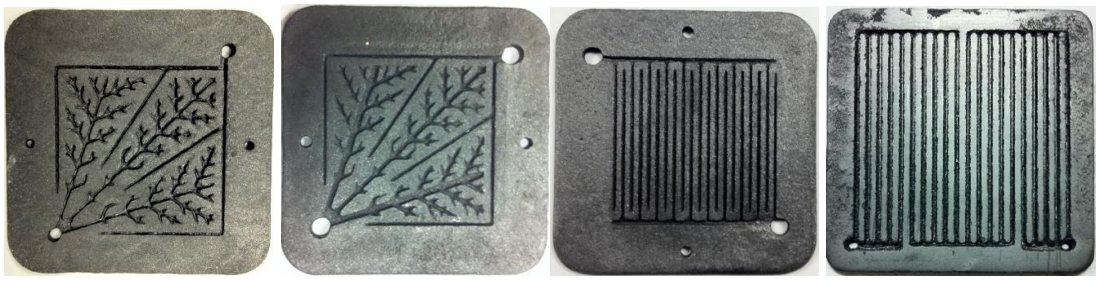

(a) (b) (c) (d)

Fig. 4 Example of the SLS fabricated graphite composite plates, (a) interdigitated bio-inspired design with constant channel width, (b) interdigitated bio-inspired design using Murray's law, (c) conventional interdigitated design, and (d) parallel in series design.

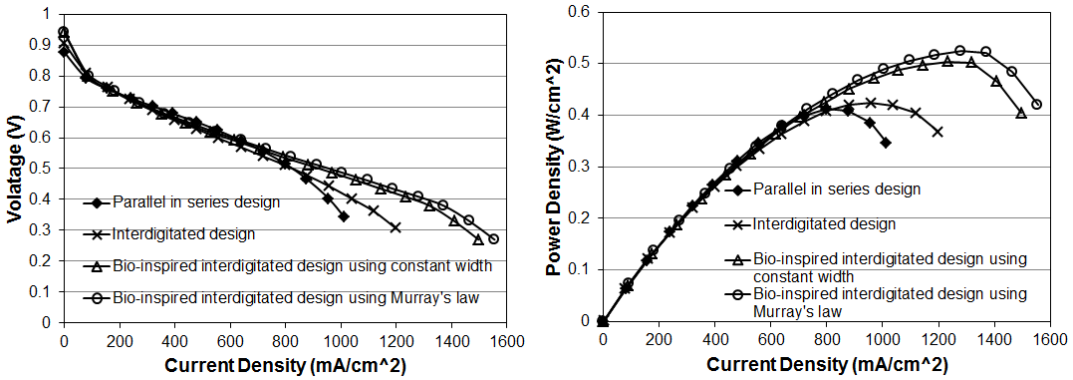

Fig. 5 Comparison of experimental results of the bio-inspired interdigitated leaf designs and conventional designs.

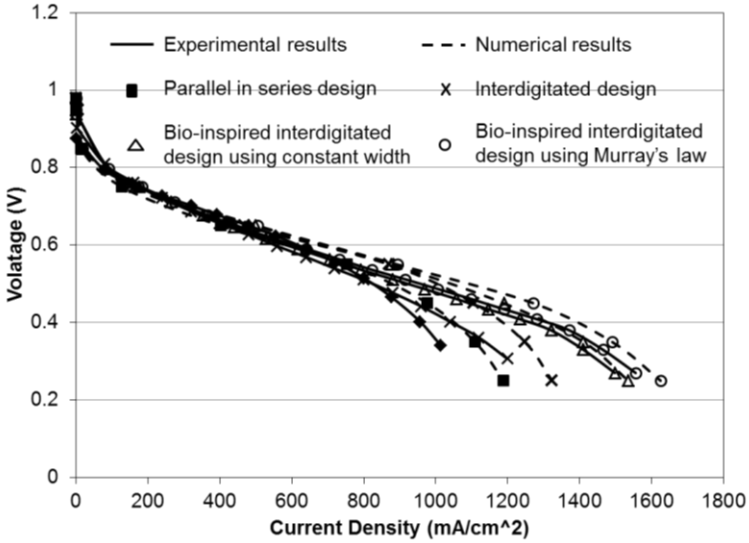

Fig. 6 Comparison of numerical and experimental results of PEM fuel cell using different flow field designs.

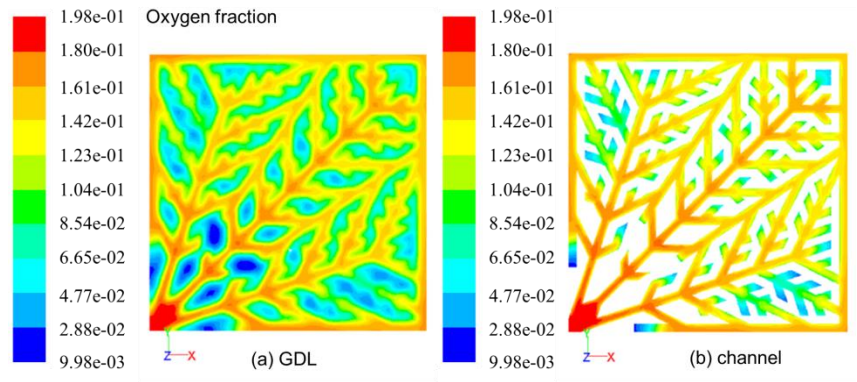

Oxygen distribution

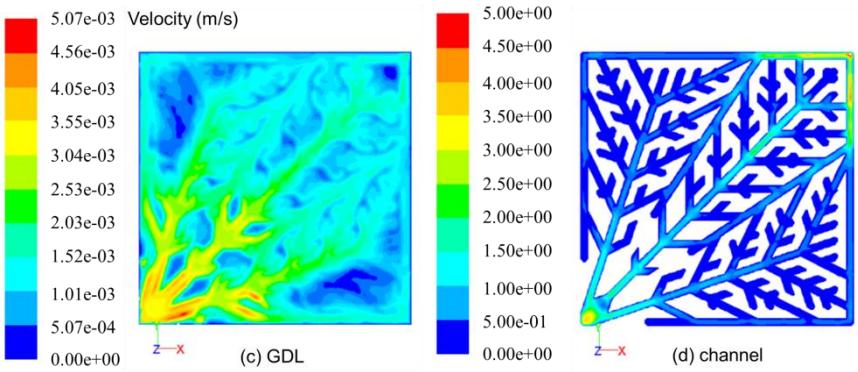

Velocity distribution

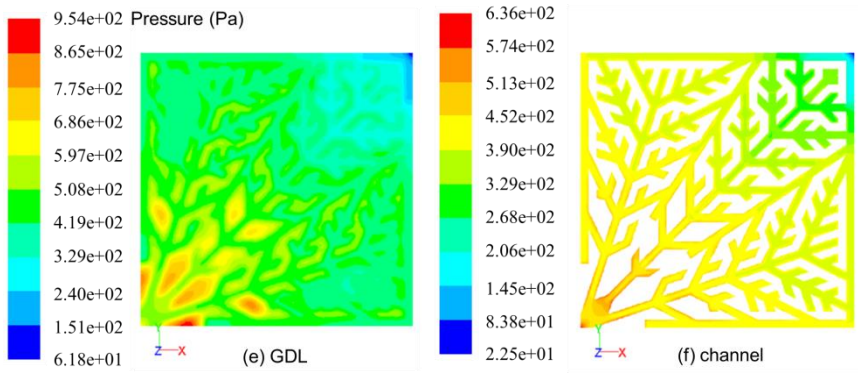

Pressure distribution

Fig. 7 Numerical results of the non-interdigitated bio-inspired design with constant channel width.

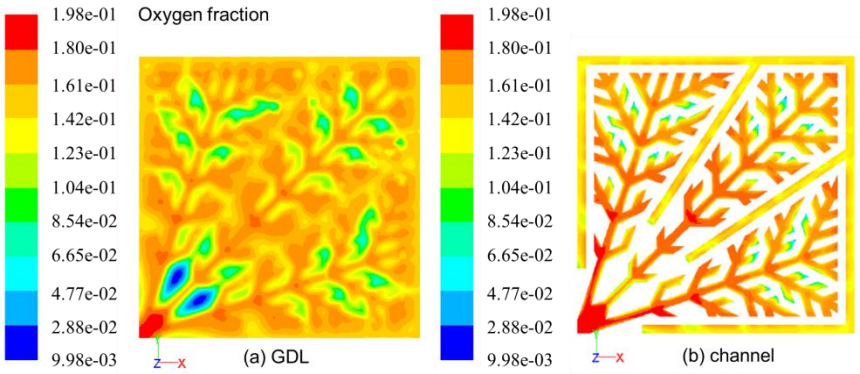

Oxygen fraction distribution

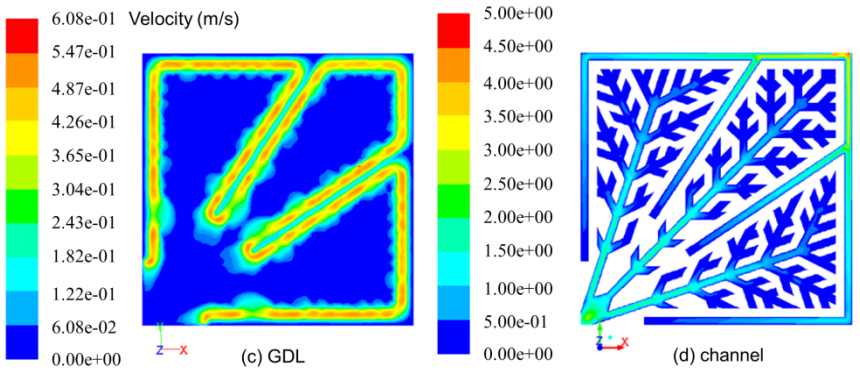

Velocity distribution

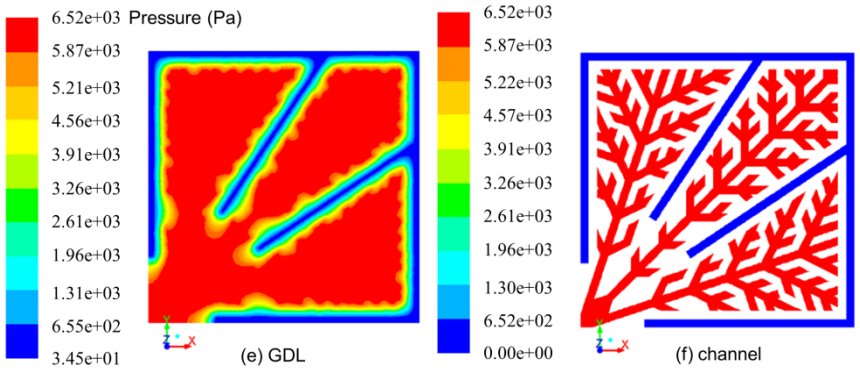

Pressure distribution

Fig. 8 Numerical results of the interdigitated bio-inspired design with constant channel width.

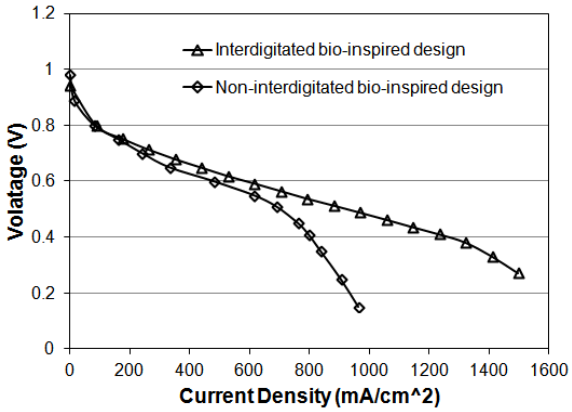

Fig. 9 Comparison of the performance of PEM fuel cell for the interdigitated and non-interdigitated bio-inspired designs.

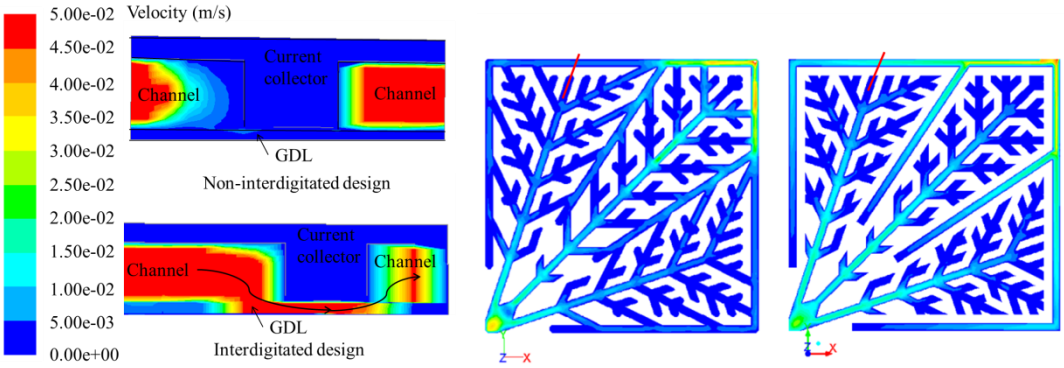

Fig. 10 Detailed under-rib velocity distributions for the non-interdigitated and interdigitated bio-inspired designs.

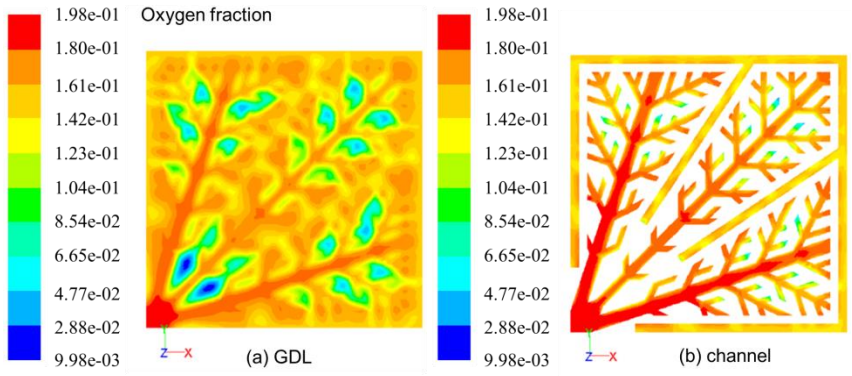

Oxygen fraction distribution

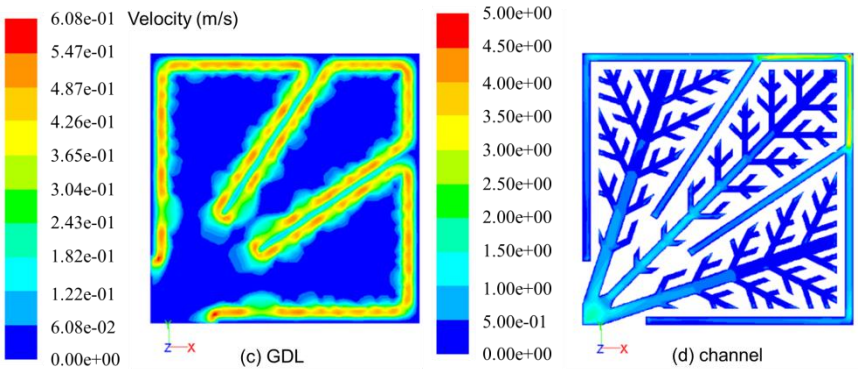

Velocity distribution

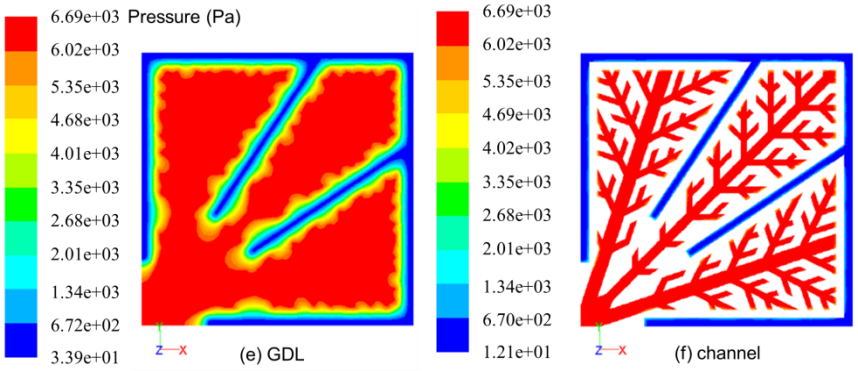

Pressure distribution

Fig. 11 Numerical results of the interdigitated bio-inspired design following Murray's law.

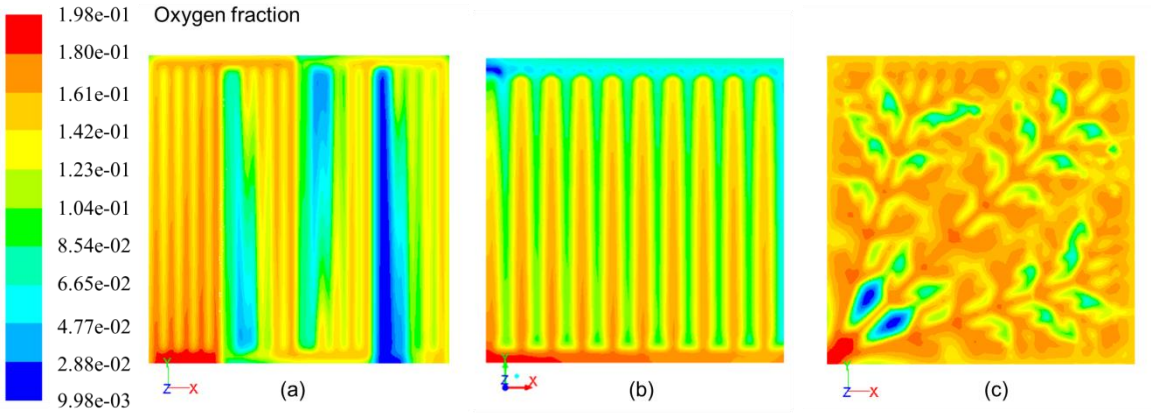

Fig. 12 Comparison of oxygen distribution in the GDL for different flow field designs: (a) interdigitated design width, (b) parallel-in-series design, and (c) bio-inspired interdigitated design with constant channel width.

Table 1 Channel widths of the bio-inspired leaf flow field design determined by Murray's law.

Branches	Generation	Hydraulic diameter (mm)	Channel width (mm)
Right & left branches	1st	1.88	2.51
	2nd	1.35	1.23
	3rd	1.20	1.00
Middle branches	1st	1.63	1.78
	2nd	1.29	1.14
	3rd	1.20	1.00

Table 2 Parameters used in the simulation model.

Reference exchange current density at anode (A/m^2)	4.48×10^{5}
Reference exchange current density at cathode (A/m^2)	4.48
Charge transfer coefficient at anode	1.0
Charge transfer coefficient at cathode	1.0
Concentration exponent at anode	0.5
Concentration exponent at cathode	1.0
Open circuit voltage (V)	0.98
H_2 diffusivity (m^2/s)	8×10^{-5}
O_2 diffusivity (m^2/s)	2×10^{-5}
H_2O diffusivity (m^2/s)	5×10^{-5}
Membrane equivalent weight (kg/kmol)	1100
Catalyst layer surface-to-volume ratio (1/m)	1.25×10^{7}
GDL electric conductivity ($1/\Omega$ m)	280
GDL porosity	0.82
GDL viscous resistance at anode ($1/m^2$)	10^{12}
GDL viscous resistance at cathode ($1/m^2$)	3.86×10^{12}
GDL and catalyst layer permeability ($1/m^2$)	5.68×10^{10}
Bipolar plate electric conductivity ($1/\Omega$ m)	92600

Table 3 Operating conditions in the simulations for different flow field designs.

Operation temperature (K)	348
Operation pressure (atm)	1.0
Anode stoichiometry	2.0
Cathode stoichiometry	2.0
Relative humidity	100%

PAPER

V. Optimization of Parallel and Serpentine Configurations for Polymer Eletrolyte Membrane Fuel Cells

Nannan Guo, Ming C. Leu, Umit O. Koylu

Department of Mechanical and Aerospace Engineering,

Missouri University of Science and Technology, Rolla, MO 65409, USA

Abstract

A network-based optimization model was developed to optimize the channel dimensions of flow fields in order to achieve a uniform flow distribution and improve the performance of polymer electrolyte membrane (PEM) fuel cells. Different flow field configurations, including parallel, parallel-in-series, and serpentine, were investigated using the present optimization model. Two cases, with and without considering reactant consumption, were compared to show the effect of including reactant consumption on the flow field designs. The results demonstrated that the optimized designs significantly improved the flow velocity distribution in all the configurations investigated. The optimized designs with consideration of reactant consumption exhibited more uniform flow velocity distribution when the entire fuel cell unit was considered. Additionally, the performances of PEM fuel cells for the conventional and optimized flow field designs were studied with a three-dimensional, two-phase fuel cell simulation model, and the computational results showed that the optimized designs with considering reactant

consumption produced the highest maximum power density for each configuration investigated. These results show that the network-based model is capable of optimizing various flow field configurations with flexibility and indicate the importance of considering reactant consumption in the optimization model.

Keywords: Flow field design; Optimization model; Parallel configuration; Serpentine configuration.

1. Introduction

The flow field of a bipolar plate distributes fuel gases to reaction sites and removes reaction products (i.e., water) out of the fuel cell, significantly affecting the performance of polymer electrolyte membrane (PEM) fuel cells [1-4]. Numerous flow field configurations have been proposed and investigated in the past. These conventional designs can be classified into four categories: pin-type, parallel, serpentine, and interdigitated. Among them, parallel and serpentine designs are the most widely known and utilized ones. Parallel designs have the advantage of low pressure drop. However, since parallel flow fields have multiple flow paths, in which gases flow preferentially through the least resistant channels, uneven flow and stagnant areas tend to form at various areas of parallel channels, lowering the transport efficiency of the reactants. Serpentine designs usually give high fuel cell performance but they typically have relatively long reactant flow path, leading to substantial pressure drop. Additionally, reactant concentration significantly decreases from the inlet to the outlet of the flow

channel. This decrease leads to considerable Nernst losses and non-uniform electric current density distribution, reducing both the overall performance and lifetime of PEM fuel cells. Therefore, it is essential to investigate and optimize the flow distribution within these configurations in order to eliminate the stagnant areas and hence improve performance.

Mathematic models have been developed by researchers to optimize flow field designs in order to improve PEM fuel cell performance. Compared with numerical models [5-7] and analytical models [8-10], network-based optimization models [11,12] have the flexibility of establishing complex networks and thus can be easily applied to various flow configurations. In a network model, channel networks are described analogically as electric circuit networks. Similar to Ohm's law, pressure drop is assumed to be proportional to flow rate. The relationship among pressure drop, flow rate, and flow resistance could be built using the Hagen-Poiseuille equation. Tondeur et al. [13,14] developed a network-based model to investigate the flow and pressure distribution in 2D intersecting channels (meshes) with different numbers of meshes. A uniform flow distribution in a rectangular lattice network was achieved by configuring the flow resistances on the periphery of the lattice. Peng et al. [15] and Zhang et al. [16] proposed a flow network based model to calculate the flow distribution within interdigitated and parallel channels and to optimize the channel dimensions in order to obtain an even flow distribution. Peng et al. [17] found that the inhomogeneous compression of the gas diffusion layer (GDL) would cause the GDL intruding into the channels and eventually change the flow distribution. Therefore, they proposed a multi-objective optimization

model based on the network approach to eliminate the non-uniform distribution in the flow field by taking the GDL intrusion into account.

Previously reported network-based optimization models have treated the flow rate over the entire flow field as constant and have not taken the consumption of reactant gases along the flow channels by electrochemical reactions into consideration. Reactant consumption has a significant effect on the flow field design as it dramatically changes the flow distribution in a fuel cell. As reactant gases flow through a fuel cell, the flow rate gradually decreases due to the reactant consumption, and hence the channels near the inlet have higher flow rates than those near the outlet. If the typical stoichiometry of 2.0 is used, the difference between the flow rates at inlet and outlet could be as high as 50%.

In the present study, a network-based optimization model with consideration of reactant consumption was developed. Different flow field configurations, including parallel, parallel-in-series, and serpentine designs, were optimized using the developed model. In order to demonstrate the effect of reactant consumption on the flow field design, two different optimization scenarios, i.e., uniform flow velocity distribution with and without considering reactant consumption, were investigated and compared. A three-dimensional, two-phase numerical simulation model of PEM fuel cell was applied to study the flow distributions of the conventional and optimized designs and to validate the proposed optimization model. Finally, the fuel cell performance characteristics of the optimized designs were compared with those of the conventional designs to study how the optimized designs would influence the final fuel cell performance.

2. Network-Based Optimization Model

The optimization model was constructed by establishing the flow relationship over the entire channel network and then setting the objective function and constraints, and solved by using Quasi-Newton algorithm. The detailed optimization model was described in reference [12], and is summarized in the following for the completeness of the present paper.

2.1 Flow relationships

The flow relationship was developed based on the following justifiable assumptions: a) the flow is laminar; b) the reactant gases are viscous; c) a constant resistance coefficient, which can be estimated empirically, exists at each channel junction; and d) reactants are consumed uniformly over the entire active area. Uniform consumption of reactants is desirable for flow field designs. Although the conventional designs normally could not achieve this situation, the designs after optimization would be very close to uniform consumption, which will be discussed later.

In the network approach, a flow field configuration can be represented as a channel network, and each channel is treated as a link connecting two nodes. The channel networks of parallel, parallel-in-series, and serpentine flow patterns are given in Fig. 1. In all of the designs, $N \times M = 21 \times 10$ nodes were used. Channel (k, l) is designated as the

channel connecting two neighboring nodes designated by k and l. For the Hagen-Poiseuille flow, the relationship between pressure drop and flow rate in each channel (k, l) is

$$\Delta p_{kl} = \frac{32\mu L_{kl} q_{kl}}{A_{kl}^{c} {D_{kl}^{h}}^{2}} \tag{1}$$

where μ is the fluid viscosity, L_{kl} is the channel length, q_{kl} is the volumetric flow rate, D_{kl}^{h} is the hydraulic diameter, and A_{kl}^{c} is the channel's cross-sectional area. The volumetric flow rate is

$$q_{kl} = v_{kl} A_{kl}^{c} \tag{2}$$

where v_{kl} is the average flow velocity in the channel. Analogous to an electric circuit network, the pressure drop in Equation (1) can be expressed in terms of flow rate and flow resistance as

$$\Delta p_{kl} = r_{kl} q_{kl} \tag{3}$$

where r_{kl} is the flow resistance in the channel, which is related to the channel's geometric dimensions as

$$r_{kl} = \frac{32\mu L_{kl}}{A_{kl}^{c} {D_{kl}^{h}}^{2}} \tag{4}$$

To take the pressure losses at the conjunction of channel segments into account, a constant resistance coefficient, r_c, is introduced to the flow resistance, r_{kl}, in equation (4), i.e.

$$r_{kl} = \frac{32\mu L_{kl}}{A_{kl}^{c} {D_{kl}^{h}}^{2}} + r_c \tag{4'}$$

Mass conservation equations were established for two cases: a) without considering reactant consumption, and b) with considering uniform reactant consumption.

(a) Mass conservation without considering reactant consumption

For a given node k, the sum of all the in-flow rates (+) and the out-flow rates (-) should equal zero,

$$\sum_k q_{kl} = 0 \tag{5}$$

where $\sum_k$ indicates the summation of all the channels connected to the node k. Substituting equation (3) into (5), a linear equation system of pressure can be established for each node k:

$$\sum_k \frac{\Delta p_{kl}}{r_{kl}} = \sum_k \frac{P_l - P_k}{r_{kl}} = 0 \tag{6}$$

This equation system has $N \times M$ equations and $N \times M$ unknowns, which consist of the pressure at each node. By solving them, the pressure at every node can be determined. In the flow field configurations investigated in this study, there are three types of conjunctions, straight connection, T corner, and L corner, as shown in Fig. 1. For each type of conjunction, equation (6) can be expressed, respectively, as

Straight connection:

$$\frac{P_{i,j-1} - P_{i,j}}{r_{(i,j)(i,j-1)}} + \frac{P_{i,j+1} - P_{i,j}}{r_{(i,j)(i,j+1)}} = 0 \tag{7-1}$$

T corner:

$$\frac{P_{i-1,j} - P_{i,j}}{r_{(i,j)(i-1,j)}} + \frac{P_{i+1,j} - P_{i,j}}{r_{(i,j)(i+1,j)}} + \frac{P_{i,j+1} - P_{i,j}}{r_{(i,j)(i,j+1)}} = 0 \tag{7-2}$$

L corner:

$$\frac{P_{i,j-1} - P_{i,j}}{r_{(i,j)(i,j-1)}} + \frac{P_{i+1,j} - P_{i,j}}{r_{(i,j)(i+1,j)}} = 0 \tag{7-3}$$

where subscripts (i, j) represent the coordinates of the nodes of channel network.

(b) Mass conservation with considering uniform reactant consumption

During fuel cell operation, the local flow rates in channels keep decreasing from inlet to outlet since the reactant gases are consumed gradually by electrochemical reactions. This makes the flow characteristics substantially different from the one with constant flow rate (without reactant consumption). For improving flow field optimization and enhancing fuel cell performance, it is necessary to take the reactant consumption into consideration. Reactants are assumed to be consumed uniformly over the entire active area, i.e., at each node, $Q/(\eta(N \times M))$ is consumed, where Q is the inlet flow rate and η represents the stoichiometry. Therefore, equation (6) is modified to

$$\sum_k \frac{P_k - P_l}{r_{kl}} = \frac{Q}{\eta(N \times M)} \tag{8}$$

2.2 Objective function

Uniform flow velocity distribution could reduce the stagnant areas and overvoltage losses within a fuel cell and hence improve the performance. To achieve uniform distribution, the standard deviation of flow velocity within all channels was used as the objective function:

$$Minimize\ E = \sqrt{\frac{\sum_{(k,l)}(v_{kl} - \bar{v})^2}{2NM - N - M}} \tag{9}$$

where $\sum_{(k,l)}$ indicates the sum over all channels, and $\bar{v} = \frac{\sum_{(k,l)} v_{kl}}{2NM - N - M}$ is the mean flow velocity.

2.3 Constraints

The total channel surface area should be fixed at a certain percentage of the active area in the optimization model to give a balance between mass transport and electrical conductivity. The percentage used in this study was 50%, thus

$$S_c = \sum_{(k,l)} L_{kl} w_{kl} = 0.5A \tag{10}$$

where A is the active area of the fuel cell. In addition, considering the feasibility of bipolar plate manufacture, the channel width should be restricted to a certain range. The range used in this study was 0.5-2.5 mm, thus

$$0.5 \leq w_{kl} \leq 2.5 \tag{11}$$

2.4 Solving the optimization problem

The model was formulated into a constrained optimization problem with channel widths as design variables. A MATLAB optimization tool box based on Quasi-Newton algorithm was employed and the corresponding program was developed to solve this problem. To start the calculation, an initial set of channel width (e.g., 1.5 mm for all channels) was used. Then, the flow resistance for each channel was determined from equation (4'), and the pressure at each node was calculated by solving the linear equation system given by either equation (6) or equation (8). Subsequently, the flow velocity in each channel was obtained from equations (2) and (3). The iteration process continued until the minimum velocity deviation was achieved following equation (9). Two

optimization cases were investigated, i.e., the optimized I design, which did not consider the reactant consumption along the flow channels, and the optimized II design, which considered the reactant consumption. Three different flow field configurations, i.e., the parallel, parallel-in-series, and serpentine designs, were optimized. The parallel-in-series design consisted of a series of connected sub-groups of parallel channels and each sub-group had three channels in this study. If H denotes the number of channels in a sub-group, then the parallel and single serpentine designs could be treated as a special case of the parallel-in-series design, where $H = 21$ for the parallel design and $H = 1$ for the single serpentine design. Table 1 gives the values of the flow field parameters used in the optimization model. It should be noted that although the optimization was performed for the anode, it would also be valid for the cathode since both anode and cathode sides are essentially the same in terms of flow velocity distribution.

3. Numerical Simulation

A three-dimensional, two-phase simulation model based on the finite element method (FEM) [18-23] was used to validate the proposed optimization model, investigate the performance of PEM fuel cells using the conventional and optimized designs, and quantify how the optimized design would affect the fuel cell performance. The detailed governing equations involved in the PEM fuel cell transport phenomena can be found in reference [24]. A PEM fuel cell module from the commercial software ANSYS Fluent was employed to solve the governing equations. The model parameters, given in Table 2, were based on Iranzo's publications [24,25], which have verified that these parameters

could provide an accurate prediction of the experimental results. The operating conditions used in the simulation model are given in Table 3. The total number of volume elements in the fuel cell computation domain was around 900,000 for each design. The computational convergence was set to 10^{-7} for all equations. The velocity distributions within the flow fields and the fuel cell polarization curves were obtained and studied. Besides the PEM fuel cell simulation model, a model simulating only the flows in the channels, referred to as the channel flow simulation model, was also developed to investigate the velocity distribution in the case of optimized I designs, in which no reactant consumption was considered.

4. Results and Discussion

4.1 Parallel configuration

Figure 2 shows the iteration process of the optimization model for the parallel configuration. Both of the cases, with and without considering reactant consumption, were investigated. The standard deviation of the velocities in different channels decreased significantly from the initial guess value. In the case of without considering reactant consumption (Fig. 2(a)), the standard deviation reduced to near zero, indicating that the flow in all the channels reached the same velocity. In the case of considering reactant consumption (Fig. 2(b)), the velocity deviation reduced from 0.07 to 0.01. The CAD models of the conventional parallel design and the two optimized designs employed in this study are shown in Fig. 3. The conventional design in Fig. 3(a) had a constant

channel width of 1.25 mm and a constant land width of 1.25 mm. For the optimized design without considering consumption in Fig. 3(b), the channel width increased from left to middle and then decreased afterwards. This is because of the characteristics of the conventional z-type parallel configuration, in which the channels near the inlet and outlet tend to have higher flow velocity while the channels in the middle of the flow field tend to have lower velocity [9]. Therefore, in the optimized I design, the channels near the inlet and outlet were narrower in order to increase flow resistance and thus reduce flow velocity, while the channels in the middle were wider in order to reduce the flow resistance and increase velocity, consequently, to achieve uniform flow velocity in the whole flow field. Figure 3(c) shows the CAD model of the optimized parallel design in the case of considering reactant consumption. The channel width increased from left to right because mass flow rate reduced as the reactants were continuously consumed. Therefore, the optimized II design had narrower channels near the inlet to reduce the flow velocity and wider channels near the outlet to increase the flow velocity. Moreover, for each channel in the optimized II design, the width was not a constant but gradually decreased from bottom to top, in order to compromise the reactant consumption and achieve uniform velocity along the channel. It is worth mentioning that although these optimized designs have varied channels, they can be easily fabricated with the Selective Laser Sintering process developed in our previous studies [26,27].

Figure 4 shows the velocity distribution in the conventional and optimized I parallel channels obtained from the FEM simulations of the flows within channels. The channels in the middle of the conventional parallel flow field had significantly low velocity and

reactants hardly flowed through these channels, as shown in Fig. 4(a). Stagnant areas tended to form in these places. After optimization, the optimized I design achieved uniform velocity distribution within different channels, as demonstrated in Fig. 4(b). The average flow velocity in each channel was plotted in Fig. 5, which clearly showed that the average velocities in all the channels were almost the same while the flow distribution had a significant improvement compared to the conventional design. The standard deviation of the optimized I design dropped from 0.087 to 0.003 compared with the conventional design, which closely matched the analytical results from the optimization model in Fig. 2(a). All these results and comparisons confirm that the network-based optimization model works well.

Figure 6 shows the flow velocity distributions of the conventional, optimized I, and optimized II parallel designs within a PEM fuel cell unit obtained from the simulations. As expected, the conventional parallel design had a relatively large stagnant area in the flow field, as shown in Fig. 6(a), where the velocity was near zero. The optimized I design greatly reduced the stagnant area but the velocity at the bottom of these channels was still close to zero due to the reduction of reactants. The stagnant areas in both of the conventional and optimized I designs were located in the same places of the flow fields because those channels in the middle of the parallel configuration had lower velocity and formed stagnant areas. Figure 6(c) clearly revealed that the optimized II design significantly improved the flow distribution of the parallel configuration when the entire fuel cell unit and reactant consumption were considered. There was no stagnant area found in the flow field and the velocities in all channels were uniformly distributed. Also,

in each channel, the velocity was distributed evenly along the channel from bottom to top; while for the conventional and optimized I designs, the velocity in each channel kept decreasing from the bottom to top due to reactant consumption.

Figure 7 shows that the performance comparisons of the fuel cells for the conventional, optimized I, and optimized II parallel designs. As expected, both of optimized I and optimized II designs performed higher than the conventional parallel designs because of more even flow distributions. The maximum power density of the optimized II design was 25% higher than that of the conventional design. Compared to the optimized I design, the optimized II design further enhanced the fuel cell performance since the flow velocity distribution in its channels was more uniform when the entire fuel cell unit was considered and reactant consumption within the cell was accounted, as shown in Fig. 6. This demonstrates that consideration of reactant consumption has a significant effect on the optimized design, resulting in improved fuel cell performance.

4.2 Parallel-in-series configuration

The parallel-in-series configuration divides parallel channels into several groups and connects these groups end to end. This configuration has the advantages of lower pressure drop compared to the serpentine configuration and good flow velocity distribution compared to the parallel configuration. However, since parallel channels still exist in each sub-group, it is difficult to distribute the flow evenly among these channels. The CAD models of the conventional, optimized I, and optimized II parallel-in-series

designs are shown in Fig. 8. The parallel-in-series configuration in this study had seven sub-groups with each sub-group having three parallel channels. The same header width of 3.0 mm, channel depth of 1.5 mm, and channel-to-rib ratio of 1:1 were used for the conventional and optimized designs. A constant channel width of 1.25 mm was used in the conventional parallel-in-series design.

Figure 9 shows the flow distributions in the conventional and optimized I parallel-in-series designs from the simulation of flow in channels while the average velocity in each channel of the conventional and the optimized I designs is given in Fig. 10. Since no reactant consumption was considered in this case, the flow distributions in different sub-groups were essentially identical regardless of location, as can be seen in Figs. 9(a) and 10. In each sub-group in the conventional parallel-in-series design, the flow velocity increased from the channel near the inlet to the channel near the outlet. This was different from the flow velocity distribution in the conventional parallel configuration in which the velocity decreased first and then increased from the inlet to the outlet. This difference was caused by the difference of parallel channel numbers in the two cases (i.e., 21 channels in the parallel configuration and 3 channels in the sub-group of the parallel-in-series configuration). Similar observations were also reported by other researchers [9].

The optimized parallel-in-series design without considering reactant consumption is shown in Fig. 8(b). The dimensions of the parallel channels in the different sub-groups were the same because of the same flow characteristics, as discussed above. The widths of the channels from left to right in each sub-group were 1.38 mm, 1.25 mm and 1.12

mm, respectively. The smaller width of the channel near the outlet increased its flow resistance and thus reduced the flow velocity. Likewise, the larger width of the channel near the inlet increased the velocity. Consequently, an even velocity distribution was achieved, as can be seen in Figs. 9(b) and 10.

Figure 8(c) shows the optimized parallel-in-series design with consideration of reactant consumption (the optimized II design). Compared with the optimized I design in Fig. 8(b), in addition to the variation of channel width in each sub-group, the channel widths of the optimized II design decreased from the left subgroup to the right subgroup due to the reduction of mass flow rate. As a result, the flow velocity distribution in the optimized II design in the fuel cell unit was much more uniform than the flow velocity distribution in the optimized I and conventional designs, as shown in Fig. 11. The velocities in all the channels in the optimized II design were around 0.08 m/s and the standard deviation was only 0.006. Although the optimized I design exhibited better flow velocity distribution when only channel flow was considered, it showed uneven flow velocity distribution when the entire fuel cell unit was investigated. As shown in Fig. 11(b), the flow velocity kept decreasing from the inlet to the outlet due to the reactant consumption along the flow channels.

A comparison of the fuel cell performance among the conventional and the two optimized parallel-in-series designs is shown in Fig. 12. As expected, because of the uniform distribution of flow velocity, both the optimized I and II designs had higher performance over the conventional design, with the maximum power density of the

optimized II design 13% higher than that of the conventional design. The optimized II parallel-in-series design further enhanced the fuel cell performance compared to the optimized I design, indicating the importance of considering reactant consumption in the optimization model.

4.3 Serpentine configuration

For the serpentine configuration, the flow velocity stays the same in all channels if the reactants are not consumed. However, in a fuel cell unit, the flow rates of reactants decrease along the flow channels. The areas near the inlet have higher reactant concentration but the areas near the outlet have lower reactant concentration. This causes uneven reaction rates on the catalyst layer and can significantly decrease the fuel cell performance as well as the lifetimes of catalyst and polymer membrane. Figure 13 shows the CAD models of the conventional serpentine design and optimized serpentine design with considering reactant consumption (the optimized II design). The conventional serpentine design had constant channel width of 1.25 mm and land width of 1.25 mm. The channel width of the optimized II design in Fig. 13(b) decreased gradually from inlet to outlet to overcome the reduction of reactant concentration and flow rate along channels. After optimization, the standard deviation of flow velocity distribution from the optimization model reduced to 2.7×10^{-5} from 1.367 in the conventional serpentine design.

Figure 14 shows the velocity distributions within the conventional and optimized II serpentine designs obtained from the fuel cell simulation model. Figure 14(a) clearly

indicated that the velocity in the conventional design decreased gradually from inlet to outlet due to the reactant consumption. In comparison, the optimized II design had nearly uniform flow distribution and the average velocity was around 0.25 m/s. This demonstrates that the network-based optimization model also works well for the serpentine configuration. The final performance curves of the conventional and optimized II serpentine designs are given in Fig. 15. The optimized II design had significantly higher voltage at higher currents compared to the conventional design because of the more uniform flow velocity distribution and therefore lower concentration losses.

5. Summary and Conclusions

A network-based optimization model with and without considering reactant consumption in the flow field was developed to optimize the flow velocity distribution within polymer eletrolyte membrane (PEM) fuel cells. Three different flow field configurations, i.e., parallel, parallel-in-series, and serpentine, were optimized using the optimization model. The performance of fuel cell was compared among the conventional, optimized I (without considering reactant consumption), and optimized II (with considering reactant consumption) designs using a three-dimensional, two-phase PEM fuel cell simulation model. The flow velocity distribution results proved the validity of the optimization model and showed that the flow distributions in the optimized designs were more uniform than those in the conventional designs. Moreover, after taking reactant consumption into account in the optimization model, the optimized II design improved the flow velocity distribution in all of the configurations investigated relative to the

optimized I design, demonstrating the importance of considering reactant consumption in the optimization model. Consequently, the PEM fuel cells based the optimized II designs had the highest power regardless of the flow field configurations considered. For the parallel configuration, the performance of the optimized II design was 25% higher than that of the conventional design. For the parallel-in-series configuration, the maximum power density of the optimized II design was 13% higher than that of the conventional design. For the single serpentine design, the optimized II design improved the fuel cell performance by 10% over the conventional design. In conclusion, this paper has shown how use the network-based optimization model to optimize the flow velocity distributions for different flow filed configurations and has demonstrated the capability and flexibility of this optimization model.

Acknowledgements

This paper is based upon work supported by the National Science Foundation under Grant #CMMI-1131659. Any opinions, findings, and conclusions or recommendations expressed in this paper are those of the authors and do not necessarily reflect the views of the National Science Foundation.

References

[1] Li X, Sabir I. Review of bipolar plates in PEM fuel cells: flow-field designs. Int J Hydrogen Energy 2005;30:359-71.

[2] Hamilton PJ, Pollet BG. Polymer electrolyte membrane fuel cell (PEMFC) flow field plate design, materials and characterisation. Fuel Cells 2010;10:489-509.

[3] Guo N, Leu MC. Experimental study of polymer electrolyte membrane fuel cells using a graphite composite bipolar plate fabricated by selective laser sintering. Int SFF Symp, Austin Aug 2012;212-25.

[4] Misran E, Daud WRW, Majlan EH. Review on serpentine flow field design for PEM fuel cell system. Key Eng Mater 2010;447-448:559-63.

[5] Wang XD, Huang YX, Cheng CH, Jang JY, Lee DJ, Yan WM, Su A. An inverse geometry design problem for optimization of single serpentine flow field of PEM fuel cell. Int J Hydrogen Energy 2010;35:4247-57.

[6] Jang JY, Cheng CH, Huang YX. Optimal design of baffles locations with interdigitated flow channels of a centimeter-scale proton exchange membrane fuel cell. Int J Heat Mass Transfer 2010;53:732-43.

[7] Xing XQ, Lum KW, Poh HJ, Wu YL. Geometry optimization for proton-exchange membrane fuel cells with sequential quadratic programming method. J Power Sources 2009;186:10-21.

[8] Maharudrayya S, Jayanti S, Deshpande AP. Pressure drop and flow distribution in multiple parallel-channel configurations used in proton-exchange membrane fuel cell stacks. J Power Sources 2006;157:358-67.

[9] Maharudrayya S, Jayanti S, Deshpande AP. Flow distribution and pressure drop in parallel-channel configurations of planar fuel cells. J Power Sources 2005;144:94-106.

[10] Wang J. Pressure drop and flow distribution in parallel-channel configurations of fuel cells: Z-type arrangement. Int J Hydrogen Energy 2010;35:5498-509.

[11] Kee RJ, Korada P, Walters K, Pavol M. A generalized model of the flow distribution in channel networks of planar fuel cells. J Power Sources 2002;109:148-59.

[12] Guo N, Leu MC, Koylu UO. Network based optimization model for pin-type flow field of polymer electrolyte membrane fuel cell. Int J Hydrogen Energy 2013;38:6750-61.

[13] Tondeur D, Fan Y, Luo L. Flow distribution and pressure drop in 2D meshed channel circuits. Chem Eng Sci 2011;66:15-26.

[14] Tondeur D, Fan Y, Commenge JM, Luo L, Uniform flows in rectangular lattice networks. Chem Eng Sci 2011;66:5301-12.

[15] Peng L, Lai X, Yi P, Mai J, Ni J. Design, optimization, and fabrication of slotted interdigitated thin metallic bipolar plates for PEM fuel cells. J Fuel Cell Sci Tech 2011;8:0110021-8.

[16] Zhang W, Hu P, Lai X, Peng L. Analysis and optimization of flow distribution in parallel-channel configurations for proton exchange membrane fuel cells. J Power Sources 2009;194:931-40.

[17] Peng L, Mai J, Hu P, Lai X, Lin Z. Optimum design of the slotted-interdigitated channels flow field for proton exchange membrane fuel cells with consideration of the gas diffusion layer intrusion. Renew Energ 2011;36:1413-20.

[18] Ferng YM, Su A. A three-dimensional full – cell CFD model used to investigate the effects of different flow channel designs on PEMFC performance. Int J Hydrogen Energy 2007;32:4466-76.

[19] Le AD, Zhou B. A general model of proton exchange membrane fuel cell. J Power Sources 2008;182:197-222.

[20] Hontanon E, Escudero MJ, Bautista C, Garcia-Ybarra PL, Daza L. Optimisation of flow-field in polymer electrolyte membrane fuel cells using computational fluid dynamics techniques. J Power Sources 2000;86:363-8.

[21] Barreras F, Lozano A, Valino L, Marin C, Pascau A. Flow distribution in a bipolar plate of a proton exchange membrane fuel cell: experiments and numerical simulation studies. J Power Sources 2005;144:54-66.

[22] Cheddie D, Munroe N. Review and comparison of approaches to proton exchange membrane fuel cell modeling. J Power Sources 2005;147:72-84.

[23] Manso AP, Marzo FF, Garmendia Mujika M, Barranco J, Lorenzo A. Numerical analysis of the influence of the channel cross-section aspect ratio on the performance of a PEM fuel cell with serpentine flow field design. Int J Hydrogen Energy 2011;36:6795-808.

[24] Iranzo A, Munoz M, Rosa F, Pino J. Numerical model for the performance prediction of a PEM fuel cell. Model results and experimental validation. Int J Hydrogen Energy 2010;35:11533-50.

[25] Iranzo A, Munoz M, Pino J, Rosa F. Update on numerical model for the performance prediction of a PEM fuel cell. Int J Hydrogen Energy 2011;36:9123-7.

[26] Bourell DL, Leu MC, Chakravarthy K, Guo N, Alayavalli K. Graphite-based indirect laser sintered fuel cell bipolar plates containing carbon fiber additions. CIRP Ann-Manuf Techn 2011;60:275-8.

[27] Guo N, Leu MC. Effect of different graphite materials on the electrical conductivity and flexural strength of bipolar plates fabricated using selective laser sintering. Int J Hydrogen Energy 2012;37:3558-66.

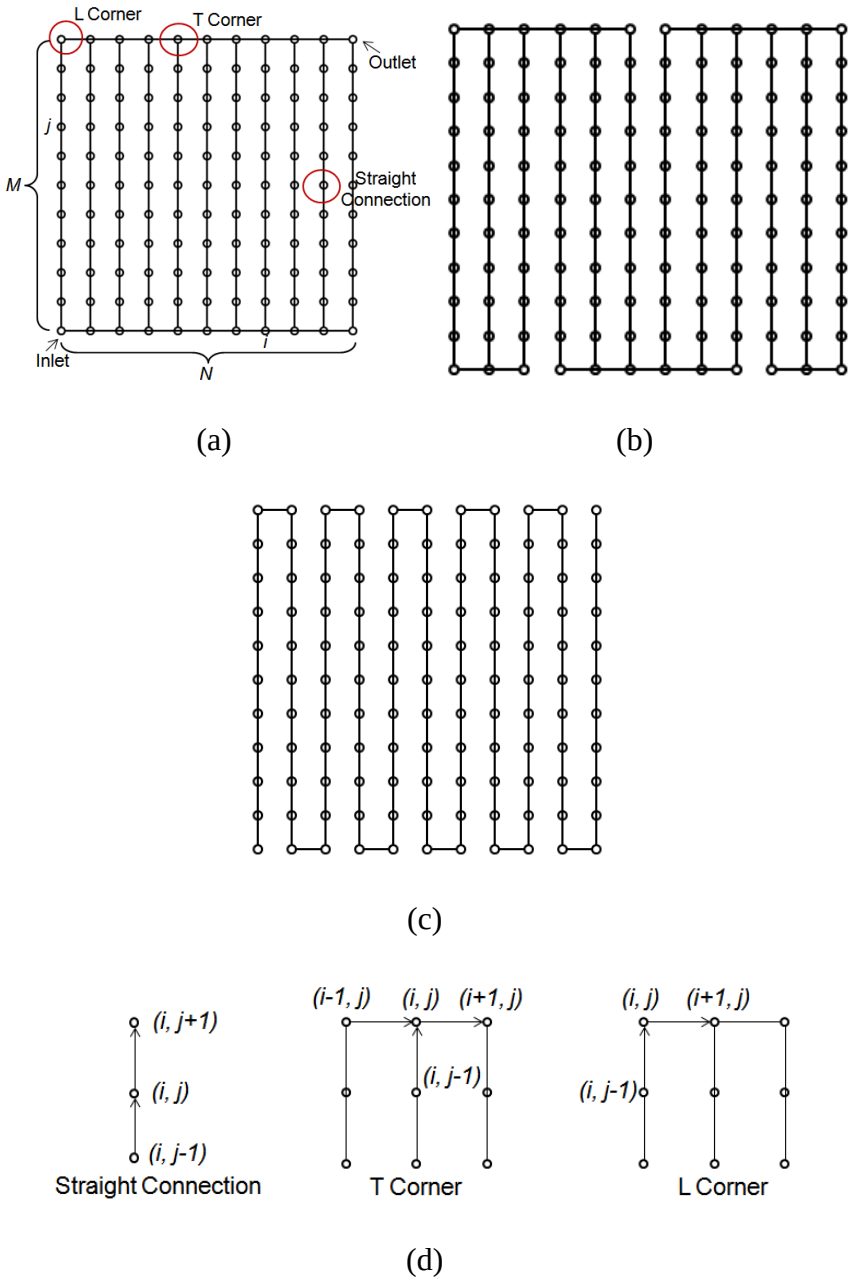

Fig. 1 Channel networks for (a) Parallel design, (b) parallel in series design and (c) serpentine design; and (d) different types of conjunctions within these flow field designs.

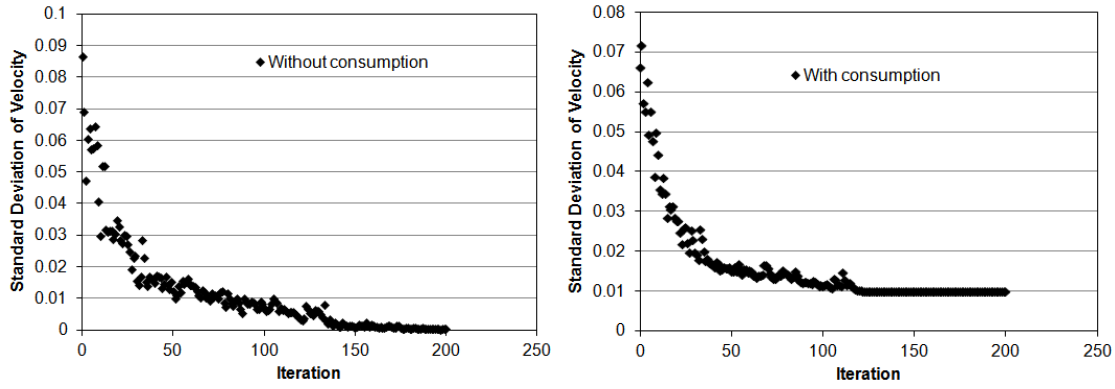

(a) (b)

Fig. 2 Iteration of the optimization model of the parallel designs for the cases of (a) without considering consumption and (b) with considering consumption.

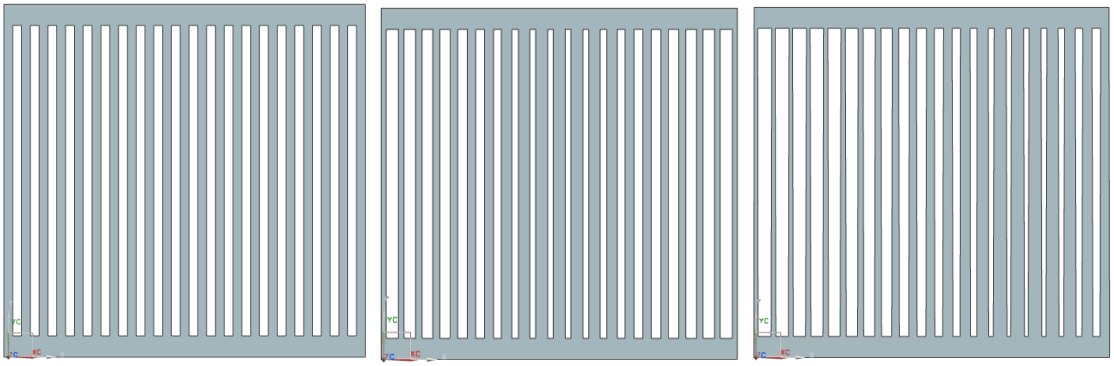

(a) (b) (c)

Fig. 3 CAD models of (a) the conventional, (b) optimized I, and (c) optimized II parallel designs. (The gray color portions are the flow channels)

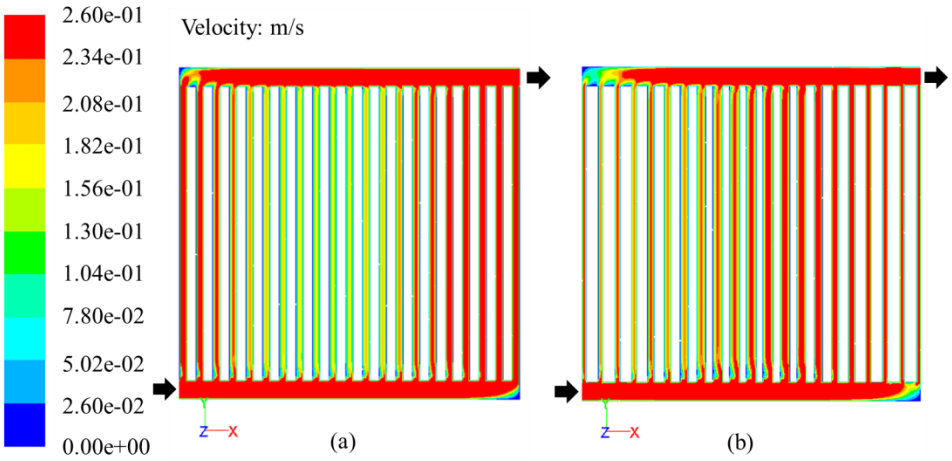

Fig. 4 Flow velocity distribution obtained from simulation of flow channels for (a) conventional parallel design and (b) optimized I parallel design.

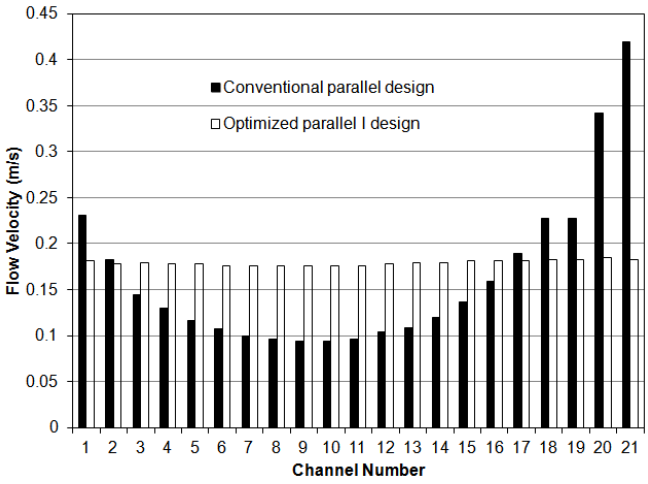

Fig. 5 Comparison of flow velocity in the channels of conventional parallel and optimized parallel I designs.

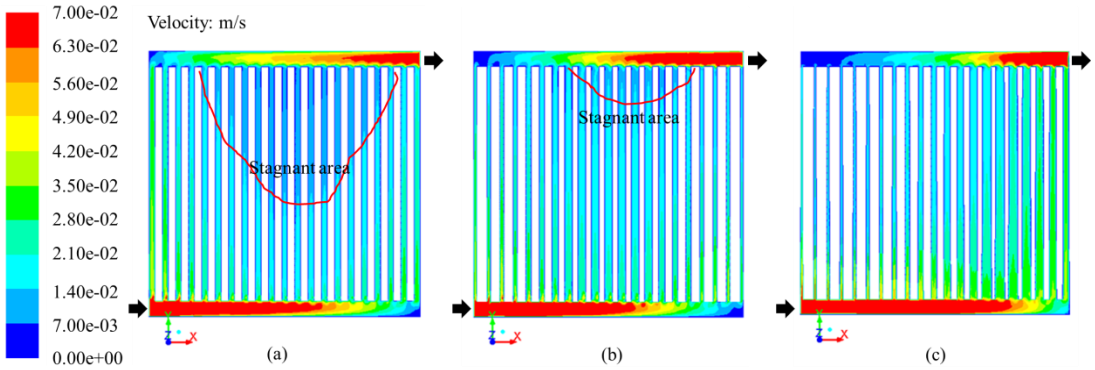

Fig. 6 Flow velocity distributions obtained from the PEM fuel cell simulation model in the case of considering reactant consumption for (a) conventional design, (b) optimized I design and (c) optimized II design.

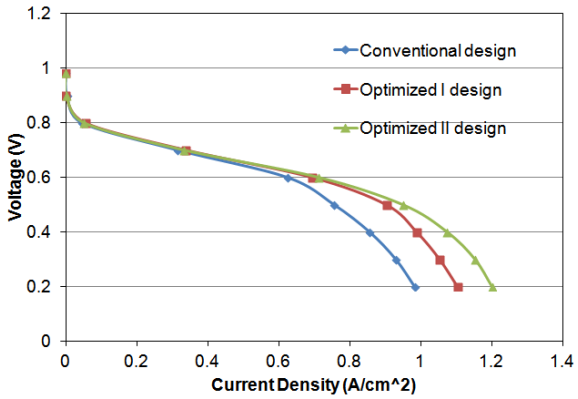

Fig. 7 Comparison of the performance of fuel cells using the conventional and optimized parallel designs.

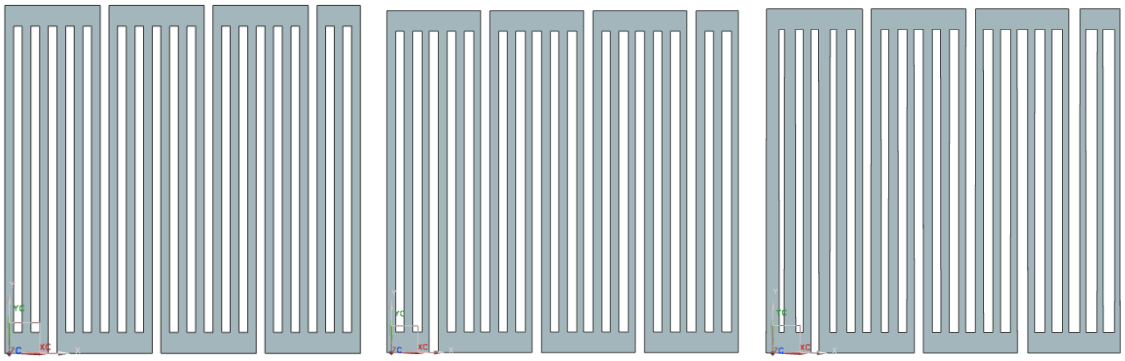

(a) (b) (c)

Fig. 8 CAD models of (a) Conventional parallel in series design, (b) optimized I design without consumption, and (c) optimized II design with consumption.

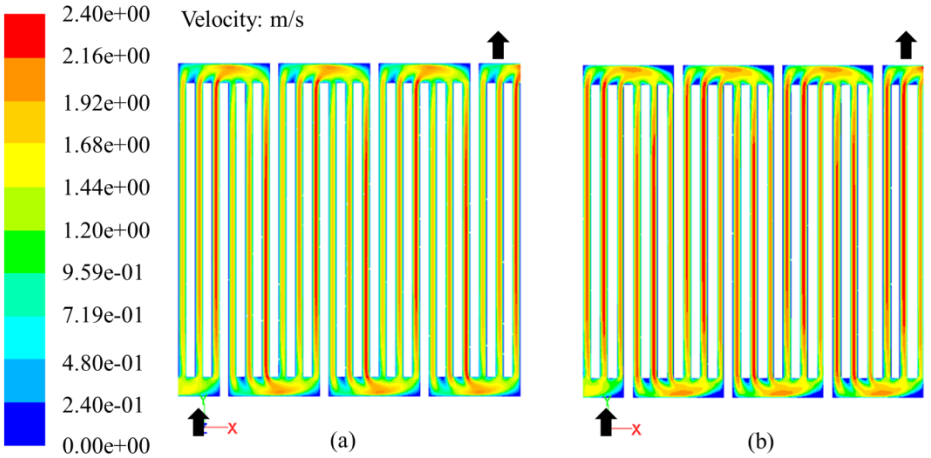

Fig. 9 Flow velocity distribution in the case of without considering consumption for (a) the conventional parallel in series design and (b) the optimized I design.

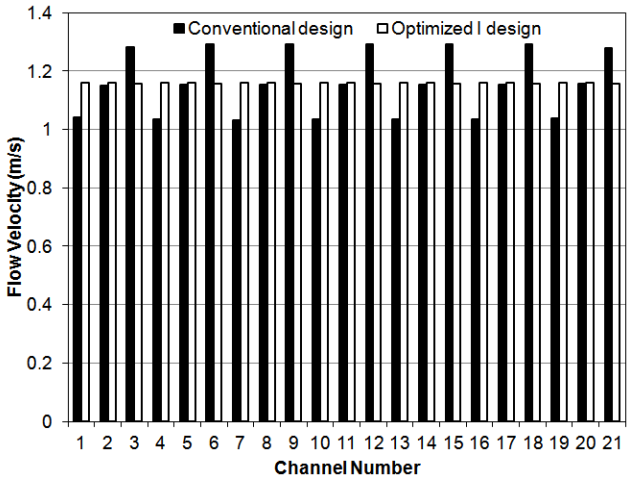

Fig. 10 Comparison of the average flow velocity in the channels of conventional and optimized I parallel in series designs.

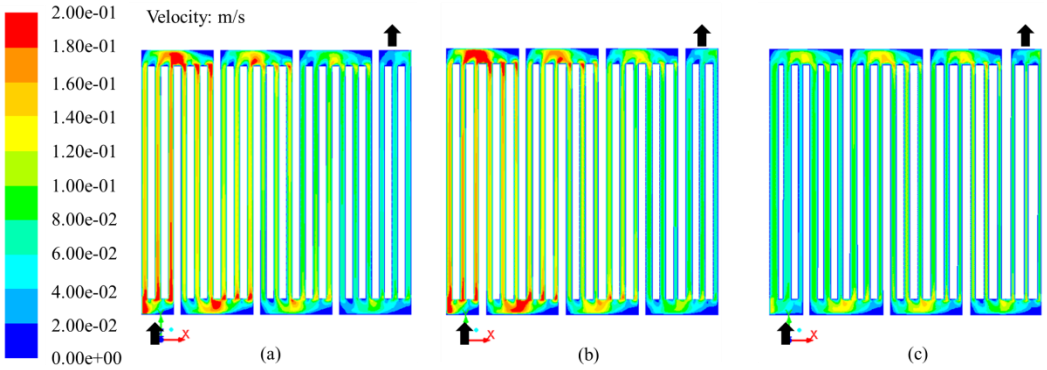

Fig. 11 Flow velocity distribution obtained from the PEM fuel cell simulation model for the parallel in series configuration (a) conventional design, (b) optimized I design and (c) optimized II design.

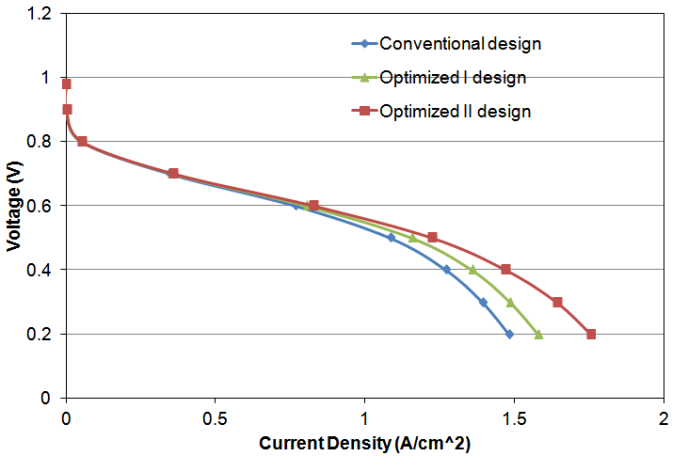

Fig. 12 Comparison of the performance of fuel cells using the conventional and optimized parallel in series designs.

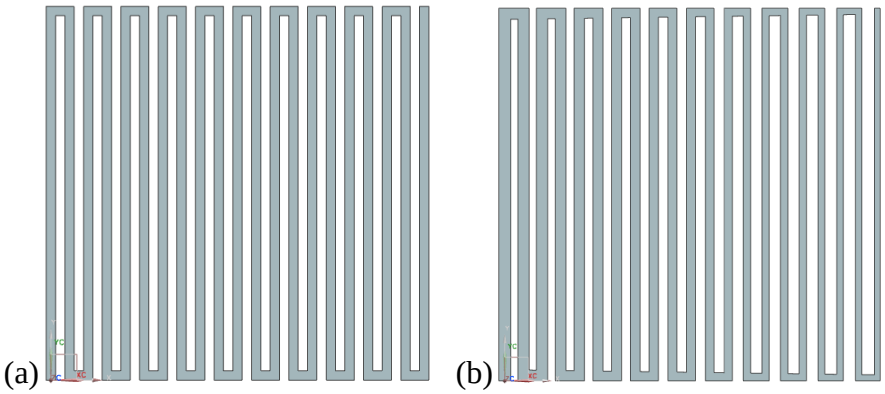

Fig. 13 CAD models of (a) the conventional serpentine design with constant channel width of 1.25 mm and (b) the optimized II serpentine design.

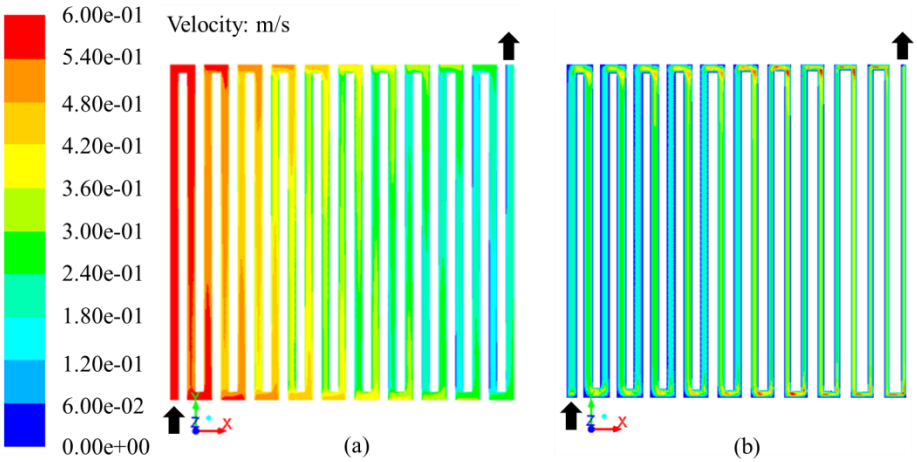

Fig. 14 Velocity distribution of (a) conventional serpentine design and (b) optimized II serpentine design.

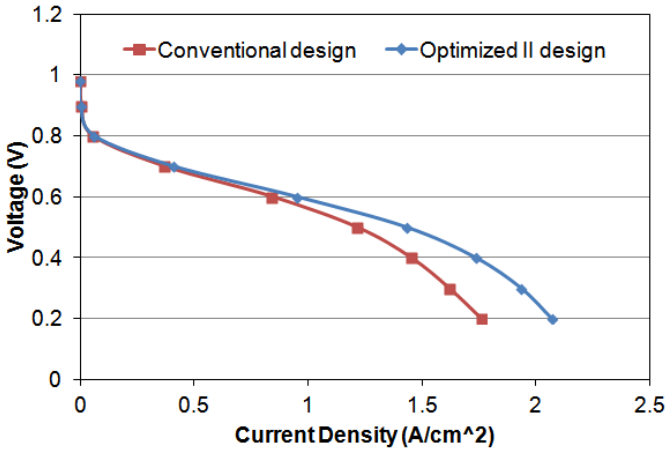

Fig. 15 Performance of the conventional serpentine design and the optimized II serpentine design.

Table 1 Parameters of the optimization model.

Active area (mm^2)	Ratio of surface area to land area	Number of parallel channels	Channel depth (mm)	Inlet flow rate (cm^3/s)	Stoichiometry
50×50	1:1	21	1.0	4.3	2.0

Table 2 Parameters in the simulation model.

Reference exchange current density at anode, referred to m^2 Pt (A/m^2 Pt)	4.48×10^5
Reference exchange current density at cathode, referred to m^2 Pt (A/m^2 Pt)	4.48
Charge transfer coefficient at anode	1.0
Charge transfer coefficient at cathode	1.0
Concentration exponent at anode	0.5
Concentration exponent at cathode	1.0
Pore blockage saturation exponent	2.0
Open circuit voltage (V)	0.98
H_2 diffusivity (m^2/s)	8.0×10^{-5}
O_2 diffusivity (m^2/s)	2.0×10^{-5}
H_2O diffusivity (m^2/s)	5.0×10^{-5}
Membrane equivalent weight (kg/kmol)	1100
Catalyst layer surface-to-volume ratio (1/m)	1.25×10^7
GDL electric conductivity ($1/\Omega$ m)	280
GDL porosity	0.82
GDL wall contact angle (deg)	110
GDL viscous resistance at anode ($1/m^2$)	10^{12}
GDL viscous resistance at cathode ($1/m^2$)	3.86×10^{12}
Bipolar plate electric conductivity ($1/\Omega$ m)	92600

Table 3 Operation parameters in the FEM simulation for different flow field designs.

Operation temperature (K)	353
Operation pressure (atm)	1.0
Anode stoichiometry	2.0
Cathode stoichiometry	2.0
Relative humidity at anode (%)	100
Relative humidity at cathode (%)	100

SECTION

2. CONCLUSIONS

Selective Laser Sintering provides a way to fabricate graphite composite bipolar plates for use in polymer eletrolyte membrane (PEM) fuel cells. This significantly reduces time and cost at the research and development stage of bipolar plates, as compared with the conventional fabrication methods such as compression molding and injection molding. Different graphite materials, including natural graphite, synthetic graphite, carbon black, and carbon fiber, were investigated using the selective laser sintering process to fabricate bipolar plates. With a proper combination of these materials, bipolar plates with electrical conductivity ranging 120-380 S/cm and flexural strength ranging 30-50 MPa have been obtained, which satisfy the requirements set by the Department of Energy and also are comparable with those developed by compression molding and injection molding.

Bio-inspired flow field designs with hierarchical structures similar to leaf veins were developed and fabricated using the selective laser sintering process. Both numerical and experimental studies were carried out to investigate the bio-inspired flow field designs. The Murray's law was used to determine the channel dimensions of different generations in order to further take advantage of the optimum transport structures in biological systems. The experimental results showed that the peak power density of the fuel cell using the bio-inspired designs was 20-25% higher than that of the conventional parallel in series and interdigitated designs. This demonstrates the significant advantages of the bio-inspired leaf design developed here.

A network-based optimization model considering the reactant consumption throughout the flow field was also developed in order to optimize the flow velocity distribution within PEM fuel cells. Four different flow field configurations, pin-type, parallel, parallel-in-series, and serpentine, were optimized using the presented optimization model. The performance characteristics of the optimized designs and the conventional designs were compared using PEM fuel cell simulation model. The flow velocity distribution results verified the optimization model and showed that the flow distributions in the optimized designs were more uniform than those in the conventional designs. The results implied that the network-based model was capable of optimizing various flow field configurations with flexibility. Moreover, after taking reactant consumption into account in the optimization model, the optimized II design improved the flow distribution in all the configurations investigated relative to the optimized I design, which did not consider reactant consumption, demonstrating the importance of considering reactant consumption in the optimization model. As a result, the PEM fuel cells using the optimized II designs had the highest power regardless of the flow field configurations considered. For the pin-type and parallel configurations, the performance of the optimized II design was 25% higher than the conventional design. For the parallel-in-series configuration, the maximum power density of the optimized II design was 13% higher than the conventional design. For the single serpentine design, the optimized II design improved the fuel cell power density by 10% than the conventional design. The optimized designs presented here are expected to improve the efficiency of PEM fuel cells, especially with the advancement in manufacturing processes such as selective laser sintering.

BIBLIOGRAPHY

[1] The Connecticut Center for Advanced Technology, Inc. Fuel cell economic development plan hydrogen roadmap. January 1, 2008.

[2] DOE Hydrogen Program Record. Fuel cell system cost – 2009. October 7, 2009.

[3] K. Promislow, B. Wetton, "PEM fuel cells: A mathematical overview," SIAM Journal of Applied Math, 2009, 70(2): 369-409.

[4] H. Tsuchiya, O. Kobayashi, "Mass production cost of PEM fuel cell by learning curve," International Journal of Hydrogen Energy, 2004, 29: 985-990.

[5] D. S. Watkins, K. W. Dircks, D. G. Epp, "Fuel cell fluid flow field plate," US Patent No. 5,108,849, 1992.

[6] D. S. Watkins, K. W. Dircks, D. G. Epp, "Novel fuel cell fluid flow field plate," US Patent No. 4,988,583, 1991.

[7] H. Li, Y. Tang, Z. Wang, Z. Shi, S. Wu, D. Song, J. Zhang, K. Fatih, J. Zhang, H. Wang, Z. Liu, R. Abouatallah, A. Mazza, "A review of water flooding issues in the proton exchange membrane fuel cell," Journal of Power Sources, 2008, 178: 103-117.

[8] J. Soler, J. Hontanon, L. Daza, "Electrode permeability and flow-field configuration: influence on the performance of a PEMFC," Journal of Power Sources, 2003, 118: 172-178.

[9] http://www.gizmag.com/artificial-leaf-blueprint/14630/picture/112719. June 2012.

[10] http://www.cancerquest.org/lung-cancer-anatomy. June 2012.

[11] A. Muller, P. Kauranen, A. Ganski, B. Hell, "Injection moulding of graphite composite bipolar plates," Journal of Power Sources, 2006(154): 467-471.

[12] S. R. Dhakate, R. B. Mathur, B. K. Kakati, T. L. Dhami, "Properties of graphite-composite bipolar plate prepared by compression molding technique for PEM fuel cell," International Journal of Hydrogen Energy, 2007, 32: 4537-4543.

[13] R. B. Mathur, S. R. Dhakate, D. K. Gupta, T. L. Dhami, R. K. Aggarwal, "Effect of different carbon fillers on the properties of graphite composite bipolar plate," Journal of Materials Processing Technology, 2008, 203: 184-192.

[14] R. Blunk, M. H. Elhamid, D. Lisi, Y. Mikhail, "Polymeric composite bipolar plates for vehicle application," Journal of Power Sources, 2006, 156: 151-157.

[15] L. Du, S. C. Jana, "Highly conductivity epoxy/graphite composites for bipolar plates in proton exchange membrane fuel cells," Journal of Power Sources, 2007, 172: 734-741.

[16] J. H. Lee, Y. K. Jang, C. E. Hong, N. H. Kim, P. Li, H. K. Lee, "Effect of carbon fillers on properties of polymer composite bipolar plates of fuel cells," Journal of Power Sources, 2009, 193: 523-529.

[17] M. C. Hsiao, S. H. Liao, M. Y. Yen, A. Su, I. T. Wu, M. H. Hsiao, S. J. Lee, "Effect of graphite sizes and carbon nanotubes content on flowability of bulk-molding compound and formability of the composite bipolar plate for fuel cell," Journal of Power Sources, 2010, 195: 5645-5650.

[18] C. Y. Yen, S. H. Liao, Y. F. Lin, C. H. Huang, Y. Y. Lin, C. M. Ma, "Preparation and properties of high performance nanocomposite bipolar plate for fuel cell," Journal of Power Sources, 2006, 162: 309-315.

[19] N. Guo, M. C. Leu, "Effect of different graphite materials on electrical conductivity and flexural strength of bipolar plates fabricated by selective laser sintering," International SFF Symposium, Austin, 2010.

[20] S. Chen, D. L. Bourell, K. L. Wood, "Fabrication of PEM fuel cell bipolar plates by indirect SLS," International SFF Symposium, Austin, 2004.

[21] S. Chen, J. Murphy, J. Herlehy, D. L. Bourell, "Development of SLS fuel cell current collectors," Rapid Prototyping Journal, 2006: 275-282.

[22] S. Chen, D. L. Bourell, K. L. Wood, "Improvement of electrical conductivity of SLS PEM fuel cell bipolar plates," International SFF Symposium, Austin, 2005.

VITA

Nannan Guo was born on February 21, 1985 in Changzhi, Shanxi, China. He received his B.S. in Mechanical Engineering from Xi'an Jiaotong University, Xi'an, Chian, in June 2006. In June 2009, he received his M.S. in Mechanical Engineering from Xi'an Jiaotong University, Xi'an, China.

Nannan Guo won the first place award for the paper entitled "Optimization model for bio-inspired design of bipolar plate flow fields for polymer electrolyte membrane fuel cells" at the Intelligent Systems Center Graduate Research Symposium on April 13, 2012 at Missouri University of Science and Technology.

In August 2013, he received his Ph.D. under the guidance of Dr. Ming C. Leu in Mechanical Engineering from Missouri University of Science and Technology, Rolla, Missouri, USA.

During his graduate study, he authored and co-authored 7 journal papers and 5 conference papers.